Martin Landfahrer, BSc

Computational investigation of the blow-out characteristics of a multi-hole distributor used for industrial dedusting systems

MASTER'S THESIS

to achieve the university degree of

Diplom-Ingenieur

Master's degree programme: Chemical and Process Engineering

submitted to

Graz University of Technology

Supervisor

Ao. Univ.-Prof. Dipl.-Ing. Dr.techn. Helfried Steiner

Institute of Fluid Mechanics and Heat Transfer

Graz, May 2016

A work as this is never finished, one must simply declare it finished when one has within limits of time and circumstances, done what is possible

-Johann Wolfgang von Goethe

AFFIDAVIT

I declare that I have authored this thesis independently, that I have not used other than the declared sources/resources, and that I have explicitly indicated all material which has been quoted either literally or by content from the sources used. The text document uploaded to TUGRAZonline is identical to the present master‘s thesis.

Date

Signature

Abstract

The present work investigates the flow in a compressed air distributor channel (manifold) typically met in mechanical bag filter dedusting devices in industry. In the existing applications a fairly non-uniform distribution of the gas flow exiting from the manifold into the individual bags is often observed. Consequently, some single bags are insufficiently cleaned, while others are subject to unacceptably large mechanical cleaning impulses. The latter implies unduly high strain exerted on some filters which have therefore be replaced more frequently. Another problem which may arise is the caking of sedimented dust in the upper part of the bags. Large amounts of caked dust deposited in the upper part of the bags may in the worst case impede a stable and safe operation of the whole filtering device. Both problems may possibly be avoided when the compressible gas flow inside the distributor duct is better understood motivating the present CFD simulations.

Since the exceedingly high computational cost did not allow for a spatially three-dimensional numerical modelling of the real full-size geometry, a simplified two-dimensional model considering a reduced geometry was developed. Some three-dimensional simulations of representative test cases were still carried out to evaluate the predictive capability of the two-dimensional model. Aside from some minor discrepancies the simplified two-dimensional model was proven as a reliable approach for describing the essential features of the considered flow.

The obtained computational results reflect the problem of the non-uniformly distributed momentum of the pulse jets emanating at the individual exits of the manifold very well. The passage of the shock front reflected from the end and its collision with the density discontinuity is found as the major reason for the observed significantly higher increase in exit momentum, and hence, the exceedingly high cleaning impact on the filters, located near the end of the duct. The modification of the end of the duct by attaching of an extra expansion volume is shown to alleviate this problem to some extent. Due to the additional volume the otherwise normally reflected strong shock is diffracted into several weaker reflections. The returning diffracted reflections successively pass the individual exits, not only later in time as compared to the case with unmodified end. They also lead to a successive compression of the gas in several smaller steps, so that the otherwise almost jump-like sharp increase in exit momentum is turned into a more gradual change. The resulting less steeply increasing impact of the pulse jets injected into the filters may expectedly help to extend the material life-time of the filter bags.

Kurzfassung

Die vorliegende Arbeit untersucht die kompressible Luftströmung in einer Druckluftleitung einer Schlauchfilteranlage, wie diese häufig zur Entstaubung in der Industrie verwendet werden. Ein in diesen Anlagen typischerweise auftretendes Problem ist die mitunter sehr ungleichmäßige Verteilung des Gasstroms auf die einzelnen Filterschläuche. Dies führt dazu, dass einzelne Filter unzureichend gereinigt werden und andere wiederum mit einem zu großen Abreinigungsimpuls beaufschlagt werden. Eine unzureichende Abreinigung kann zum Anbacken von Sediment führen. Starke lokale Anbackungen im oberen Bereich der Filtersäcke können im Extremfall den Betrieb der gesamten Anlage destabilisieren. Erfahren einige Filter hingegen einen zu starken Druckluftimpuls für deren Abreinigung, werden diese mechanisch weitaus stärker belastet und müssen daher öfter ersetzt werden. Beide Probleme sollen durch ein besseres Verständnis der hochgradig instationären kompressiblen Luftströmung im Inneren des Verteilerrohres vermindert oder sogar vermieden werden. Dieser Einblick soll durch CFD Simulationen gewonnen werden.

Da der Rechenaufwand zur numerischen Betrachtung eines dreidimensionalen Modells der gesamten Verteilerrohrstrecke einer realen Anlage unakzeptabel groß wäre, werden in den Simulationen primär vereinfachte zweidimensionale Geometrien betrachtet. Für spezielle Testfälle wurden dennoch dreidimensionale Vergleichssimulationen durchgeführt, um die Vorhersagefähigkeit der reduzierten zweidimensionalen Modelle zu evaluieren. Abgesehen von einigen eher geringfügigen Abweichungen zeigte sich hierbei gute Übereinstimmung. Die räumlich zweidimensionale Modellierung erwies sich somit als rechnerisch effizienter und zuverlässiger Ansatz zur Beschreibung der wesentlichen Merkmale der kompressiblen Strömung im betrachteten Verteilerkanal.

Die von den Simulationen erhaltenen Ergebnisse spiegeln sehr gut die in der Praxis oftmals beobachtete stark unterschiedliche zeitliche Entwicklung und Intensität der aus einzelnen Ausgängen des Verteilerkanals jeweils austretenden Impulsströme wieder. Als wesentliche Ursache dieser Ungleichförmigkeit konnte die am Ende des Verteilerkanals reflektierte Stoßwelle identifiziert werden, insbesondere deren Wechselwirkung mit der Dichtediskontinuität, welche der primären Stoßwelle nachfolgt. Durch eine Modifikation des Kanalendes in Form eines direkt am Ende des Verteilerkanals angeschlossenen Expansionsvolumens konnte dieser Effekt bis zu einem gewissen Grad abgeschwächt werde. Durch die Wandgeometrie dieses Volumen wird der Stoß nicht mehr als starke Einzelwelle normal reflektiert, sondern als Sequenz mehrerer schwächerer Reflexionen. Diese schwächeren Reflexionen passieren zeitversetzt die einzelnen Auslässe und führen dort zu einem weniger abrupten Druckanstieg. Der vom reflektierten Stoß im unmodifizierten Kanal an den Ausgängen des Verteilerkanals induzierte nahezu instantan ansteigende starke Austrittsimpuls wird so zeitlich auf mehrere Impulse verteilt, welche graduell an Intensität zulegen. Dies kann die ansonsten starke mechanische Belastung der Filter verringern und somit deren Lebensdauer deutlich erhöhen.

Index

Symbol directory

Latin letters

A	Cross- sectional area	[m^2]
a_0	Velocity of sound	[m/s]
$\hat{a}/a_0$	Critical Ratio of the velocity of sound at M=1	[-]
a, θ	Parameters	[-]
B	spanwise extension of the planar duct	[m]
$C_\mu, C_{\varepsilon 1}, C_{\varepsilon 2}$	Model constants in the k-ε model	[-]
c_v, c_p	Heat capacities at constant volume and constant pressure	[J/kgK]
D	Diffusion coefficient	[m^2/s]
d_H	Hydraulic diameter	[m]
d	Diameter of the exit holes in the real application	[m]
E	Empirical constant in the u* approach	[-]
e	Specific internal energy	[J/kg]
$\hat{e}$	total energy	[J/kg]
Fr	Froude number	[-]
f_i^B	Body forces	[N/m^2]
g	Gravitational accceleration	[m/s^2]
H	The height of the square distributor duct	[m]
h	Mass specific enthalpy	[J/kg]
k	Turbulent kinetic energy	[m^2/s^2]
L_0	Reference value for the length	[m]
l_μ	Reference scale for the standard wall function	[m]
M	Mach number	[-]
$\dot{m}_{in}$	Mass flux at the inlet	[kg/sm^2]
M_G	Molecular weight	[kg/mol]
$\hat{\dot{m}}$	Critical mass flux	[kg/sm^2]
p	Pressure	[Pa]
Pr	Prandtl number	[-]
p_0	Reference Pressure	[Pa]
p^*	Dimensionless pressure	[-]
$\hat{p}/p_0$	Critical Ratio of the pressure at M=1	[-]

Q_ϕ	Mass specific source term of quantity ϕ	[kg/m³s [ϕ]]
q_j	Conductive heat flux	[W/m²]
$\dot{q}_Q$	Internal heat sources	[W/m³]
R	Universal gas constant	[J/molK]
R_S	Specific gas constant	[J/kgK]
Re	Reynolds number	[-]
s	Length of the flow filament	[m]
T	Temperature	[K]
T*	Dimensionless Temperature	[-]
$\widehat{T}/T_0$	Critical Ratio of the temperature at M=1	[-]
T_0/T	Ratio of the temperatures at two points	[-]
t	Time	[s]
t^*	Dimensionless time	[-]
U	Circumference	[m]
U_0	Flow velocity	[m/s]
u_0	Reference value for the velocity	[m/s]
u	Velocity in general	[m/s]
u_i, u_j, u_k	Velocity (i, and kindicates the Cartesian coordinates: x,y,z)	[m/s]
u_x, u_y, u_z	Velocity in the Cartesian coordinates x,y,z	[m/s]
u_i^*, u_j^*	Dimensionless velocity	[-]
u_τ	Wall friction velocity	[m/s]
u*	Dimensionless velocity as realized in Ansys Fluent	[-]
W	Velocity of a disturbance	[m/s]
w_{exit}	Width of the exit slots used in the 2D-simulations	[m]
x	Cartesian Coordiante	[m]
x_i, x_j	Coordinate direction i and j	[-]
x_i^*	Dimensionless coordinate direction i	[-]
y	Cartesian Coordiante	[m]
z	Cartesian coordinate	[m]

Greek letters

Δt	Time step	[s]
Δx	Size of a cell in the mesh	[m]
δ_{ij}	Kronecker delta	[-]
ε	Dissipation rate of the turbulent kinetic energy	[m^2/s^3]
κ	Isentropic exponent [-]	[-]
κ_t	von-Kármán constant	[-]
λ	Materials conductivity	[W/mK]
λ_0	Reference for material conductivity	[W/mK]
λ^*	Dimensionless material conductivity	[-]
μ	Dynamic viscosity	[kg/ms]
μ_t	Turbulent viscosity	[kg/ms]
μ_0	Reference dynamic viscosity	[kg/ms]
μ^*	Dimensionless dynamic viscosity	[-]
ρ	Density of the media	[kg/m^3]
ρ_0	Reference density	[Pa]
ρ^*	Dimensionless density	[-]
$\hat{\rho}/\rho_0$	Critical Ratio of the density at M=1	[-]
τ_w	Wall shear stress	[N/m^2]
τ_{ij}	Stress tensor (i, j indicate the Cartesian coordinates: x, y, z)	[N/m^2]
τ_{ij}^*	Dimensionless stress tensor	[-]
ϕ	Arbitrary conserved quantity	[ϕ]
ω	Characteristic frequency of the energy supporting vortices	[1/s]

Acronyms

CFD	Computational fluid dynamics
DNS	Direct numerical simulation
FCT	Flux corrected transport
FDM	Finite difference method
FEM	Finite elements method
FVM	Finite volume method
LES	Large eddy simulation
PM_{10}	Particles with a diameter of 10 µm, and less
RANS	Reynolds- Averaged- Navier- Stokes
RNG	Renormalisation Group
RSM	Reynolds stress model
SST	Shear stress transport
UDF	User defined function

1. Introduction

1.1.Motivation and Background

The present study was motivated to gain a better understanding of the compressible air flow in a blow pipe of a bag filter device. To this end the flow is investigated using numerical flow simulation, generally termed *Computational Fluid Dynamics (CFD)*. CFD is a useful tool to describe various kinds of flows, be it in nature, biological systems, or technical applications evolving on very different scales of magnitude, such as blood flow in small veins, or atmospheric flows in big wind systems. In industrial applications CFD is often used as a powerful tool for the layout and design of technical devices, where this approach generally represents an attractive alternative to comprehensive, time consuming and costly experimental campaigns to be carried out on expensive test facilities. A further crucial advantage of numerical simulations in comparison to measuring techniques lies in the fact that the relevant physical quantities can easily be determined at any position of the flow field (Schneider, 1999). In experiments this is often not possible or associated with great technical and financial effort. For these reasons CFD simulations are used more and more often in industry.

Since the air-pollution and its prevention or reduction become increasingly important, many companies take much effort to improve the industrial processes for air pollution control. In addition to meanwhile well-established measurement techniques, numerical simulations are becoming increasingly important for the further development and optimization of these complex processes. Based on a detailed numerical description it is possible to clearly identify flow related problems and to derive a most reliable solution, technologically as well as economically. The big effort spent on the control of the emission of dust particles is due to the fact that these small particles can have a significant impact on human health. In principle, it can be said that particles with a diameter smaller than 10 µm, also referred to as PM_{10}, are respirable and can cause adverse health consequences. The possible hazardous effect on human health can also be attributed to the fact that those particles consist of several single components, as illustrated in Figure 1. The main ingredients reach from elementary- and organic carbon, other organic materials, mineral components to heavy metals and many others. The composition of the particles depends to a large extent on the emission sources. One of the great challenges is to identify the emission sources of the dust particles. Due to the great importance in air pollution control many studies have carried out on this subject. In Austria this type of investigations revealed the industry, road traffic, room heating, agriculture and construction industry as the five largest sources. According to several studies it can be said that the three main emission sources of PM_{10}, i.e., the industry, road traffic and room heating, make up approximately 75% of the whole PM_{10}-dust emission in Austria (status as of 2002).

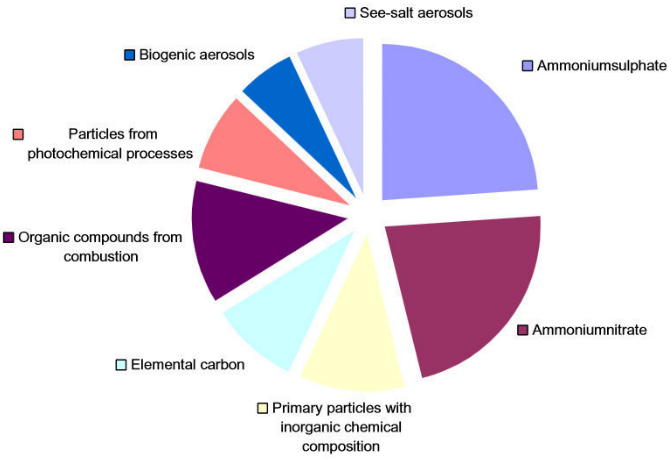

Figure 1: Contribution of different chemical components to the total mass in rural areas of north Western Europe [1]

In industry the dust emissions primarily originate from combustion processes of manufacturing industry and from process heat generation. Particles are also generated in big energy conversion systems, like power or heating plants. The emissions caused by the road traffic are more difficult to capture. Beside the direct exhaust gas emissions of cars, the abrasion of the tyres and the turbulent air flow around the vehicles, which causes a resuspension of particles, add to the total emission of the road traffic. The dust emissions of the third largest contributor, the room heating, are almost exclusively caused by solid fuel combustion, burning wood and coal. [2]

It is obvious, that the PM_{10} dust is generated differently by the different contributors. It is therefore often necessary to regulate the dust emissions for each individual contributor separately. For example, the emissions of heating plants in industry are regulated dependent of their capacity. Various different separation technologies have been established in heating plants and industry, which are explained in more detail in the following section. The appropriate choice of the most suited separation method depends on many factors, such as the size and shape of the particles as well as the composition of the crude gas and the required separation efficiency [2]. In general it can be said that particles with a size bigger than 20 μm, are technically easy to separate. Particles which are even bigger than 100 μm can be simply separated using gravity settlers. In contrast, smaller particles require more sophisticated techniques.

For a better awareness of the complexity of the problem typical particle size intervals of different types of dust are shown in Figure 2. It becomes apparent that these dusty media are typically composed of particles strongly varying in size. This characteristic feature makes it hard to find one optimum solution for all sizes. In fact, the solution to be sought will be rather found as a best-suited compromise. [3][4][5]

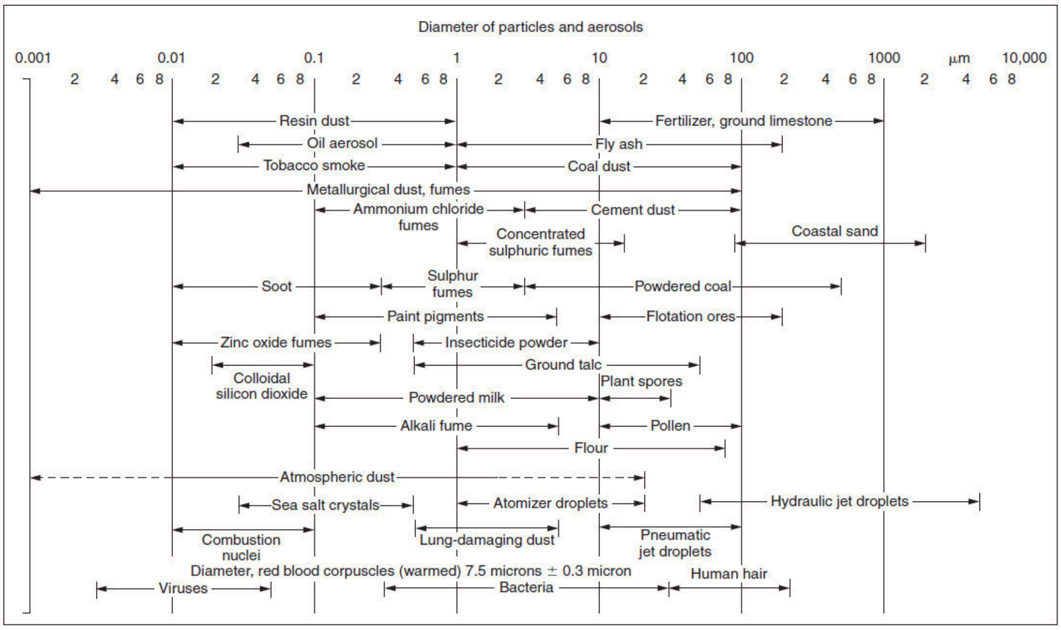

Figure 2: Different types of dust and their typical particle size variation [6]

1.2.Particle separation methods

This chapter describes a couple of well-established techniques which have been developed to remove particles from dusty gas streams in industrial applications. The main types of particle separation systems used in industry today are the mass force -, filtering-, electrostatic separators and wet scrubbers. All of these systems are based on a different separation mechanism, which makes them better suited to one process and less suited to the other. The separation systems also differ in the purity they can provide, which further depends heavily on the particle diameter. As one can imagine the purity required for the cleaned gas is different for turbines or gas engines. [7][4]

Figure 3 shows the filtration efficiency dependent of the particle diameter. This efficiency represents the percentage of particles, which are separated, for a given particle diameter. It becomes clear that some separation methods are more appropriate for separating larger particles as compared to others. As seen from Figure 3, a cyclone separates at least 50 percent of the particles with a diameter larger than 8 μm. The different methods shown in Figure 3 and their underlying operating principles are explained briefly in the following chapters.

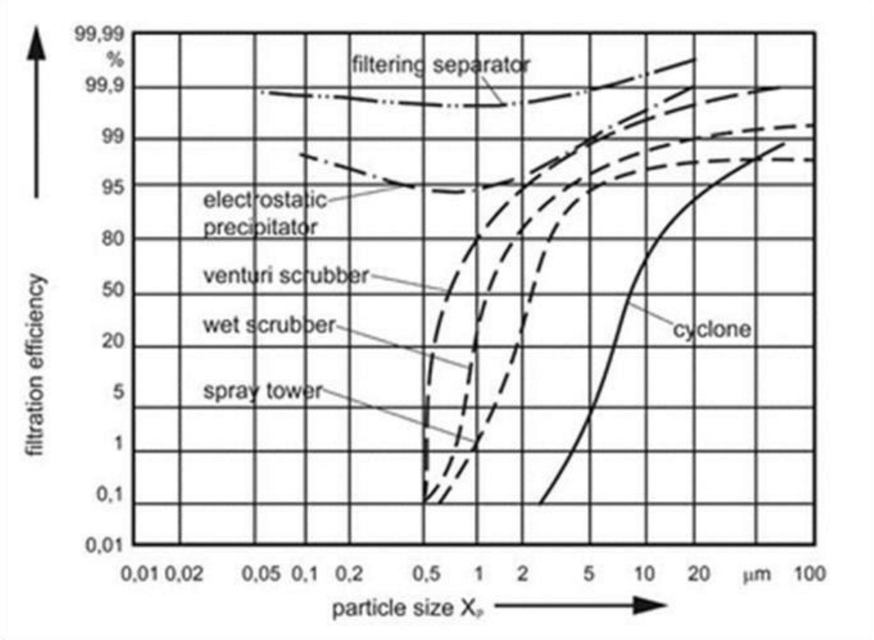

Figure 3: Filtration efficiency over particle size of different separation methods [8]

1.2.1. The main types of separators

Mass force separator

As the terminology suggests, these types of separators use the mass forces to separate the particles. The technically easiest method uses the gravity force to separate the particles. As such these separators are also called gravity separators. They consist of very simple pools, where the particles stay over sufficient time to sediment. This method can be applied only to big particles, because small particles would settle too slowly and the needed pool size would be too large. [3]

Other mass force separators apply other forces to accelerate the sedimentation process. The best known of them is the cyclone. The cyclone is also well-suited for rather big particles. The operation principle is schematically shown in Figure 4. The dust-laden gas enters the cyclone at the top and is forced into rotation. The sedimentation occurs because the particles cannot follow the vortex inside the cyclone. This is due to the fact that particles have a higher inertia than air. Driven by centrifugal forces they are conveyed to the outer walls where the solid particles are separated and collected in the silo underneath. [7][3]

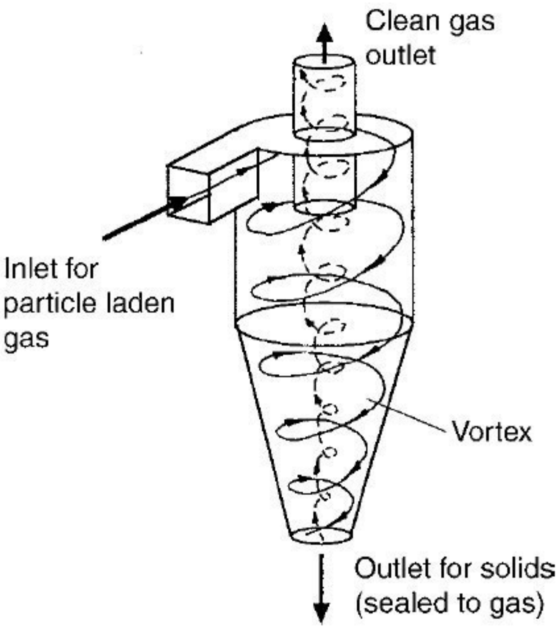

Figure 4: Gas cyclone [9]

The major advantage of cyclones is that they can be applied in a large temperature range. The dust-laden gas does therefore not have to be cooled or heated. [7]

Cyclones are present in many processes and if necessary multiple units are used, where they can be arranged as a serial or parallel multi-cyclone, as shown in Figure 5. Cyclones arranged in series are used when the solid concentration is very high, so that a sequential multi-stage separation is needed. On the other hand, cyclones are arranged in parallel, when the dusty gas input stream is too large to be handled with a single cyclone. The gas stream is then divided and fed into the individual cyclones.[10]

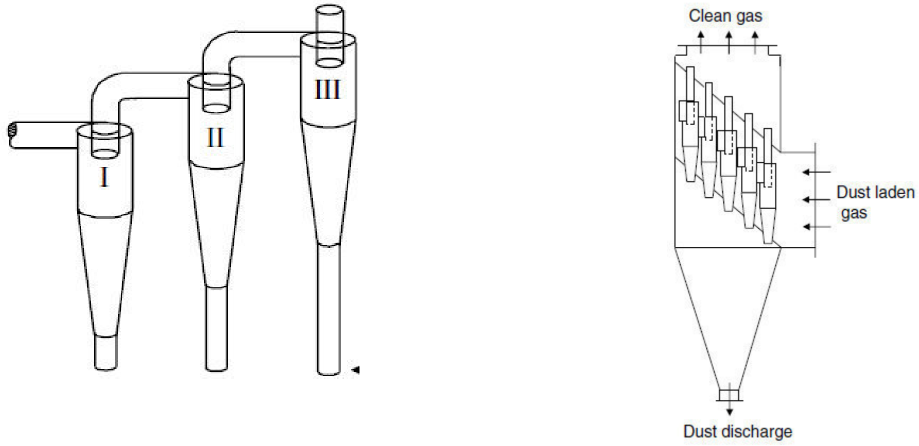

Figure 5: Types of multi-cyclones: Serial arrangement left and parallel right [10]

Electrostatic filters

The electrostatic filters are not filters in the conventional sense; they rather belong to the precipitators. They do not use any filter material, a corona point discharge is used instead to charge the particles and thus separate them. Figure 6 shows the principle of an e-filter. At the electrode, mostly a wire with spikes, a high voltage is applied. This causes the emission of negative electrons into the gas compartment between. The dust-laden gas flows past the high-voltage electrodes and the particles are negatively charged. The electrically charged particles migrate to the plate separator, where the particles are separated wet or dry. Dry cleaning means a periodical cleaning of the plate separator by knocking. Wet cleaning uses a thin film of water which flows along the plate separator. A big advantage of the e-filters is the possibility to separate particles below 1μm. They can also operate at higher temperatures like cyclones. [3][4][10]

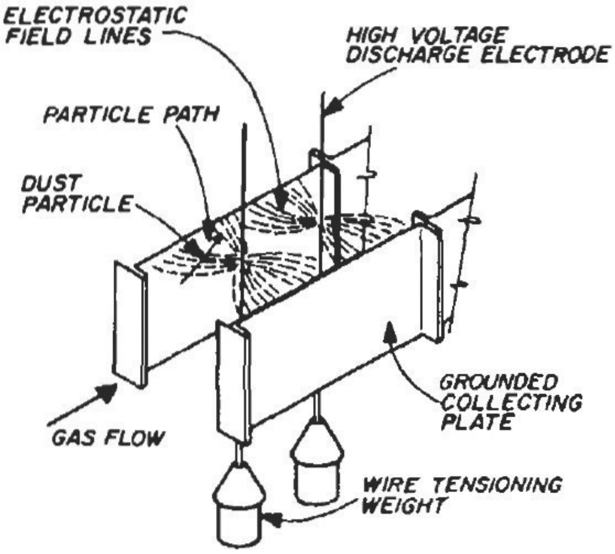

Figure 6: Basic design and functional principle [11]

Wet scrubbers

These types of separators are based on a spray of liquid or liquid films to wash out the particles. These methods are very effective for a particle size about 1 [μm]. Here the particles adhere to the strongly increased surface of the liquid, so that they are essentially trapped by the liquid, which carries them out of the system. [4]

There exist many methods to generate the required large liquid-gas interface constituted by highly dispersed fine droplets. Typically, special arrangements of conventional spray nozzles are used for this purpose. There are, however, also other designs used in industry. Figure 7 shows some of the most common designs. [4]

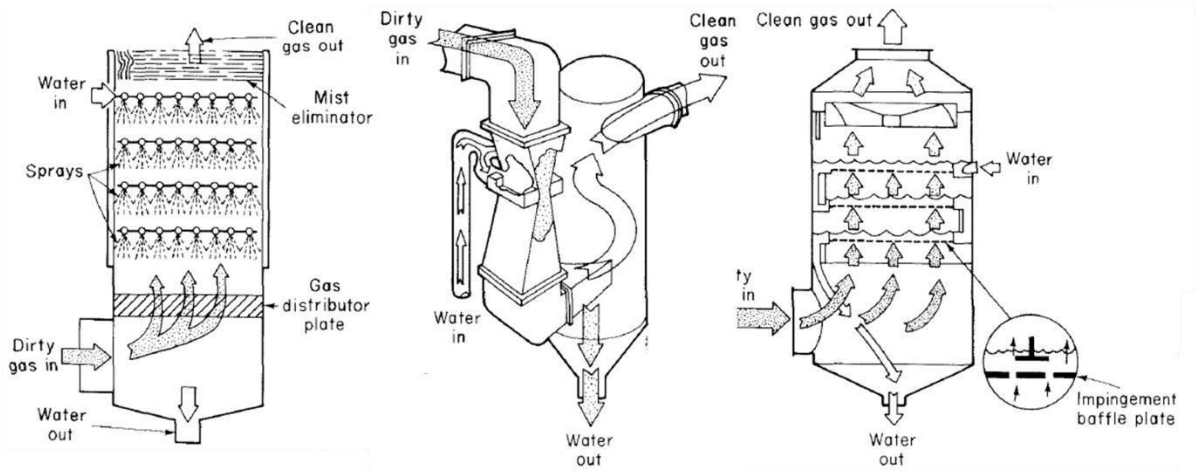

Figure 7: Most common designs of wet scrubbers: Spray tower, ventury scrubber and packed bed scrubber [4]

Filter separators

Filter separators work with porous materials which serve as a barrier for the particles. These porous materials can be felts, nonwovens, like fleeces or tissues. The main representatives of the filter separators are the bag-, pocket-, cartridge- and cassette filters.[7][9]

One can imagine this filter media as discrete, interconnected collectors constituted by fibres or grains. In general, one can distinguish between surface filtration and depth-loaded filtration. The main difference between these two mechanisms is the location, where the particles are separated. In the case of depth-loaded filters, the particles enter the filter medium and get separated inside. Whereas, in surface filters the particles are separated on the surface and only a few enter the filter medium. The major disadvantage of the depth-loaded filters is that the filters have to be replaced, if the pressure loss gets too high due to the blocking of the separated particles. In contrast, the surface filters are periodically cleaned within certain intervals, which are generally termed “regeneration”, to bring the pressure loss down. [12][13]

Filter separators can be specially designed such that almost any particle size can be separated. However, as the sizes of the pores of the filter medium are reduced, the pressure loss increases. Due to this restriction, the smallest particle size which can be deposited with sufficiently high efficiency and technical feasibility is about 0.5 [μm].[7]

Filter separators with cloth filter cannot be used at high temperatures as compared to the mass force separators and the e-filters. This type of filters can be still applied in aggressive environments and at high temperatures, if ceramic or sintered metal filters are used. However, these particular types of filter materials break more easily, when they are subject to strong operating temperature fluctuations. [7][10]

Summary of the separation methods

In table 1 the key parameters of the different separation methods are summarized for the sake of a better comparability. The methods are compared with regard to a minimal particle size, where a high degree of separation is still possible. The methods are further compared with regard to the maximal permissible raw and clean gas dust content, the pressure loss, maximum allowed gas temperature and flow capacity.

Table 1: Comparison of the different separation methods [8]

Characteristics	Cyclone separator	Wet separator	Electrostatic precipitator	Filtering separator
High degree of separation within particle size [µm]	>10	>0.1	>1	>0.5
Raw gas dust content [g/m³]	<1000	<10	<50	<100
Achievable clean gas dust content [mg/m³]	100-200	50-100	<50	<20
Pressure loss [Pa]	500-3 000	100-1 000	30-400	600-2 000
Max. gas temperature [°C]	450	3.000	450	260
Flow capacity [m³/h]	3 000-200 000	3 000-100 000	10 000-300 000	1 000-100 000

The comparison shown in table 1 makes evident that the filtering separators are the best solution in most cases. A big advantage of the filtering separators against the others is the low dust content on the clean side. This is explained by the fact that also very small particles can be separated as already mentioned in the previous chapter. On the other hand, their pressure loss is bigger than for most other separators.

1.2.2. Bag filters

The motivation and the goals of the present study can be better understood having some basic knowledge on bag filter separators. Therefore the different designs, functional principle, as well as the limits will be shortly reviewed in the following subsections. A bag filter system typically used in industry is shown in Figure 8.

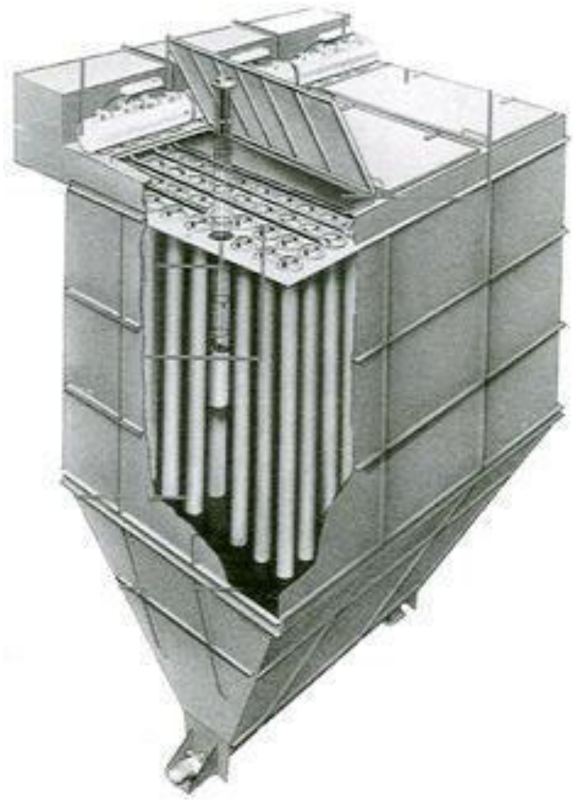

Figure 8: Pulse jet Bag filter [14]

As already mentioned, bag filters are classified as filter separators. More exactly, they belong to the category of surface filters. Since this is an important aspect when dealing with bag filters, it will be explained in more detail below.

The filtering process of surface filters can be basically divided into two phases. In the first phase the oncoming particles enter the filter medium and are collected by the filter cartridge. These particles block the filter element. After this initial contamination the particles do not enter the filter medium but are deposited on the surface of the filters, where they build a dust layer. The thicker the dust layer, the higher becomes the pressure loss across the filter cake. In order to keep the pressure loss below a certain limit, the filters have to be cleaned from time to time to operate efficiently. After such cleaning steps the pressure loss is reduced down to a certain level from where it rises again during the successive filtering phase. A typical pressure loss over the time is schematically shown in Figure 9. Stable and unstable processes are indicated additionally. A stable process means that the pressure loss drops to the same level each time the filter is regenerated. An unstable process may be caused by a too heavy deposition of the particles inside the filter, so that the filter it is clogged. In this case, the pressure loss after each regeneration step is notably increasing and finally exceeds the acceptable limits. Filters associated with such an unstable process and have to be replaced. [13]

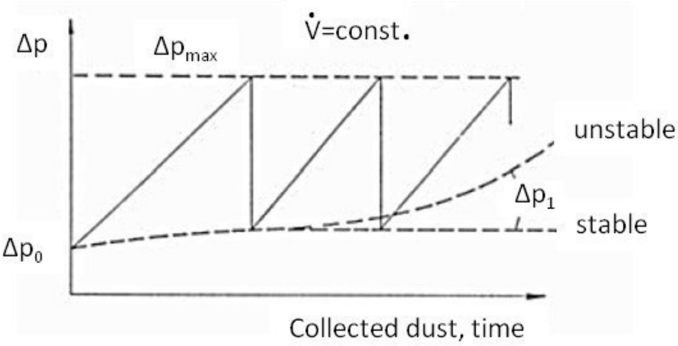

Figure 9: Pressure loss during collection time [13]

It is worth emphasizing that the regeneration frequency is also of relevance. Attention must be paid to minimize the regeneration frequency, since the particle concentration in the clean gas increase during pulsation generally used for cleaning. After cleaning, the concentration drops again. This effect follows from the fact that particles, migrated into the filter media, are redispersed, when the filter media hits back on the support cage. This cage is applied to support the filter on the inner side and prevent it from collapsing. The history of a typical concentration in the clean gas is schematically shown in Figure 10. One can see, that in the first few regenerations the concentration increases significantly and stabilises after some cycles. This stabilizing tendency is due, amongst other things, to the fact that the filter media has to find a stable state. [13]

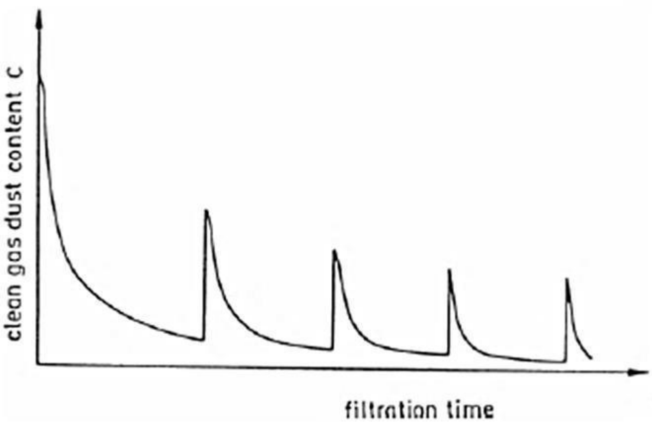

Figure 10: Particle concentration on clean air side [13]

In principle, it is necessary to distinguish between online and offline regeneration. Online means that the regeneration takes place during the filtering process. Offline, on the other hand, means that the dusty gas supply is closed during the regeneration. For filters regenerated online, the particle concentration in the clean gas depends on the cleaning method. The filters can be regenerated by knocking or shaking, reverse air or with a jet pulse. The operating principles of these different techniques are shown in Figure 11.

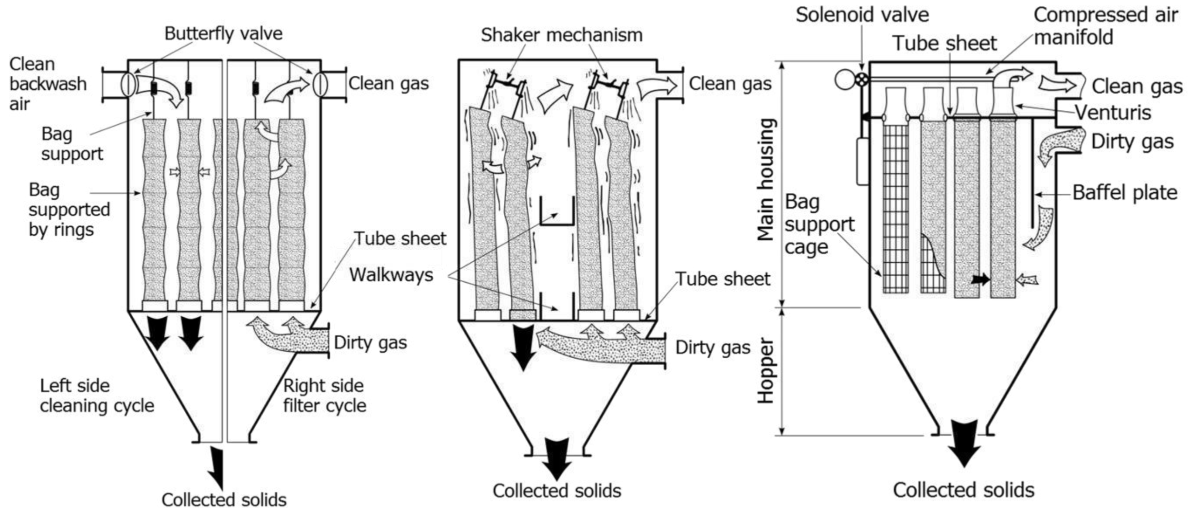

Figure 11: Different cleaning methods: a) dedusting by reverse air, b) Mechanical dedusting, c) Pulse Jet cleaning [15]

The basic design of this type of filters is approximately always the same. The dirty air is conducted into the filter bags supported by a tube sheet. Driven by the pressure difference the gas passes the filter material, where the particles are deposited on the inner side. The clean gas generally exits the filtering device through an outlet at the top. Several methods are applied for the regeneration of the filters. They will be briefly described below.

Dedusting by reverse air

In this method the filters are cleaned by simply operating the devise with a reverse air flow. The clean air penetrates the filter bags from outside, and thereby removes the collected dust layer on the inner surface of the bags. The filter bags are supported by rigid wire rings so that they do not collapse under the action of the cleaning air stream coming from outside. The deformation of the bags has to be still sufficiently large to remove the dust. [13]

This dedusting method is generally used in filter systems, which are divided into chambers working alternately in separator and regenerator mode. This operating principle allows a continuous process.

Mechanical dedusting

When dedusting the bag filters mechanically through shaking, the bags are mostly kept in a fixed position at the bottom and they are shaken at the top. The particles are also removed from the inner side of the bags, similarly to the dedusting by reverse air.

There are different shaking mechanisms which move the bags in different ways, as displayed in Figure 12. These mechanisms generate waves which are propagating from the top to the bottom of the bags and loosen the dust cake. The wavy motion of the bag sheds the particles off the filter surface. The design of such filters is very simple and is therefore often used in industry. [13]

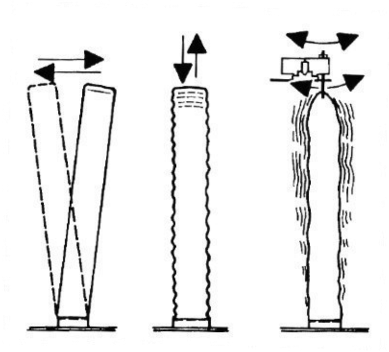

Figure 12: Different shaking mechanisms [16]

Dedusting by Pulse- Jet technology

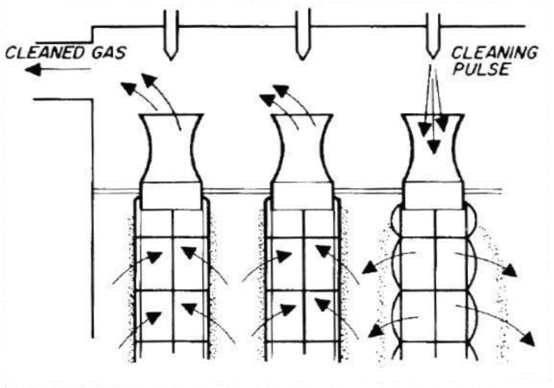

Figure 13: Schematic representation of a pulse jet cleaning device [16]

As third possibility of filter-cleaning is the so called pulse-jet technology. The biggest difference between this technology and the other two dedusting mechanisms is that the flow of the crude gas is fed from the other side. This means that the particles are separated on the outer surface of the bags. Similarly to the dedusting by reverse air, a support cage is needed to prevent the bag from collapsing during filtering. This has also an effect during the cleaning of the bags. The single bags are opened upwards which allow for a dedusting by an air impulse from above as shown in Figure 13. The needed air is fed from a pressure tank and is distributed over the individual bags by a distributor pipe, which is also called blow pipe. The escaping air impulse enters the bags and leads to a rapid increase in pressure inside, which causes a removal of the particles on the outer surface of the bags. A more detailed insight into this dedusting process is given in the next section.

The arrangement of the blow pipe and the bag filters beneath are shown in Figure 14, where it is schematically illustrated on the left side and on the right side a real blow pipe is shown. It becomes obvious, that on industrial scale several filter rows are supplied by one single pressure tank. It should be mentioned that only one row is dedusted at a time. When the pressure difference between the clean and dirty area reaches a critical value again another row is cleaned.

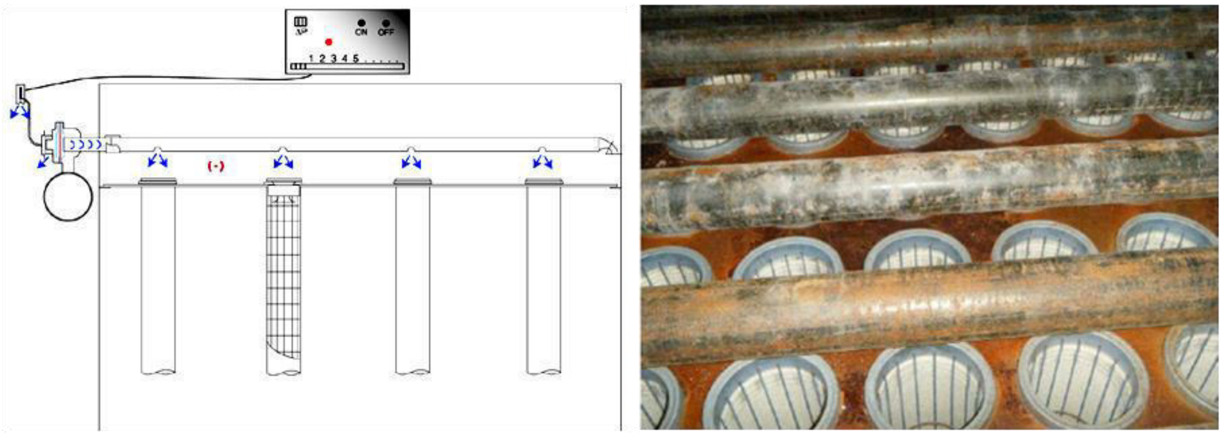

Figure 14: Schematic illustration of the blow pipe and the filter bags (left) and a real configuration (right) [17]

In Table 2 the three different bag filter cleaning systems are compared with respect to energy consumption, mean pressure loss and other key parameters. This comparison underlines the benefits of the Pulse-jet cleaning systems.

This system allows a much larger total filter area and a greater dust load permitted on the filters compared to the other cleaning methods. Those factors have a direct impact on the maximum gas flow rate possible. Only the lifetime of a single filter bag is shorter, however this issue is discussed later.

Table 2: Comparison of the different cleaning methods [18]

	Mechanical cleaning	**Reverse air cleaning**	**Pulse-Jet cleaning**
Gas flow rate [m^3/h]	500	1 000- 20 000	1 000- >2 000 000
Filter area [m^2]	5	20- 200	10- > 20 000
Filter area load [m^3/m^2 min]	0.7- 1.5	0.7- 1.7	0.5- 3
Dedusting	Shake/ Knock Low energy Only offline	Reverse air Low energy Only offline	Air pulse High energy Offline and online
Lifetime of filter elements [a]	4- 7	Max. 10	1- 5
Energy consumption [%] *	120	100	80
Mean system pressure drop [Pa]	2.000	1.600	1.200

* Energy consumption with respect to Reverse Air cleaning =100 [%]

1.3.Problem definition

After having briefly reviewed the basic principles of the different dedusting methods a closer look shall be taken at the Pulse-jet technology, where the presently considered compressible flow problem is met.

As already mentioned, a short intense air pulse is used to clean the filters. This short air pulse leads to a sudden increase of the pressure inside the filter bags which leads to an acceleration of the filter cloth into the radial direction, as it is illustrated in Figure 15. This dedusting concept allows for a clear distinction between the filtering and the regeneration process. During the filtering process the filter cloth is pressed radially inwards. During the regeneration process the filter cloth bulges radially so that the filter cake is thrown off from the outer surface. In the relaxation phase after the pressure pulse the filter cloth hits back on the support cage. Due to this impact small particles, which may have penetrated the filter tissue, can be dispersed again and contaminate the gas on the clean air side. The regenerations lead to high stresses of the filter cloth causing a considerable wear of the material dependent of the strength of the pressure pulse. For that reason, not all types of filter materials can be used. Many different types of filter materials exist, which have spacific advantages and disadvantages. Table 3 exemplarily lists some filter materials, how they are produced, and where they are used. [12]

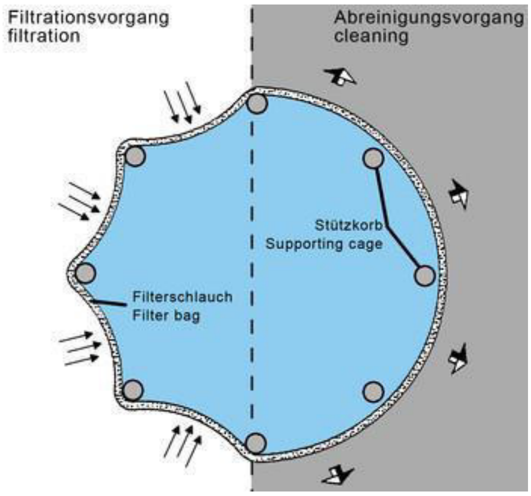

Figure 15: Cross section of a bag filter during filtration and cleaning [19]

Table 3: Comparison of different filter materials and their usual usage [18]

Filter materials	Types of construction	Usage
Tissue	Tissues made of synthetic, metal fibres and natural fibres, Mono-/ Multifilament	Mostly for mechanical dedusting
Needle felt	-	Mostly for filter bags and pockets with continuous compressed air cleaning
Fleece	Fleeces with bonding agents, Meltblown	Mostly for filter cartridges with continuous compressed air cleaning
Glass fibre	-	Mostly for HEPA filters, cassettes- and bag filters
Sintered filter elements	Sintered plastics, ceramic and metal elements	

Supply and distribution of pressurized air

The compressed air needed for the regeneration is supplied from a pressure vessel, whose pressure is maintained using an air compressor. A solenoid valve is installed at the outlet of the vessel to control the exit gas stream, as illustrated in Figure 16. During the filtering the valve is closed and the pressure inside the vessel remains constant somewhere within 3 up to 5 [bar].

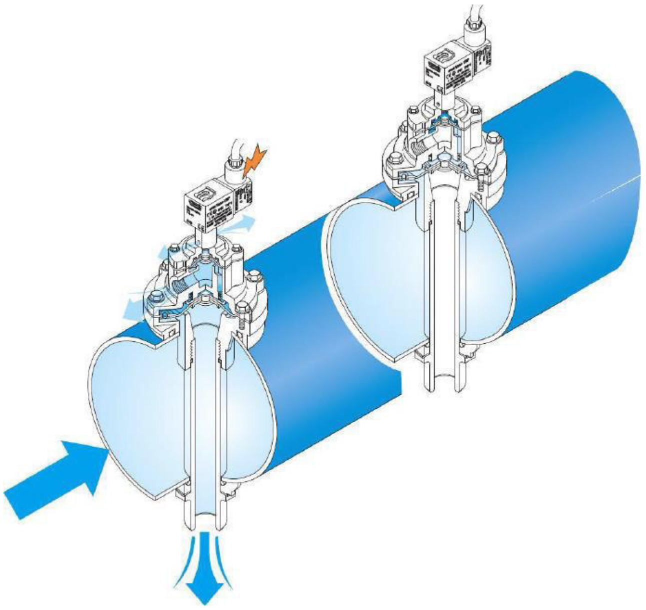

Figure 16: Solenoid valve in opened and closed position [17]

The closing force needed to lock the valve is generated from the pressure inside the vessel. If the pressure loss across the filters exceeds a certain limit, the valve opens so that the pressurized gas can expand through the exit. Due to this sudden expansion a shock wave is formed and is propagated through the blow pipe. On its way through the blow pipe it successively passes the individual exits to the filter bags, which receive a short pulse of compressed air used for dedusting their outer surface. There exist various different designs of the blow pipe, whose layout mostly follows some empirical principles, or, in other words, some rules of thumbs. For example, the ratio between the pipe diameter and the exit hole diameters should not exceed a given value. Nonetheless, the design of the blow pipe still varies from manufacturer to manufacturer. Some manufacturers, for example, have developed special outlets for the exit flow into the individual filter bags, ranging from simple slots to simple and short pipe ends attached at the individual outlets. Some manufacturers developed special shaped exit nozzles which are also attached at the individual outlets of the blow pipe, where they should produce pulse jets blowing into each filter bag with approximately the same axial momentum. Moreover, these nozzles should also minimize the pressure drop caused by the individual outlets. [20]

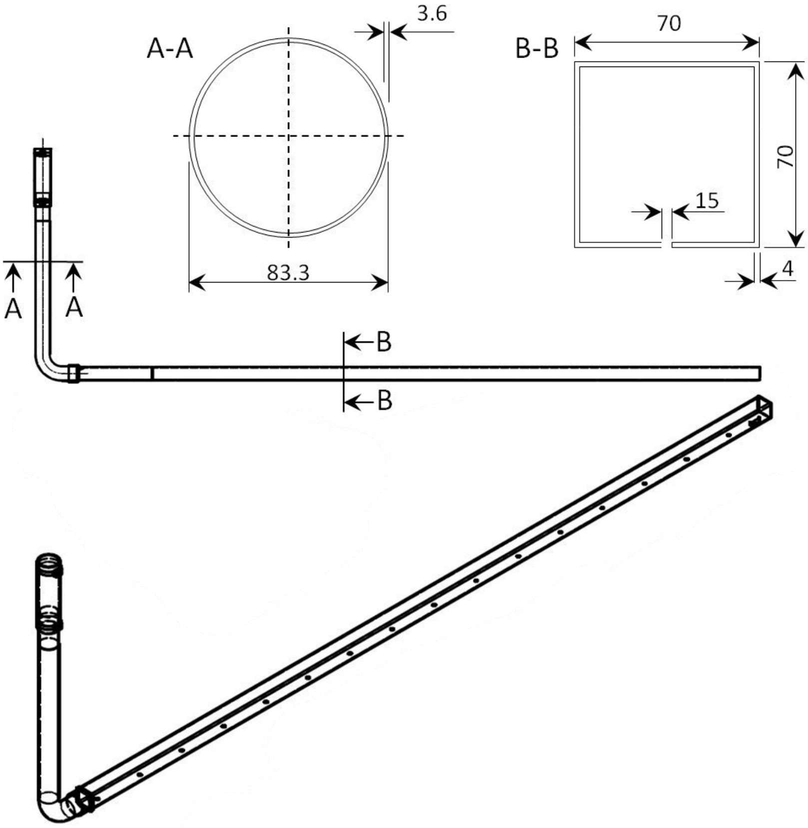

Figure 17: The blow pipe considered in this work, units in [mm]

The blow pipe investigated in this work is shown in Figure 17. The solenoid valve mounted at the inlet of the pipe is not shown in this illustration. Upon opening of the valve the air stream enters a vertical cylindrical section and is then redirected into the horizontal direction through the 90 degree bend. Downstream of the bend the flow enters a long straight channel with square cross-section. The bottom wall of this square channel is perforated by a number of equally distributed exit holes, which are looking to the aperture of the individual filter bags.

As already indicated above, various flow related problems can arise during the regeneration phase. The pulse jets, which are successively generated at each exit hole upon the passage of the pressure wave, can leave the blow pipe in non-perpendicular direction, or they differ significantly in terms of duration or axial momentum. These deficits inevitably lead to a sub-optimal dedusting and may also cause unacceptable high stresses exerted on some of the filters. In particular, an oblique ejection of the pulse jets leads to the problem that the jets do not hit the bags centrically, but may also strike the outer surface of the filters. Thus, not the whole amount of the ejected air enters the filter bag which may lead to poor cleaning. A non-uniform distribution of the exit air along the pipe results in different levels of dedusting among the individual filters. As a result, those filter bags which receive more air have to be exchanged more often, because they are subject to higher stresses. Exchanging the filters more often leads to unnecessary expense. On the other hand, those filters which receive less air are insufficiently cleaned and the dust cake is not removed completely. This results after several insufficient cleaning cycles in an agglomeration of the dust cake. This may also increase the mechanical stress on the filter, and static problems can occur as well.

1.4.Goal of this work

From the experience in various industrial plants it is apparent, that dedusting of bag filters is often far from being ideal. Especially the aforementioned non-uniform gas pulse distribution among the filters appears to be a very common deficit. So it is very often observed that filters positioned near the beginning of the blowing pipe are worse cleaned, which is indicated by caking of sedimented dust at the upper part of the bags. On the other hand the filters positioned near the end of the pipe end appear to receive an excessively high cleaning pulse causing much higher strain. This is indicated by the fact, that the filters located near the end often become worn out earlier and have to be replaced more frequently. Therefore, the layout of blow pipes has to focus the distribution of pulsed air among the individual exits. The present work tackles this problem by performing numerical flow simulations of the underlying unsteady compressible flow through the blow pipe and emerging the sequence of pulse jets used for dedusting.

2. Mathematical description

Fluid mechanics essentially attempts to provide a most realistic description of the motion of fluids. While simple strongly reduced problems can often be solved analytically, more complex problems can often only be solved numerically. In any case, it is always necessary to state at first the mathematical formulation of the governing conservation equations.

2.1. Conservation equations

The conservation principles relevant for fluid mechanics are in general the conservation of mass, momentum, and energy. The differential conservation equations of mass and momentum are mostly summarized as the *Navier-Stokes equations*, which represent the base for all CFD-programs. [21] The conservation equations are generally written as

$$\frac{\partial}{\partial t}(\rho \Phi) + \frac{\partial}{\partial x_i}(\rho u_i \Phi) = \frac{\partial}{\partial x_i}\left(\mathrm{D}\frac{\partial \Phi}{\partial x_i}\right) + Q_{\Phi} \qquad [2.1]$$

In this representation Φ indicates any conserved quantity considered in the flow system. The individual terms occurring in this equation are associated with the following physical meanings:

The first term on the left hand side denotes the transient term. It describes the local temporal change of the conserved quantity. The second term represents the transport of the conserved quantity due to convection. On the right side of the equation, the first term represents the diffusive transport involving the diffusion coefficient D. The second term on rhs is a volumetric source-term. The equations of conservation shall be rewritten below for the individual conserved quantities in compressible flow.

2.1.1. The Navier Stokes equations

Continuity equation

The equation of continuity describes the conservation of mass and can be written as

$$\frac{\partial \rho}{\partial t}+\frac{\partial}{\partial x}(\rho u_x)+\frac{\partial}{\partial y}(\rho u_y)+\frac{\partial}{\partial z}(\rho u_z)=0 \qquad [2.2]$$

As such the continuity equation states that mass cannot be neither destroyed nor produced. In the formula above the terms on the left side describe the local instantaneous change in density and the spatial change of the convective fluxes of mass into all directions, respectively.

Conservation of momentum

The equations of conservation of momentum essentially represent Newton´s second law, which states that the product of mass and acceleration is balanced by forces acting on the considered mass. The equations of momentum can be written for each direction of a Cartesian coordinate system (x, y, z) as

direction x:

$$\begin{aligned}\frac{\partial}{\partial t}(\rho u_x)+\left(\frac{\partial}{\partial x}(\rho u_x^2)+\frac{\partial}{\partial y}(\rho u_x u_y)+\frac{\partial}{\partial z}(\rho u_x u_z)\right)\\ =-\frac{\partial p}{\partial x}+\left(\frac{\partial \tau_{xx}}{\partial x}+\frac{\partial \tau_{yx}}{\partial y}+\frac{\partial \tau_{zx}}{\partial z}\right)+\rho f_x^B\end{aligned} \qquad [2.3]$$

direction y:

$$\begin{aligned}\frac{\partial}{\partial t}(\rho u_y)+\left(\frac{\partial}{\partial x}(\rho u_x u_y)+\frac{\partial}{\partial y}(\rho {u_y}^2)+\frac{\partial}{\partial z}(\rho u_y u_z)\right)\\ =-\frac{\partial p}{\partial y}+\left(\frac{\partial \tau_{xy}}{\partial x}+\frac{\partial \tau_{yy}}{\partial y}+\frac{\partial \tau_{zy}}{\partial z}\right)+\rho f_y^B\end{aligned} \qquad [2.4]$$

direction z:

$$\begin{aligned}\frac{\partial}{\partial t}(\rho u_z)+\left(\frac{\partial}{\partial x}(\rho u_x u_z)+\frac{\partial}{\partial y}(\rho u_y u_z)+\frac{\partial}{\partial z}(\rho {u_z}^2)\right)\\ =-\frac{\partial p}{\partial z}+\left(\frac{\partial \tau_{xz}}{\partial x}+\frac{\partial \tau_{yz}}{\partial y}+\frac{\partial \tau_{zz}}{\partial z}\right)+\rho f_z^B\end{aligned} \qquad [2.5]$$

The three equations of momentum shown above can be generally rewritten in index notation as

$$\frac{\partial}{\partial t}(\rho u_i)+\frac{\partial \rho u_i u_j}{\partial x_j}=-\frac{\partial p}{\partial x_i}+\frac{\partial \tau_{ji}}{\partial x_j}+\rho f_i^B \qquad [2.6]$$

with the indices i and j denoting the individual directions in Cartesian coordinates.

The first term on the left hand side of Eq. (2.6) represents the local temporal change of momentum into the direction *i*. The second term on left hand side describes the convective change of momentum. The forces occurring on the right hand side can be divided into surface and body forces. The first two terms, representing the pressure forces and the viscous friction forces, respectively, belong to the surface forces. The latter can be further divided into normal stress- and shear stress forces. The last term on rhs represents the body forces acting on the considered volume, such as gravitational forces, centrifugal forces, or electromagnetic forces etc.

The viscous friction force is basically obtained as the divergence of the stress tensor τ_{ij}, which can be written as

$$\tau_{ij} = \begin{bmatrix} \tau_{xx} & \tau_{xy} & \tau_{xz} \\ \tau_{yx} & \tau_{yy} & \tau_{yz} \\ \tau_{zx} & \tau_{zy} & \tau_{zz} \end{bmatrix}$$

Using Stokes friction law the single components of this tensor are obtained dependent of the strain rates as

$$\tau_{ij} = \mu \left[\frac{\partial u_i}{\partial x_j} + \frac{\partial u_j}{\partial x_i} - \frac{2}{3} \delta_{ij} \frac{\partial u_k}{\partial x_k} \right] \qquad [2.7]$$

Assuming Newtonian fluids (water, air, etc.) the molecular viscosity is independent of the strain rates.

2.1.2. Energy equation

Energy can exist in many forms, and it can be transformed from one form into another without any losses. One can generally distinguish between kinetic energy, thermal energy, and chemical bond energy. This work considers the energy equation without the chemical reactions, because chemically inert air is exclusively regarded as flow medium.

The energy equation can be generally written as [22]

$$\frac{\partial}{\partial t}\left[\rho\left(e+\frac{u_i u_i}{2}\right)\right]+\frac{\partial}{\partial x_j}\left[\rho u_j\left(e+\frac{u_i u_i}{2}\right)\right]= \\ \rho u_i f_i^B-\frac{\partial}{\partial x_j}\left(u_j p\right)+\frac{\partial}{\partial x_j}\left(u_i \tau_{ij}\right)-\frac{\partial}{\partial x_j} q_j+\dot{q}_Q\ , \qquad [2.8]$$

where e describes the specific internal energy, and $\frac{u_i u_i}{2}$ the specific kinetic energy, which can be combined to the so called total energy $\hat{e}=e+\frac{u_i u_i}{2}$.

In Eq. (2.8) the left hand side describes the local temporal and convective change of the total energy, respectively. The first three terms on the right hand side describe the power of the volume forces, pressure forces and viscous forces respectively. The last two terms describe the energy transport due to heat conduction and the power of internal heat sources.

The term for heat conduction can be described by Fourier´s law, $q_j=-\lambda\frac{\partial T}{\partial x_j}$, where λ describes the fluid conductivity [W/mK].

Based on the energy equation given by Eq. (2.8), another formulation of the energy equation can be derived. Subtraction of the mechanical contribution in the energy equation provides a transport equation for the specific internal energy, which can be written as:

$$\frac{\partial e}{\partial t}+u_i\frac{\partial e}{\partial x_i}+p\frac{\partial u_i}{\partial x_i}=\tau_{ij}\frac{\partial u_i}{\partial x_j}+\frac{\lambda}{\rho}\frac{\partial^2 T}{\partial x_i \partial x_i} \qquad [2.9]$$

The five differential conservation equations of mass, momentum, and energy are basically not sufficient to provide all unknown variables $(\rho, u_x, u_y, u_z, p, e, T)$. The thermal and caloric equations of state are therefore additionally needed to close the system. The thermodynamic equations of state basically allow expressing the pressure, density, internal energy, enthalpy, or temperature, as a function of two other state variables, which, e.g., for the pressure can be written as

$$p=p(\rho, e) \qquad [2.10]$$

The thermal equation of state relates the pressure to the density and temperature. Assuming perfect gas behaviour it reads [23] [24]

$$p=\rho R_s T \qquad [2.11]$$

In this equation, $R_S = R/M_G$ denotes the specific gas constant with R being the general molar gas constant, and M_G being the molecular weight of the flow medium.

The specific internal energy and enthalpy are related to the temperature through the specific heat capacities, which are generally defined as

$$c_v = \left.\frac{\partial e}{\partial T}\right|_{\rho=const.}, \quad c_p = \left.\frac{\partial h}{\partial T}\right|_{p=const.} \tag{2.12}$$

with $R_S = c_p - c_v$. For perfect gases with constant specific heat capacities, and hence, also a constant isentropic exponent $\kappa = c_p/c_v = const.$, the caloric equations of state read

$$e = \frac{1}{\kappa - 1}\frac{p}{\rho}, \qquad h = e + \frac{p}{\rho} = \frac{\kappa}{\kappa - 1}\frac{p}{\rho} \tag{2.13}$$

Introducing Eq. (2.13) into Eq. (2.9) finally leads to the following formulation of the energy balance

$$\frac{\partial p}{\partial t} + u_j \frac{\partial p}{\partial x_j} + \kappa p \frac{\partial u_j}{\partial x_j} = (\kappa - 1)\left(\tau_{ij}\frac{\partial u_i}{\partial x_j} + \lambda \frac{\partial^2 T}{\partial x_j \partial x_j}\right) = 0 \tag{2.14}$$

Non-dimensionalized conservation equations

The non-dimensional formulation is obtained by relating the individual variables to appropriate reference quantities. An order-of-magnitude analysis of the non-dimensionalized equations basically allows to identify the relevant terms in different asymptotic flow regimes, which can be suitably described by simplified formulations. Regarding the distinction between a compressible and incompressible flow regime the governing equations even require a very different solution method.

Introducing the reference quantities $L_0, u_0, p_0, \rho_0, \mu_0, \lambda_0$, the individual variables can be non-dimensionalized as [26]

$$x_i^* = \frac{x_i}{L_0}, \qquad t^* = \frac{t\,u_0}{L_0}, \qquad u_i^* = \frac{u_i}{u_0}, \qquad p^* = \frac{p}{p_0},$$
$$\rho^* = \frac{\rho}{\rho_0}, \qquad T^* = \frac{\rho_0 R_S T}{p_0}, \qquad \mu^* = \frac{\mu}{\mu_0}, \qquad \lambda^* = \frac{\lambda}{\lambda_0},$$

Using these quantities the non-dimensional conservation equations of mass, momentum, and energy read

$$\frac{\partial \rho^*}{\partial t^*} + \frac{\partial \rho^* u_i^*}{\partial x_i^*} = 0 \tag{2.15}$$

$$\frac{\partial \rho^* u_i^*}{\partial t^*} + \frac{\partial \rho^* u_i^* u_j^*}{\partial x_j^*} = -\frac{1}{\kappa M^2}\frac{\partial p^*}{\partial x_i^*} + \frac{1}{Re}\frac{\partial \tau_{ij}^*}{\partial x_j^*} + \frac{\rho^*}{Fr^2} \qquad [2.16]$$

$$\frac{\partial p^*}{\partial t^*} + u_j^*\frac{\partial p^*}{\partial x_j^*} + \kappa p^*\frac{\partial u_j^*}{\partial x_j^*} = \kappa(\kappa-1)\frac{M^2}{Re}\mu^*\tau_{ij}^*\frac{\partial u_i^*}{\partial x_j^*} + \frac{\lambda^*}{Re\,Pr}\frac{\partial^2 T^*}{\partial x_j^* \partial x_j^*}\,, \qquad [2.17]$$

respectively. They involve the Mach number (M), which is of high relevance when dealing with compressible flows, as will be shown in more detail below. The further occurring dimensionless numbers are the Reynolds number (Re), the Froude number (Fr), and the Prandtl numbers (Pr).

The Reynolds number describes the ratio of inertial forces to the viscous forces and is defined as[22]

$$Re = \frac{\rho_0 u_0 L_0}{\mu_0}. \qquad [2.18]$$

In internal flows through non-cylindrical pipes or channels the so called the hydraulic diameter is used as characteristic length $d_H = L_0$. It is defined as $d_H = 4A/U$ dependent of the cross-sectional area (A) and the circumference (U) of the considered channel. The Reynolds number is the decisive parameter for the occurrence of a laminar or turbulent flow regime. In case of a pipe flow the critical Reynolds number for the transition from laminar to turbulent flow is about 2300. For very large Reynolds number the effect of viscous forces can be neglected, and the Navier-Stokes equation can be reduced to the so called Euler equations valid for inviscid flow.

The Froude number defined as

$$Fr = \frac{u_0}{\sqrt{gL_0}} \qquad [2.19]$$

represents the ratio of inertial forces to gravitational forces [22]. This implies that for a large value of the Froude number the gravitational forces are small and can be neglected.

The Prandtl number defined as [22]

$$Pr = \frac{\mu_0 c_p}{\lambda_0} \qquad [2.20]$$

stands for the ratio of kinematic viscosity to thermal conductivity and thus links the velocity field with the temperature field of the flow. In wall bounded flow the Prandtl number thus represents the ratio of the thickness of the boundary layers of the velocity to the temperature. For most gases the Prandtl number is close to unity.

2.1.3. The Mach number

As already mentioned above, the Mach number plays a very prominent role in the context of compressible flow. It is defined as the ratio between the characteristic velocity scale to the isentropic speed of sound

$$M = \frac{u_0}{a_0} \qquad [2.21]$$

Recalling the definition of the isentropic velocity of sound [27]

$$a_0^2 = \left(\frac{\partial p}{\partial \rho}\right)_s \qquad [2.22]$$

this implies that incompressible flow, where the density is basically independent of the pressure, and hence $a_0^{-2} = (\partial\rho/\partial p)_s = 0$, is associated with zero Mach number. The relevance of the compressibility is therefore dependent of the magnitude of the Mach number. The lower limit for compressible flow is generally assumed as M≈0.3, which already requires relatively high flow velocities in most cases. The compressible flow regime occurring above this limit is often further divided into a subsonic (0.3<M<0.8), transonic (0.8<M<1.2) and supersonic (1.2<M<3) subregime. Flows with a Mach number larger than 5, are commonly called hypersonic. These are relevant for asteroids, or spacecraft when entering the atmosphere. [28]

Figure 18 a-d shows a moving source of sound to explain the different regimes based on the principles of wave propagation. If the source is not moving, the pressure (and density) disturbances associated with the sound waves spread out in concentric spheres into all three dimensions. If the source moves slower than the velocity of sound, $W < a_0$, the disturbances spread not spherically symmetric, as shown in Figure 18 b. If the source moves at the velocity of sound, $W = a_0$, all disturbances coincide at one point moving at sound speed. For $W < a_0$the motion is faster than the speed of sound and the disturbances spread inside a Mach cone moving with the velocity W.

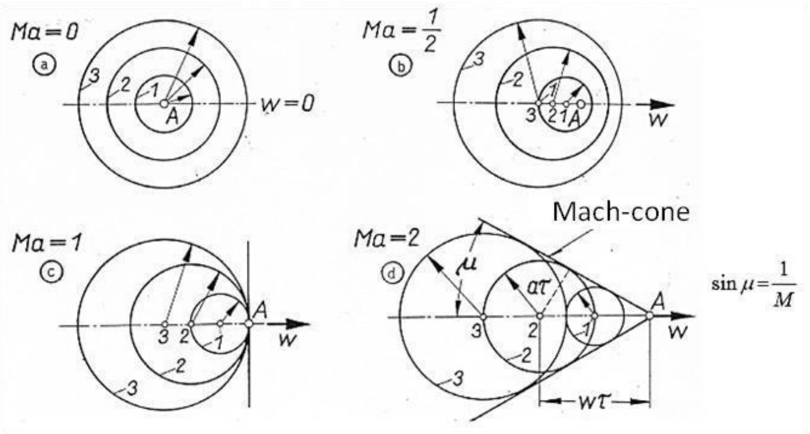

Figure 18: Spreading of the disturbances at different Mach-numbers [28]

In Table 4 some examples of flows with their typical range of Mach numbers are shown. [29]

Table 4: Flow configurations and their typical range of mach numbers

Example	Mach number	Example	Mach number
Vent pipe	0.1	Steam turbine	0.7
Vehicle flow	0.2- 0.3	Commercial aircraft	0.85
Wind rotor	0.2- 0.5	Blast wave	>1.5
Discharge of pressure vessels	0.5- 1.5		

A typical flow phenomenon in a compressible fluid is the propagation of a sound wave. A sound wave essentially represents a disturbance in density and pressure which is propagated through the medium at a certain speed (speed of sound). Upon the passage of the disturbance the medium undergoes an infinitesimal change in pressure, density, temperature, and velocity. This is schematically shown in Figure 19 in a fixed frame of reference on the left hand side, and in frame of reference moving at sound speed on the right hand side. Accordingly, the propagating sound wave appears as stationary in the latter, and it faces an oncoming gas flow at the velocity $u = a$.

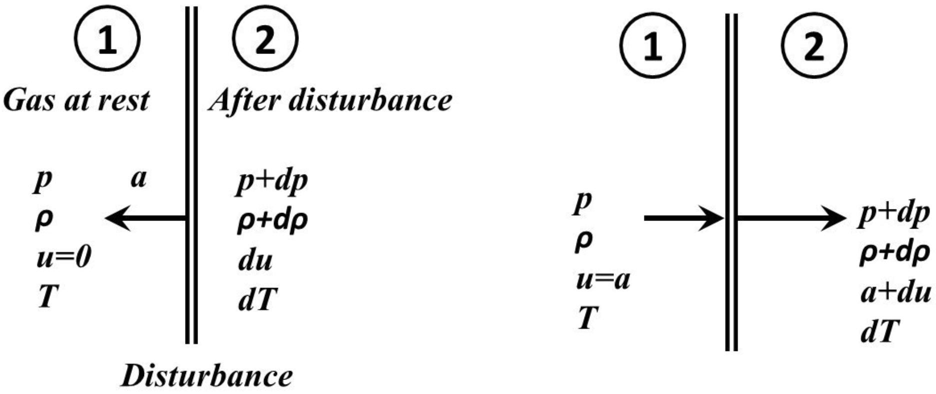

Figure 19: The conditions before (1) and after (2) the sound wave

For the system shown on rhs of Figure 19 we can write the balances of mass and momentum as

$$a\rho = (a + du)(\rho + d\rho) \tag{2.23}$$

$$p + a^2\rho = (p + dp) + (a + du)^2(\rho + d\rho), \tag{2.24}$$

respectively. Combining these two equations, which basically describes the propagation of a pressure wave of infinitesimal strength, leads to the already shown definition of the isentropic velocity of sound written as [27]

$$a^2 = \left(\frac{\partial p}{\partial \rho}\right)_s \tag{2.25}$$

For a perfect gas with constant isentropic exponent κ, and further recalling the isentropic law

$$\left(\frac{p}{p_0}\right) = \left(\frac{\rho}{\rho_0}\right)^{\kappa} = const. \tag{2.26}$$

the isentropic speed of sound is obtained as

$$a^2 = \kappa\frac{p}{\rho} = \kappa R_S T \tag{2.27}$$

2.2.One-dimensional description of compressible flow along stream tubes

The theory of flow filaments essentially solves the Euler equations valid for inviscid compressible flow along stream tubes with an infinitesimal cross-section dA. The Euler equations applied to a small volume element $dV = dAds$ being part of such a stream tube, as shown in Figure 20, are written as[30]:

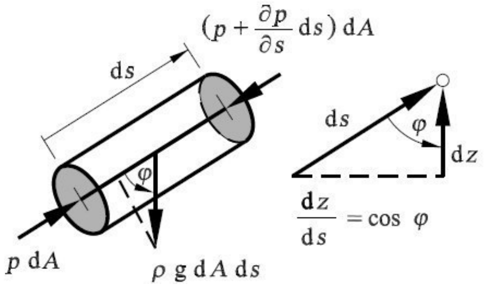

Figure 20: forces on volume element [30]

$$\frac{du}{dt} = \frac{\partial u}{\partial t} + u\frac{\partial u}{\partial s} = -\frac{1}{\rho}\frac{\partial p}{\partial s} - g\frac{dz}{ds} \tag{2.28}$$

Assuming stationary flow and introducing the isentropic speed of sound, the Euler equation for steady compressible flow becomes

$$u\frac{du}{ds} = -\frac{1}{\rho}\frac{dp}{ds} = -\frac{1}{\rho}\frac{d\rho}{d\rho}\frac{dp}{ds} = -a^2\frac{1}{\rho}\frac{d\rho}{ds} \tag{2.29}$$

Dividing this equation by a^2, further multiplying it with ds and using the definition of the Mach number according to equation 2.22, it follows

$$\frac{d\rho}{\rho} = -M^2\frac{du}{u} \tag{2.30}$$

Combining the equation above with the continuity equation, which states $\rho u A = const.$, three different situations are possible[30] [31]. These are related to the change in the cross sectional area of the stream tube. In case of subsonic flows, the cross sectional are has to be reduced in order to accelerate the flow. Conversely, in case of supersonic flows, a cross-section expansion is required to accelerate the flow. These types of nozzles are, for example, the Laval- nozzle. This in turn means that the maximum possible flow velocity in a tube with a constant cross sectional area is equal the velocity of sound. This state is also termed as *choked*, and is of great importance for the prescription of the flow boundary conditions in the presently considered flow problem. The integration of the Euler equation along a certain portion of the stream tube extending from position s_1 to position s_2 yields the Bernoulli equation for compressible flow

$$\frac{1}{2}(u_2^2 - u_1^2) + \int_{p_1}^{p_2} \frac{dp}{\rho} = 0 \tag{2.31}$$

Expressing the density with the isentropic law $p\rho^{-\kappa} = const.$ the Bernoulli equation finally reads

$$\frac{1}{2}u_2^2 + \frac{\kappa}{\kappa - 1}\frac{p_2}{\rho_2} = \frac{1}{2}u_1^2 + \frac{\kappa}{\kappa - 1}\frac{p_1}{\rho_1} \tag{2.32}$$

Applying this equation to a stream tube extending between some point well inside a pressure vessel, where the static vessel conditions, $p_0, \rho_0, T_0, u = 0$, are met, and the exit cross-section of the outlet channel of the vessel, the thermodynamic state at the exit can be related to the static vessel conditions dependent of the exit Mach number M written as

$$\frac{p_0}{p} = \left(1 + \frac{\kappa - 1}{2} M^2\right)^{\frac{\kappa}{\kappa-1}}, \qquad \frac{\rho_0}{\rho} = \left(1 + \frac{\kappa - 1}{2} M^2\right)^{\frac{1}{\kappa-1}}, \qquad \frac{T_0}{T} = 1 + \frac{\kappa - 1}{2} M^2. \tag{2.33}$$

Assuming a straight pipe or converging nozzle at the exit the flow can isentropically expand to a state with unity Mach number at maximum. This unity Mach number condition is generally termed *blocked* or *critical outflow condition*. A transition to supersonic flow, which means a further increase of the Mach number beyond unity, would require an axial increase in cross-section as realized in the diverging part of a Laval nozzle. The critical outflow conditions are obtained by setting $M = 1$ in Eqs. (2.33). Assuming air with $\kappa = 1.4$ the critical ratios read

$$\frac{\hat{p}}{p_0} = \left(\frac{2}{\kappa + 1}\right)^{\frac{\kappa}{\kappa-1}} = 0.528, \qquad \frac{\hat{\rho}}{\rho_0} = \left(\frac{2}{\kappa + 1}\right)^{\frac{1}{\kappa-1}} = 0.634, \quad \frac{\hat{T}}{T_0} = \frac{2}{\kappa + 1} = 0.83\dot{3}. \tag{2.34}$$

The critical conditions stated above will be used to provide appropriate inflow conditions for the present numerical simulations of the compressible flow through the blow pipe, as shown below.

Calculation of the inflow boundary conditions

The prescription of the inflow conditions at the inlet of the blow pipe is based on the assumption that the flow expands isentropically from given static vessel conditions, determined by p_0 and T_0, to a blocked state associated with $M = 1$ at the inlet cross-section. The fluid mechanical losses due to the valve, which would basically lead to an increase in entropy, are neglected. The dynamic inflow boundary conditions are prescribed in terms of a critical mass flux, $\dot{m}_{in}[\frac{kg}{s\,m^2}]$, which is obtained from the critical ratios given in Eqs. (2.34) as follows:

recalling

$$\frac{\hat{\rho}}{\rho_0} = \left(\frac{2}{\kappa + 1}\right)^{\frac{1}{\kappa-1}}, \quad \frac{\hat{T}}{T_0} = \left(\frac{\hat{a}}{a_0}\right)^2 = \frac{2}{\kappa + 1} \tag{2.35}$$

we finally obtain with $u = a$, due to $M = 1$,

$$\hat{\dot{m}} = \hat{\rho}\hat{u} = (\kappa p_0 \rho_0)^{\frac{1}{2}} \left(\frac{2}{\kappa + 1}\right)^{\frac{\kappa+1}{2\kappa-2}} \tag{2.36}$$

3. Numerical simulations

In the following chapter the procedure of CFD simulations is briefly explained. The numerical setup which is particularly used for the present computations is explained in more detail. Two commercial programs have been used. The generation of the computational meshes for the studied geometries has been carried out with the pre-processing tool Gambit. Gambit is a quick and easy to learn mesh generating program, which originally served as meshing tool for the flow solver package Ansys Fluent. Ansys Fluent is used as flow solver for the present simulations, and it already provides its own mesh generator as a part of the software package. Meshes generated with Gambit can still be used.

3.1.Principals of numerical simulation

Due to the fact that most flows are very complex and only some special cases can be solved analytically (e.g. the boundary layer flow along a flat plate), most problems have to be solved numerically. The numerical simulations essentially solve a discretized representation of the governing set of differential conservation equations. The accuracy of the numerically obtained approximate solution strongly depends on the errors introduced by the discretization in time and space, the solution method applied to the discretized equations, and the individual model assumptions to be made for the description of the considered physical phenomena.

The typical workflow of numerical simulations is basically the same for all popular CFD programs (Ansys CFX, Ansys Fluent, OpenFoam etc.). At first, the considered problem has to be defined and a geometrical model of the flow domain has to be generated. For this purpose, program tools implemented in Ansys Fluent, or external programs can be used (Gambit etc.). Already at this point, care must be taken to design the geometry wisely to ensure a simple setting of the boundary conditions. The boundary conditions have a significant impact on the obtained results and must therefore be chosen carefully.

In a next logical step, the created geometry has to be subdivided into small elementary cells, the so called mesh. The mesh also has an important influence on the solution and thus, some quality criteria should be met. A bad quality of the mesh can lead to very inaccurate solutions or even a divergence of the whole simulation.

After these so called pre-processing steps, the actual simulation can be performed. This is in general an iterative process, where the solution is successively approximated to finally reach a converged solution. The so called residuals are used to quantify the deviation from the converged final solution, and shall be as small as possible.

As the last step, the obtained results have to be analysed and interpreted. This so called post-processing step deserves particular attention, because it is a prerequisite to use the obtained results in a conceivable way.

3.2.Numerical discretization

For the numerical solution of the governing differential equations, the equations have to be transformed into a discrete representation, which can be handled by digital computers. This transformation of the non-linear differential equations into a set of algebraic equations is called discretization. For this purpose several methods exist. The most widely used methods are the *finite elements*, *finite difference,* and the *finite volume method*. In numerical flow simulation the method of finite volume is most commonly used. Since this method is also implemented in Fluent, it will be discussed a little in more detail in the following subsection.[33] [34]

Finite volume method

This discretization method is based on the concept of subdividing the whole flow region into many smaller volumes, which constitute the so-called computational mesh. The individual adjacent cells of the mesh share common boundary faces and never overlap. The finite volume methods (FVM) allows for the usage of an unstructured mesh. This can be seen as an advantage over the finite difference method (FDM), since the usage of different topologies makes it easier to discretize complex geometries, and to locally refine the mesh. These local refinements of the mesh are necessary to resolve areas with large gradients properly. [34] [35] [36]

In each cell of the mesh the whole governing set of conservation equations is solved. As such FVM represents the integral form of the conservation equations applied to each cell. FVM allocates the obtained results at the centre of each cell, which used to interpolate the corresponding values on the surface of each cell as needed for the calculation of the fluxes. The calculation of the fluxes plays a key role in the FVM, because the estimation of the flux terms essentially determines the main discretization error. This error is mostly second-order.

3.3.Solver settings

Two different types of solver are implemented in Fluent for solving the integral balances over each individual computational cell: the *Pressure-Based Solver* and the *Density-Based*. The choice of the adequate solver type essentially depends of the relevance of the fluid´s compressibility in the considered problem. The Pressure-Based Solver is applied, when dealing with incompressible and slightly compressible fluids. In contrast, the Density-Based Solver is used when the flow medium is compressible and the Mach number is close to unity or higher. This work solely deals with near unity Mach number flow involving the propagation of a shock wave, which requires the use of the Density-Based Solver. In order to provide a better understanding of the operating principle, this solver is explained in more detail in the next few lines.

Density –Based Solver

This implemented solver solves the whole set of coupled conservation equations simultaneously. In doing so, the continuity equation is used to obtain the density field and the momentum equations are used to calculate the velocity field. The energy equation serves to calculate the specific internal energy or the enthalpy. Dealing with compressible flows, the pressure is obtained as a function of density and specific internal energy or enthalpy using the thermodynamic equation of state, as already explained in a previous section. It should be noted, that the material properties of the fluid have a significant influence on the results. Thus, they are updated in each iteration step.

As described above the Density-based solution method solves the set of conservation equations simultaneously. This can be done by using the so-called explicit formulation or the implicit formulation. The main difference between those is the way they linearize the set of equations. The explicit formulation requires less memory than the implicit formulation. That makes it first choice for transient simulations, as regarded in this work. A Runge-Kutta solver is used in Fluent for the explicit solution.[37] [38]

3.4.Turbulence model

In general three different approaches for simulating turbulence flows can be distinguished. The method of DNS (Direct Numerical Simuation) resolves directly the full spectrum of turbulent motion on all relevant scales. As such this concept requires a very high numerical resolution, which makes it computationally too expensive for turbulent flows at technically relevant high Reynolds numbers. The approach of the LES (Large Eddy Simulation) solves only the large turbulent structures directly, while the smaller structures are described by models. The computational costs of this approach are less than for DNS, but still often too high for engineering applications. The third possibility for describing turbulent flow is the so-called RANS approach. This abbreviation stands for *Reynolds-Averaged-Navier–Stokes* and provides the most widely used approach. It represents a statistical method, where the Navier-Stokes equations are ensemble averaged and solved for the ensemble averaged flow variables. [24] [28]

The RANS equations still contain non-linear terms, which are called *Reynolds stresses*. The name can be deduced from the fact that they appear as an additional stress tensor, which can be written as

$$\tau_{ij}{}^{R} = -\rho\overline{u_i{}'u_j{}'}, \qquad [3.1]$$

where u'_i denote the instantaneous turbulent fluctuation around the corresponding average $\overline{u_i}$. The elements of this tensor are unknown terms, so that additional equations are needed to describe them, which is the so-called closure problem of turbulence. Closure has to be provided by a turbulence model, which computes the Reynolds stresses solely as a function of the averaged flow variables. Boussinesq was one of the first who tackled this problem. Boussinesq basically assumes the Reynolds stresses as proportional to the mean velocity gradients written as

$$\rho\overline{u_i{}'u_j{}'} = -\mu_t\left(\frac{\partial\bar{u}_i}{\partial x_j} + \frac{\partial\bar{u}_j}{\partial x_i} - \frac{2}{3}\frac{\partial\bar{u}_k}{\partial x_k}\delta_{ij}\right) + \frac{2}{3}\rho k\delta_{ij}. \qquad [3.2]$$

In analogy to the viscous stress tensor, which involves the molecular viscosity (μ), the so-called turbulent viscosity (μ_t) is introduced to describe the transfer of momentum caused by turbulent eddies. Thus this parameter has to be rather considered as a local flow dependent quantity describing the turbulent motion, and not as a fluid property. Even if the approach of Boussinesq is in principal limited to isotropic turbulent flow in local equilibrium, it represents the basic assumption of most turbulence models used in today´s CFD. These turbulence models in general solve for one to several additional equations to determine this turbulent viscosity. Accordingly, the turbulence models can be subdivided into the following groups: [35]

- One-equation models (Spalart Allmaras model)
- Two equation models (Standard-k-ε, RNG-k-ε, Realizable-k-ε, k-ω, SST-k-ω)
- Reynolds stress model-RSM

The following paragraphs briefly describe the basic features of the one-equation, as well as the RSM-model. The two-equation models are explained in a little more detail, because these are widely used. One particular representative of this group is also applied in this work, the realizable $k-\varepsilon$ model.

One-equation models

The most common one-equation model in numerical simulation is the Spalart Allmaras model [35] [39]. It is often used for compressible external flow around airfoils. In this model one equation is solved for the transport of the turbulent viscosity. Similar to other scalar transport equations, this equation contains formation, destruction and diffusion terms. Near solid walls a damping function is used to decrease the turbulent viscosity.

Two-equation models

In contrast to the Spalart Allmaras model the two-equation models solve two transport equations for turbulent scalar quantities like k and ε, or k and ω to provide closure for the turbulent viscosity (μ_t). The *Standard-k-ε* model is the most frequently used approach in numerical simulation of turbulent flow [35][40][41]. Both quantities k and ε represent characteristic turbulent properties of the flow. k represents the kinetic energy of the turbulent motion, and ε the turbulent dissipation rate. The transport equations solved for k and ε are written as

$$\frac{\partial}{\partial t}(\rho k)+\frac{\partial}{\partial x_i}(\rho k\bar{u}_i)=\mu_t\frac{\partial \bar{u}_j}{\partial x_i}\left(\frac{\partial \bar{u}_j}{\partial x_i}+\frac{\partial \bar{u}_i}{\partial x_j}\right)+\frac{\partial}{\partial x_i}\left[\left(\mu+\frac{\mu_t}{\sigma_k}\right)\frac{\partial k}{\partial x_i}\right]-\rho\varepsilon\,, \qquad [3.2]$$

$$\frac{\partial}{\partial t}(\rho \varepsilon)+\frac{\partial}{\partial x_i}(\rho \varepsilon\bar{u}_i)=C_{\varepsilon 1}\frac{\varepsilon}{k}\mu_t\frac{\partial \bar{u}_j}{\partial x_i}\left(\frac{\partial \bar{u}_j}{\partial x_i}+\frac{\partial \bar{u}_i}{\partial x_j}\right)+\frac{\partial}{\partial x_i}\left(\frac{\mu_t}{\sigma_\varepsilon}\frac{\partial \varepsilon}{\partial x_i}\right)-C_{\varepsilon 2}\rho\frac{\varepsilon^2}{k}\,, \qquad [3.3]$$

where $\bar{u}_i$ denotes the Reynolds-averaged velocity component in the direction i. The variables $C_{\varepsilon 1}$ and $C_{\varepsilon 2}$ represent constants with a value of $C_{\varepsilon 1}=1.44$ and $C_{\varepsilon 2}=1.92$. The terms on the left hand side describe the temporal and the convective change of the quantities. A formation-, diffusion- and a destruction term appears on the right side of the equations, respectively. Using k and ε obtained from (3.2)- (3.3) the turbulent viscosity is computed as

$$\mu_t = \rho C_\mu \frac{k^2}{\varepsilon}, \qquad [3.4]$$

where C_μ=0.09 represents a model constant.

Since the model is so often used, its strengths and weaknesses are well documented. A typical limitation of the model is for example the fact that it has been developed for high Reynolds numbers, where isotropic flow can be assumed. Further limitations appear in more complex flow geometries, for example, involving high pressure gradients, flow separation or strongly curved streamlines, where the predictions become very inaccurate. [25]

Various attempts were made to eliminate some limitations of the Standard-k-ε model. A technique, used in statistical physics, the so-called Renormalization is adopted in the RNG-k-ε model. The quantity of k is computed from the same equation as in the Standard-k-ε model, while the dissipation rate ε is calculated using a formulation different from Eq. (3.3). This approach was shown to be more accurate in complex boundary layer flows with higher pressure gradients, or flows with weak swirl and flow separation. [24][25]

A second advancement of the Standard-k-ε model is the Realizable-k-ε model. The quantity k is again calculated as in the Standard-k-ε model, but the equations for ε as well as for the turbulent viscosity are modified introducing a further formation term in the first. The equation for the turbulent viscosity (3.4) is modified including the mean shear rate and the mean rotation of the flow field. This improvements lead to better results when flow separation occurs, where the standard $k-\varepsilon$ model is generally too conservative. This means the region, where the flow is attached is predicted much larger than it is in reality. For this reason the realizable $k-\varepsilon$ model is also used in this work.

Besides the two-equation models based on k and ε, there are also approaches using k and ω. ω describes the characteristic frequency of the energy-supporting vortices and is defined as:

$$\omega = \frac{\varepsilon}{k}. \qquad [3.5]$$

This model approach generally provides better results for the mean turbulent quantities near solid walls, than the Standard-k-ε model. In zones remote from the wall the model is less accurate. In this region the Standard-k-ε provides better results.

In order to combine the advantages of the k-ω model and the k-ε model, the SST-k-ω model has been developed. This model exploits the strengths of both two-equation models. The k-ω model is used in near wall regions, whereas in regions remote from walls the Standard-k-ε model comes into play.

Reynolds stress model (RSM)

This model calculates the Reynolds stresses directly from respective transport equations. The solution of a transport equation for ε is needed as well. Overall, in a 2D-case five and in a 3D-case seven additional equations have to be solved for the Reynolds stresses and the quantity for ε. This increases significantly the computational costs. As compared to the two-equation models the RSM-method is more accurate when dealing with very complex flow problems. Nonetheless, it must be said that the improvements do often not pay off the high computational costs, which is mainly due to the modelling of the transport equation for ε. [25]

3.5.Boundary-/ and initial conditions

The solution of the considered unsteady compressible flow problem requires an appropriate setting of the boundary conditions as well as initial conditions. The presently used conditions and their definition are described below.

3.5.1. Initial conditions

The initial conditions describe the state of the system at starting time *t=0*. In the present work the solenoid valve is assumed as closed at *t=0*, so that the fluid in the whole computational domain is at rest. The pressure, as well as the temperature inside the whole domain is set equal to the ambient reference conditions. The used initial conditions are summarized in the table below. It is noted that the pressure represents here the over-/underpressure relative to the ambient reference value.

Table 5: Initial conditions

Initial condition	Value	Unit
Pressure	0	[Pa]
Velocity (x,y,z)	0	[m/s]
Temperature	300	[K]

3.5.2. Boundary conditions

The presently considered computational domains are bounded by fixed walls, and open inlet and outlet surfaces, which require all physically meaningful settings. Symmetry conditions are used, wherever symmetry planes can be identified, in order to reduce the size of the computational domain. The computational domain with the individual boundaries is shown for a presently simulated three-dimensional case in Figure 21.

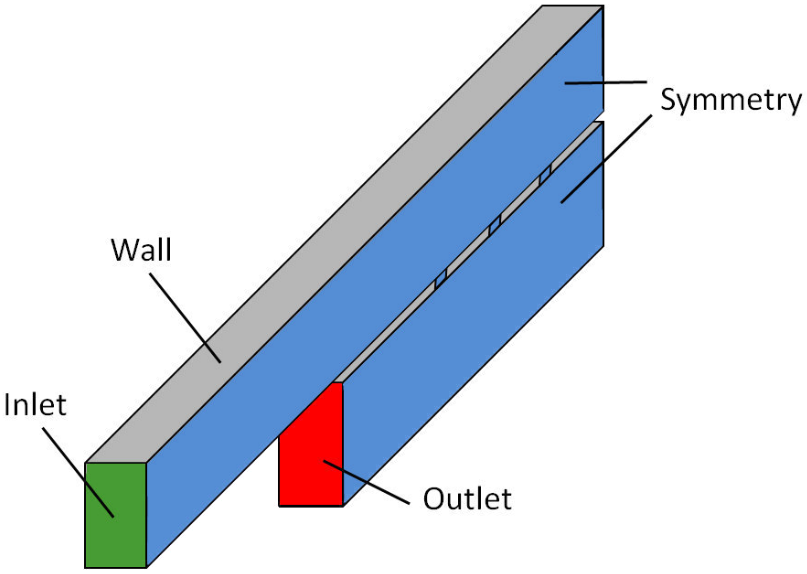

Figure 21: Sketch of a three-dimensional domain (see case C2 discussed in section 4.5) considered in the present simulations indicating the different boundaries

Wall boundaries

No-slip condition is set at all wall boundaries. Dealing with turbulent flow these no-slip conditions are prescribed in terms of the so-called Standard wall functions. This approach is based on the considerations of Launder and Spalding (1974) and is one of the most widely used in RANS-type CFD of turbulent flow. The dimensionless wall coordinates $y^* = \frac{y u_\tau}{\boldsymbol{\nu}}$ and $u^* = \frac{\bar{u}}{u_\tau}$ represent the dimensionless wall distance and dimensionless velocity, respectively, which are based on the wall friction velocity $u_\tau = \sqrt{\frac{\tau_w}{\rho}}$ and $l_\mu = \frac{\mu}{\rho u_\tau}$ as reference scales. Depending of the value of y^* the velocity in wall coordinates can be written as [21]

$$u^* = \begin{cases} y^* & \text{for } y^* < 11.225 \qquad [3.6] \\ \frac{1}{\kappa_t}\ln(E y^*) & \text{for } y^* > 11.225 \qquad [3.7] \end{cases}$$

where κ_t represents the von-Kármán-constant ($\kappa_t = 0.41$) and E an empirical constant ($E = 9.793$). For more details on the Standard wall function the reader is referred to the Ansys Theory Guide. [21]

Inlet boundary

Special attention had to be paid to the prescription of physically realistic boundary conditions at the inlet. At the inlet cross-section the pipe is basically connected through a solenoid valve with the pressure tank. Since the full numerical description of the detailed flow geometry inside the valve would be computationally too costly, a simplified transient inflow condition was assumed. Upon opening of the valve it is assumed that the gas exits from the tank (with given constant stagnation pressure p_0 and density ρ_0 inside) reaching rapidly the critical mass flux $(\hat{m})$ associated with unity Mach number as obtained from Eq. (2.36). Also the closing of the valve is considered in the performed simulations, where the mass flux drops from the critical condition to zero. Accordingly, three distinct phases were specified to prescribe this scenario from the opening to the closing at the inlet:

$$0 \leq t \leq t_I \qquad \dot{m}_{in} = \frac{1}{1+e^{(-a(t-\theta_{open}))}}\hat{m} \qquad [3.8]$$

$$t_I < t \leq t_{II} \qquad \dot{m}_{in} = \hat{m} \qquad [3.9]$$

$$t_{II} < t \leq t_{end} \qquad \dot{m}_{in} = \left(1-\frac{1}{1+e^{(-a(t-\theta_{close}))}}\right)\hat{m} \qquad [3.10]$$

with:

$t_I = 0.001\ [s], t_{II} = 0.004\ [s]/\ 0.0062\ [s], t_{end} = 0.02\ [s]$

$a = 8000\left[\frac{1}{s}\right],\ \theta_{open} = 0.0005\ [s], \theta_{close} = 0.0045/\ 0.0067[s]$

It is noted that the closing phase was not started at the same instant of time for all simulations. In the particular case V the duct extended by an additional volume at the end the closing was imposed later, for $t > t_{II} = 0.0062\ [s]$. The evolution of the mass flux prescribed at the inlet during the three phases is shown in Figure 22. The time dependent inlet mass flux was implemented in Fluent as User Defined Function (UDF).

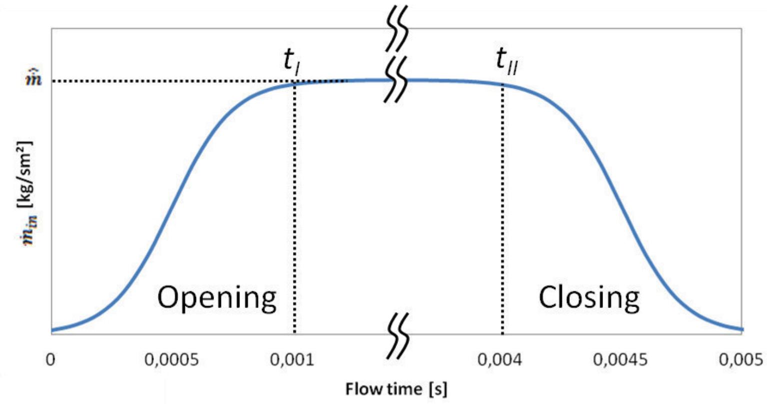

Figure 22: Prescribed time dependent mass flux at the inlet

Outlet boundary

All open surfaces aside from the inlet cross section were always assumed as so-called *pressure outlet* condition, where a constant ambient pressure is prescribed. As such this outlet boundary condition allows for flow outwards from as well as backwards into the domain. It should be posed far away from strong gradients of the relevant flow quantities to avoid instabilities.

Symmetry

For the sake of computational efficiency it is very useful to identify possible symmetry planes already when defining the geometry of the computational domain. In all presently considered three-dimensional simulations the flow field is symmetric with respect to the meridional cutting plane through the distributor duct in the streamwise direction. The symmetry conditions imposed at this plane prescribe zero gradients for all flow variables and zero normal velocity component. Table 6 summarizes the presently used boundary conditions. [42]

Table 6: Boundary conditions used

Boundary condition	
Wall	No-slip condition, Standard wall function
Inlet	Mass-flux prescribed by an UDF
Outlet	Pressure outlet imposing constant ambient pressure

4. Results

In this chapter the results of all performed simulations are discussed and analyzed. The simulations considered cases with increasing geometrical complexity to come finally fairly close to the conditions in the real application sketched in Figure 17. A full size simulation of the real application was beyond the scope of the present work due to the prohibitively high computational costs. The simulations can be distinguished into two- and three-dimensional computations, which are further indicated by the indices P (planar) and C (cubic), respectively.

The two-dimensional treatment of the present duct flow problem is certainly a great simplification, but it is still very useful to provide a first good insight into the most salient flow features like the propagation of the shock wave and the density discontinuity, and their reflections at the closed end of the duct, or the effect of these waves on the pulse jets at the individual exit holes. They are also useful to investigate the possible influence of the 90° bend of the duct upstream of the distribution section. Thus, the 2D simulations represent a computationally inexpensive first approach to investigate the basic structure of the transient flow field.

The extensions to the three-dimensional cases are not only carried out for a more comprehensive and realistic description of the real device, the three-dimensional results shall also unveil the scope and the limits of the two-dimensional considerations in predicting the real three-dimensional flow conditions.

After the computational examination of the flow field evolving in a distributor duct with the presently used end section, where the duct is simply cross-sectionally closed by a planar wall, the flow field obtained with a modified end section was investigated as well. In the analysis of the obtained results particular attention was paid to the impact of the modification on the reflection of the primary shock wave.

All simulated cases are summarized and briefly commented in Table 7.

Table 7: Performed simulations and brief description

Case		Description	Dimensions
P0	Straight planar duct	Generic test case with very simple geometry.	2D
P1	Planar duct with 90° bend	Analysis of the impact of the 90° bend on the propagation of the shock wave	2D
P2	Planar distributor duct with three exit holes (slots)	Analysis of pulse jet behaviour at the exit slots	2D
C1	Pipe with 90° bend	Provide three-dimensional results for a comparison against the two-dimensional simulations	3D
C2	Square distributor duct with three exit holes		3D
V1	Modified duct end section attached to the planar distributor section with three exit holes (Similar to P2)	Analysis of the influence of a modified end section on the reflected shock wave	2D

4.1. Results case P0

The planar duct was simulated as a generic test case to examine the capability of the presently used numerical setup to describe realistically the behaviour of the shock wave. A further benefit of the straight planar duct is the symmetry with respect to the horizontal plane along the channel axis. This allows for a reduction of the computational domain and thus saves computational time. The domain is sketched in the figure below. It extends into the axial direction 1m, and 31 mm into the vertical direction up to the plane of symmetry, which is equal to the half height of the real distributor duct.

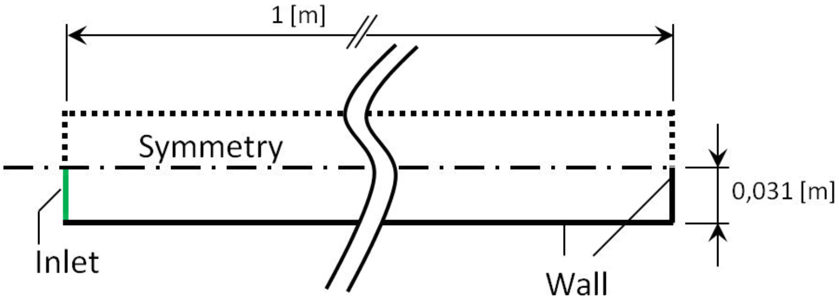

Figure 23: Geometry of the straight duct

The used computational mesh is visualized in Figure 24. The mesh was refined near the wall in order to resolve appropriately the wall boundary layer. The refined boundary layer is shown in white, the unrefined mesh in the core of the duct is displayed in yellow. The simple geometry of a square leads to no distortion of the cells, which implies a good mesh quality.

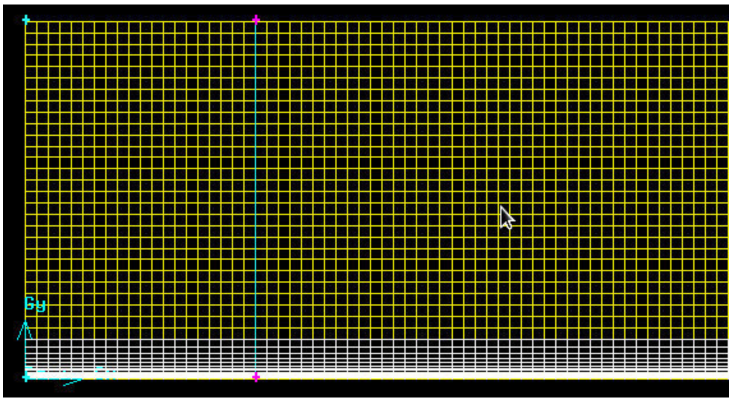

Figure 24: Mesh of the straight duct

As already stated in the previous chapter, the fluid inside the whole domain is initially at rest. It has uniform initial pressure and temperature, being equal to the ambient reference values. The mass flux according to Eq. (3.10) is imposed at the inlet, and a solid closed wall is assumed at the axial end of the duct.

The propagation of the shock wave

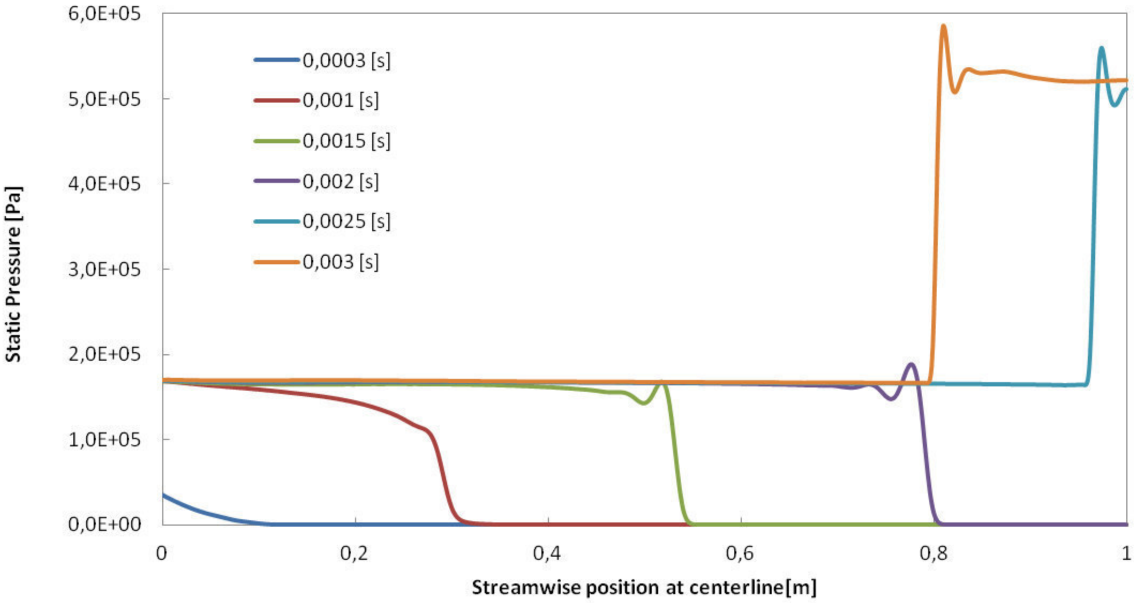

Figure 25: Streamwise variation of the pressure along the axis at different times

Figure 25 shows the axial variation of the static pressure along the centerline at different times. At the shown last two times the shock wave has already been reflected.

As it can be seen from early profiles, a certain time is required until a strong shock front has formed. The pressure behind the shock reaches a value of approximately 1.7 [Pa]. This pressure remains constant after the shock wave has passed the first time. The pressure is strongly increased after the passage of the reflected shock wave, as it can be seen in the profiles associated with the last two times. This significant second increase in pressure is due to the fact that the velocity drops to zero after the reflection, so that the dynamic pressure is transformed completely into static pressure. Figure 26 illustrates this neutralizing effect of the reflected shock wave on the velocity.

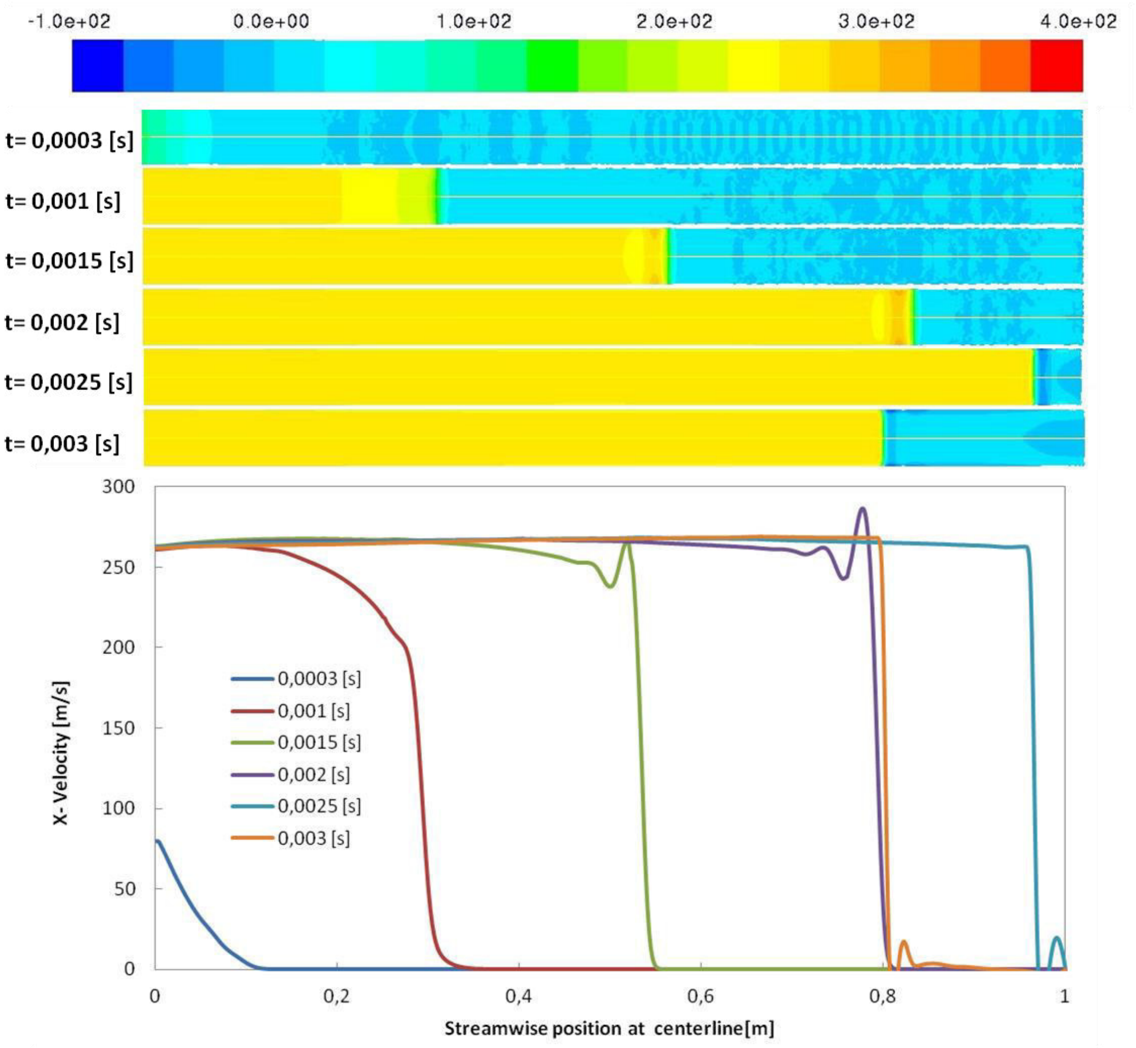

Figure 26: Contours and the variation of the streamwise velocity component along the centerline of the duct at different times

As seen from the contours of the velocity in the upper part of the figure, the velocity shows practically no variation into the vertical direction. This implies that the effect of the wall boundary layer is negligibly small, so that the motion can be practically regarded as inviscid. Thus, the results follow very closely to the inviscid streamtube theory, where the velocity behind the reflected shock becomes exactly zero.

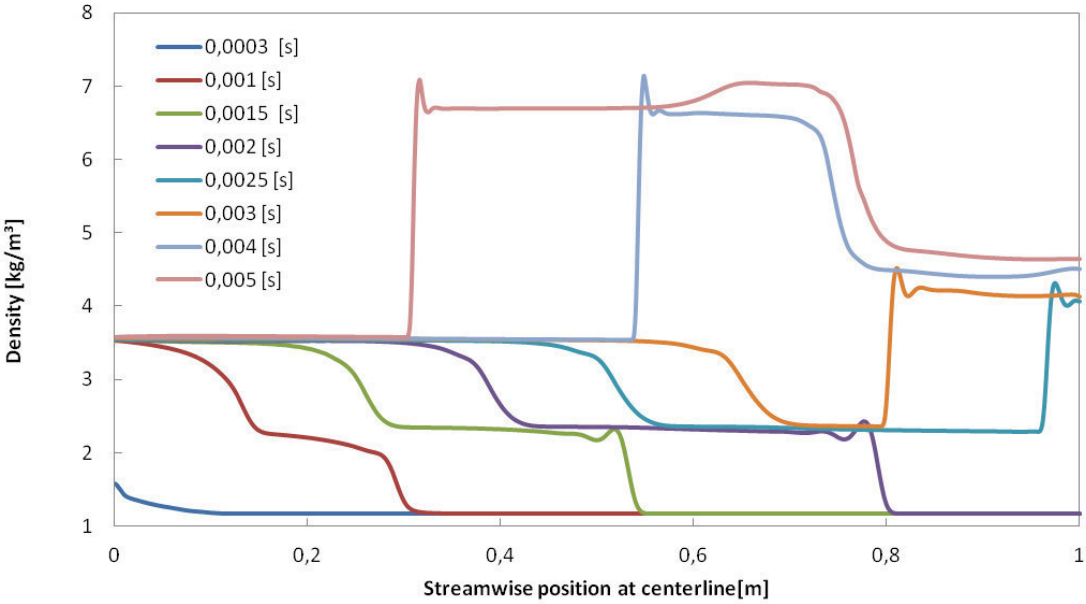

Figure 27: Variation of density along the centerline at different times

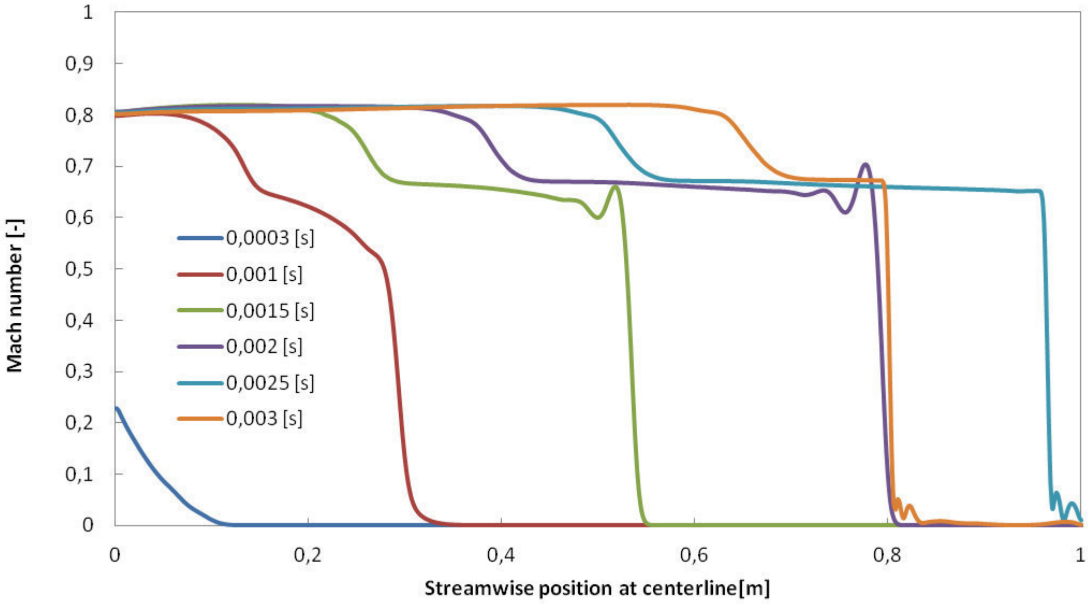

Figure 28: Variation of the Mach number along centerline at different times

Figure 27 shows the variation of the density along the centerline at different times. Two later times are included in this plot to demonstrate an important phenomenon occurring in this flow. The first four times shown in Figure 27 make apparent that the shock wave moves faster than the mass. This difference in speed causes two jumps in the density, the compression wave associated with the shock and the so called density-discontinuity behind the shock. As seen from the last shown times the collision of the reflected shock front with the density-discontinuity leads to a significant increase in density, and a temporally widening section with high density is formed. In Figure 28 the Mach number at different time steps is shown. It gets evident that the Mach number shows the same behaviour as the density. This results from the fact that the density-discontinuity translates directly into a temperature discontinuity, while the pressure and the velocity remain continuous. As a result of the local speed of sound increases so that the Mach number decreases at the discontinuity.

The presently obtained CFD results were also compared against data obtained from another one-dimensional simulation. In this one-dimensional simulation the one-dimensional inviscid conservation equations are numerically solved using a second-order Finite-Difference scheme for the discretization in space and a Mac Cormack´s scheme for the numerical integration in time The flux-corrected-transport (FCT) scheme proposed by Boris and Book [43] is used for the shock capturing. The whole numerical solution procedure was programmed in FORTRAN. Figures 29-31 show a comparison of the variations of the static pressure, streamwise velocity, and density along the centerline of the duct at different times. The results obtained from the inviscid one-dimensional solution are plotted in red, the results of the present CFD simulations with Ansys/Fluent are plotted in blue.

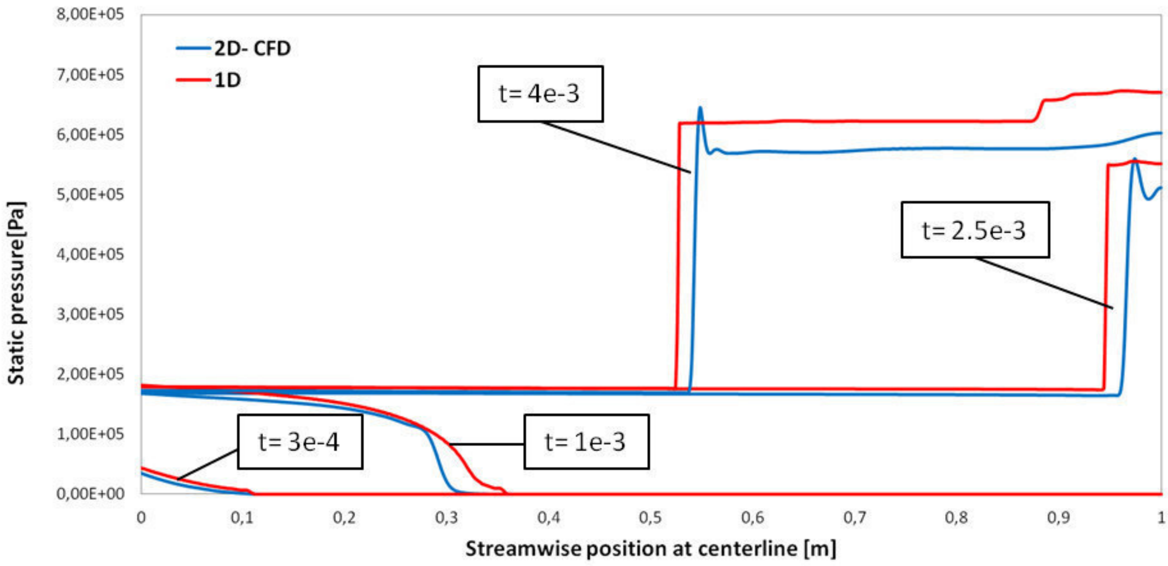

Figure 29: Comparison of the static pressure [Pa] of the 1D-simulation against the 2D CFD solution at different times [s]

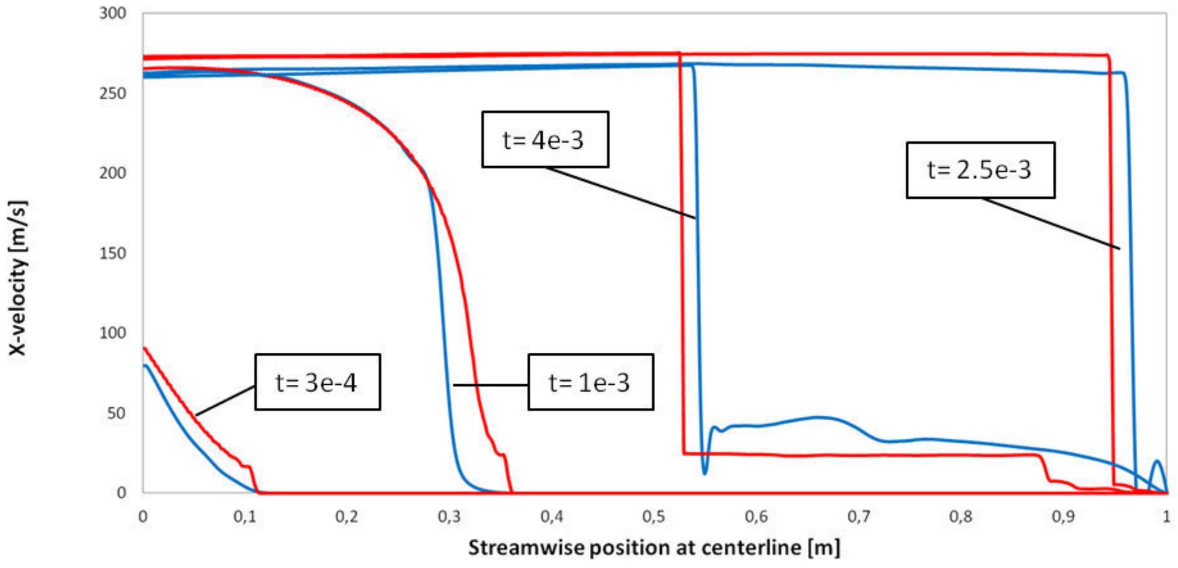

Figure 30: Comparison of the streamwise velocity [m/s] of the 1D-simulation against the 2D CFD solution at different times [s]

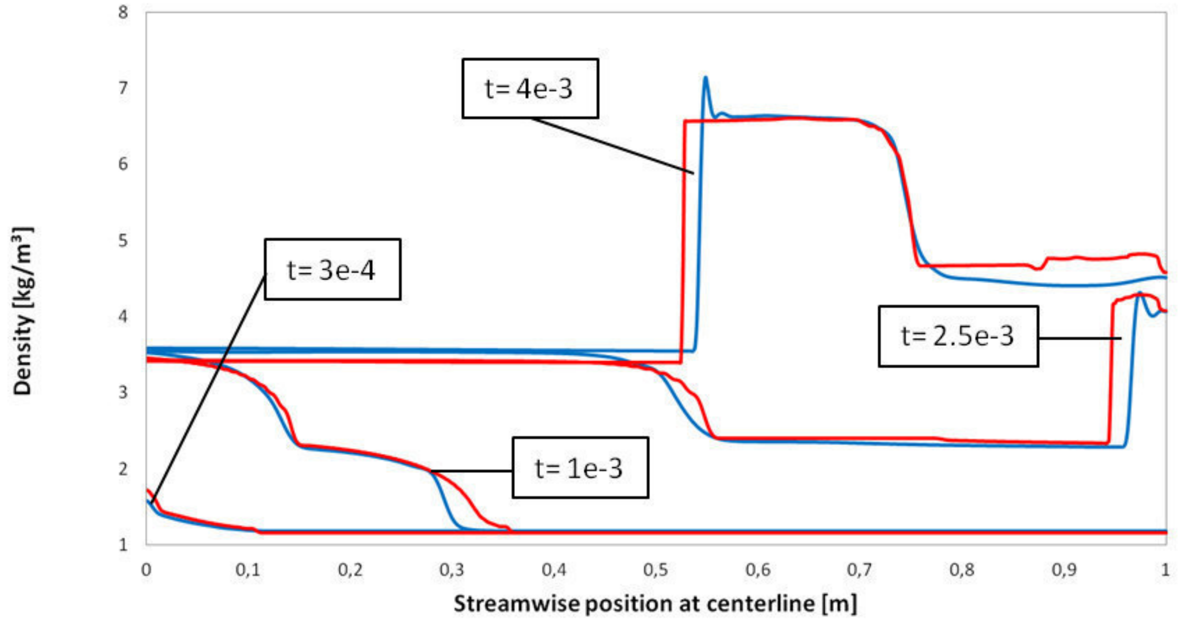

Figure 31: Comparison of the density [kg/m³] of the 1D-simulation against the 2D CFD solution at different times [s]

It can be seen that the results are roughly the same. The solution of the 1D simulation is always slightly ahead. This can be attributed to the fact that the 2D CFD solution includes wall friction, which has a small but still notable retarding effect. All in all, the propagation speed and the strength of the shock wave do not differ much, which indicates the very small influence of the viscous forces.

4.2.Results case P1

In a next step the influence of the 90° bend between the inlet and the distributor duct was analyzed. The effect of the bend on the propagation speed of the shock wave was of particular interest. This simulation was mainly motivated to answer, whether the 90° bend, occurring in the real application, can be neglected in the further computational investigations of the flow in the distributor duct.

Geometry

In this 2D-simulation the fluid first passes a straight section, a bit shorter than the straight planar duct considered in the previous case P0, where the shock wave can be formed. In the simulations of case P0 for the straight planar duct it became apparent that the shock wave has been fully developed after an axial length of 700 [mm]. The 90° bend follows the straight inlet section. A straight outlet section is attached downstream of the bend to allow for a streamwise decay of possible disturbances ahead of the end wall. The whole geometry is schematically shown in Figure 32. Here the black solid lines indicate solid walls, and the green line the inlet. At the inlet, the mass flux rate given by Eq. (3.10) is applied again.

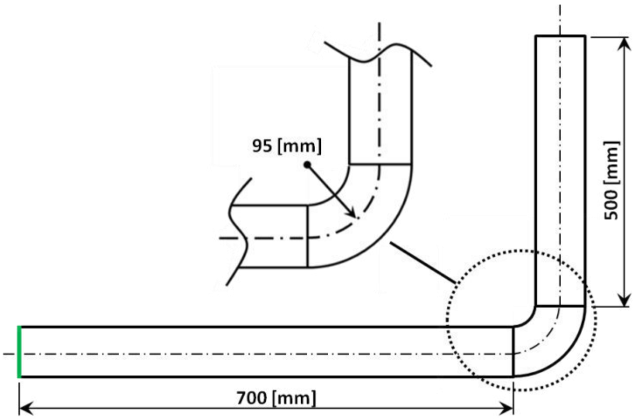

Figure 32: Sketch of the computational domain of the planar duct with a 90° bend

Simulation results

Figure 33 displays the contours of the static pressure at different times. At t=1.8e-3[s] the shock wave has just reached the entrance of the bend. When passing the 90° bend the initially planar shock front becomes distorted. It evidently moves faster on the radially inner side of the bend. However, the shock front recovers its unperturbed state very fast. An almost planar shock front is observed again already about three duct heights downstream of the bend. The local increase in shock speed on the radial inner side of the bend is also reflected by the magnitude of the velocities. The increased shock speed is accompanied by an increase in velocity up to a level even higher than the velocity of sound, as it can be seen in Figure 34. Summing up, the shown contours make apparent that the effect of the 90° bend on the conditions downstream is spatially very limited.

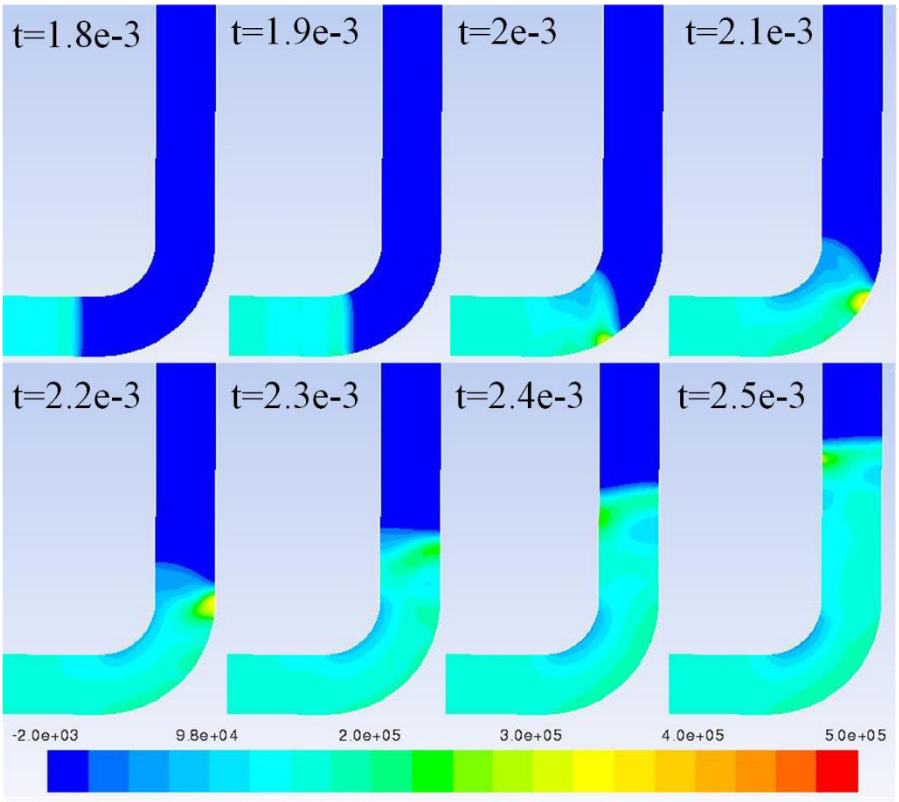

Figure 33: Contours of static Pressure [Pa] near the 90° bend at different times [s]

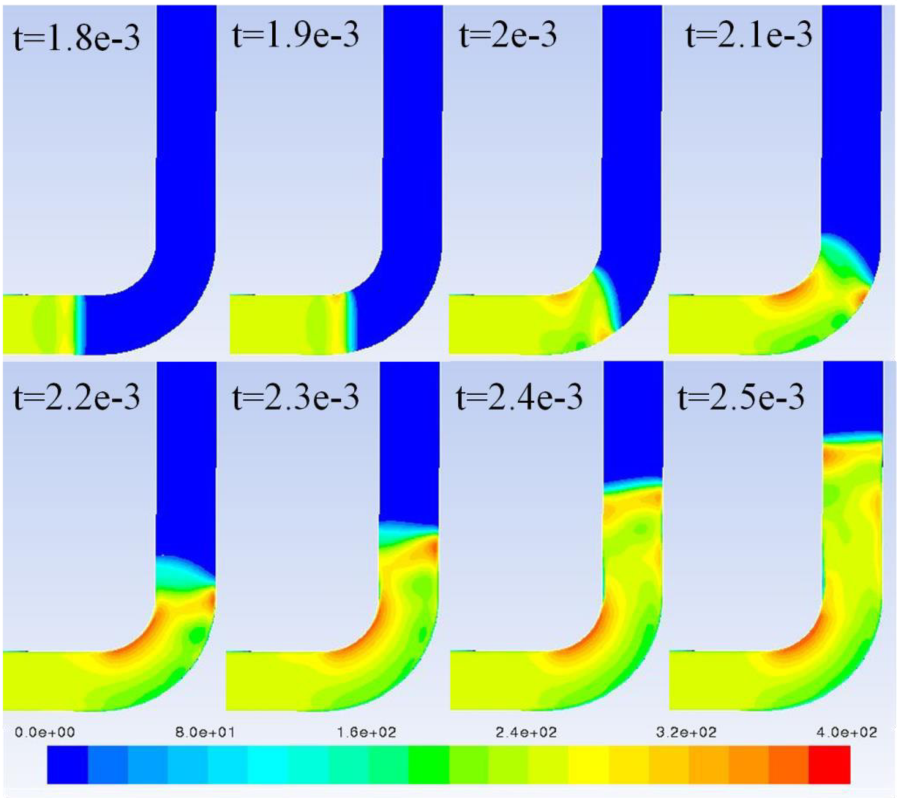

Figure 34: Contours of velocity magnitude [m/s] near the 90° bend at different times [s]

Additionally, the histories of the pressure and density were monitored at selected points in the flow field. This should provide a more quantitative insight into a possible influence of the 90° bend on the shock propagation further downstream. The positions of the selected points at the centreline of the duct are sketched in Figure 35.

The pressure and density histories shown in Figure 36 and 37, respectively, make evident that the effect of the bend on the flow is very small. Some more pronounced wiggles occur at the points downstream of the bend. Besides these temporal fluctuations the resulting compression of the gas upon passage of the shock remains almost the same.

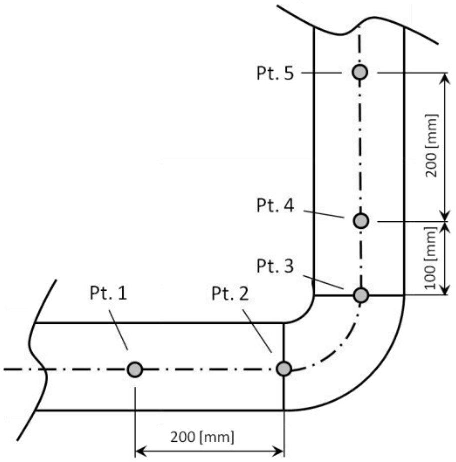

Figure 35: Positions of the selected monitoring points

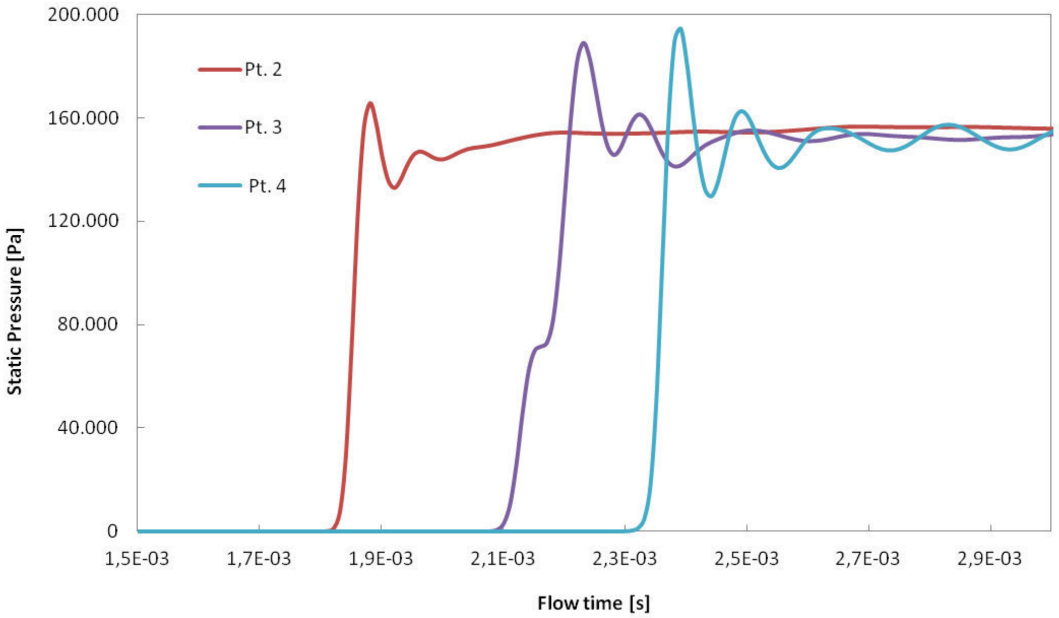

Figure 36: History of the static pressure at selected points in the duct

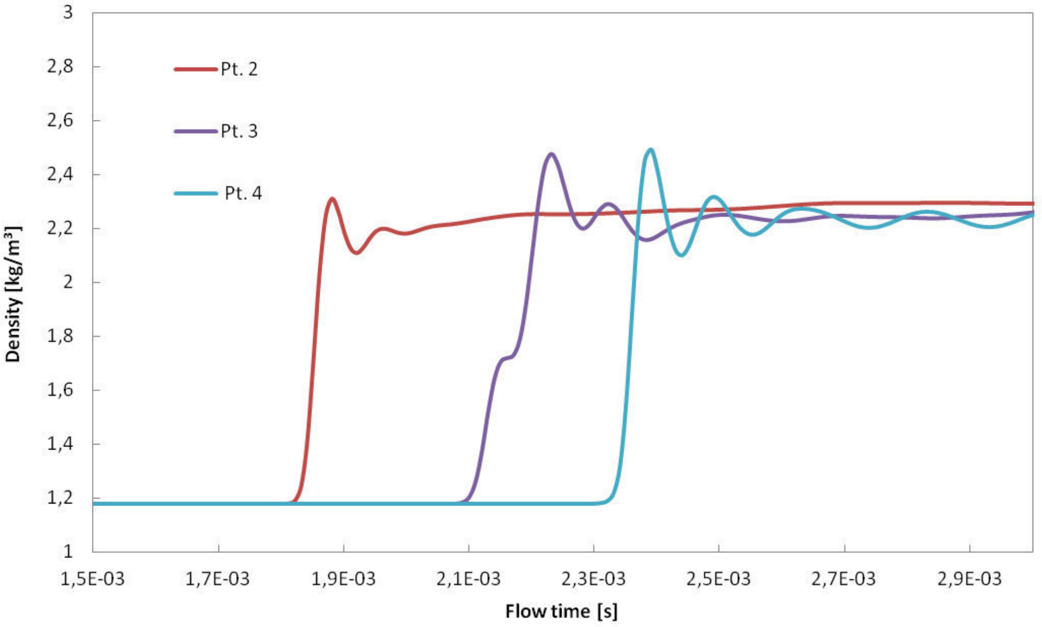

Figure 37: Density curve in different points in the pipe bend

Comparing the histories of the pressure at the equidistant pairs of points 1 and 2, and of the points 4 and 5 allows quantifying the influence of the 90° bend on the propagation speed of the shock wave. The time intervals which are required by the shock front when passing the equal distance between the considered pairs of points are indicated as Δt_1 and Δt_2 in Figure 38. Only a slight increase in shock speed can be observed. This suggests that the bend has only a negligibly small influence on the strength and the propagation speed of the shock wave. Based on these findings the 90° bend met in the real device was disregarded in all further two-dimensional simulations assuming a continuously straight duct from the inlet to the distributor section.

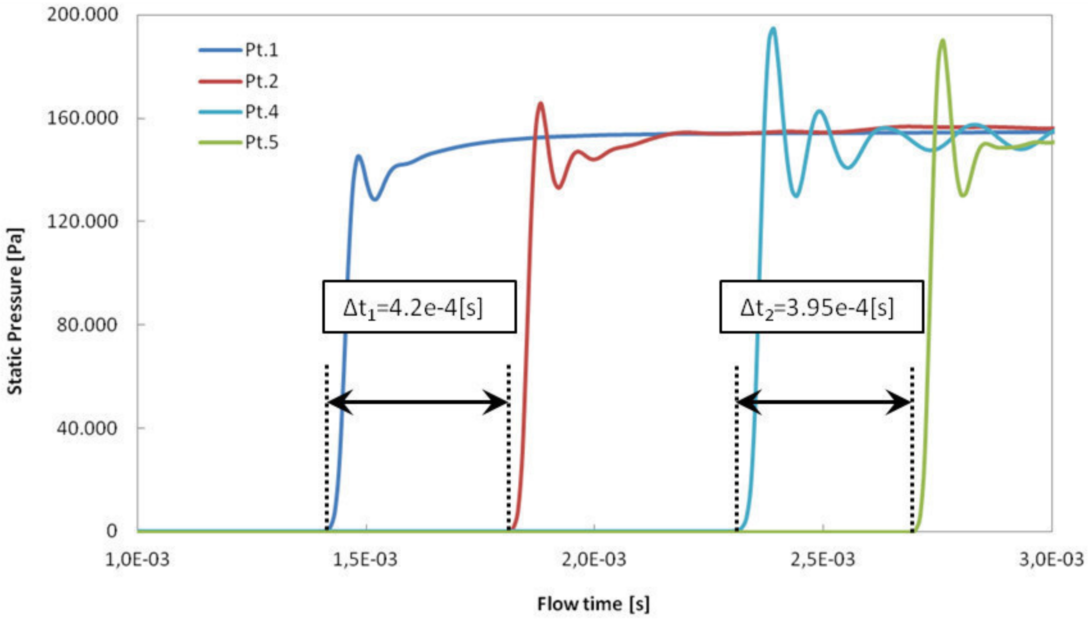

Figure 38: History of the static pressure for evaluation of the propagation speed of the shock wave in the 2D case

4.3.Results case P2

Case P2 extends the two-dimensional planar duct flow simulations to a strongly simplified manifold configuration with three exits at the lower wall of the distributor duct. Performing a 2D-simulation these exits are basically infinitely long slots. Despite the differences to the real three-dimensional application involving 16 cylindrical exit holes the results obtained for this case can already illustrate very well, how the propagating shock wave and its reflection at the closed end affect the pulse jets emerging from the individual exits. The geometry of the considered computational domain is sketched in Figure 39. Here the green line denotes again the mass flux inlet and the red lines the pressure outlet.

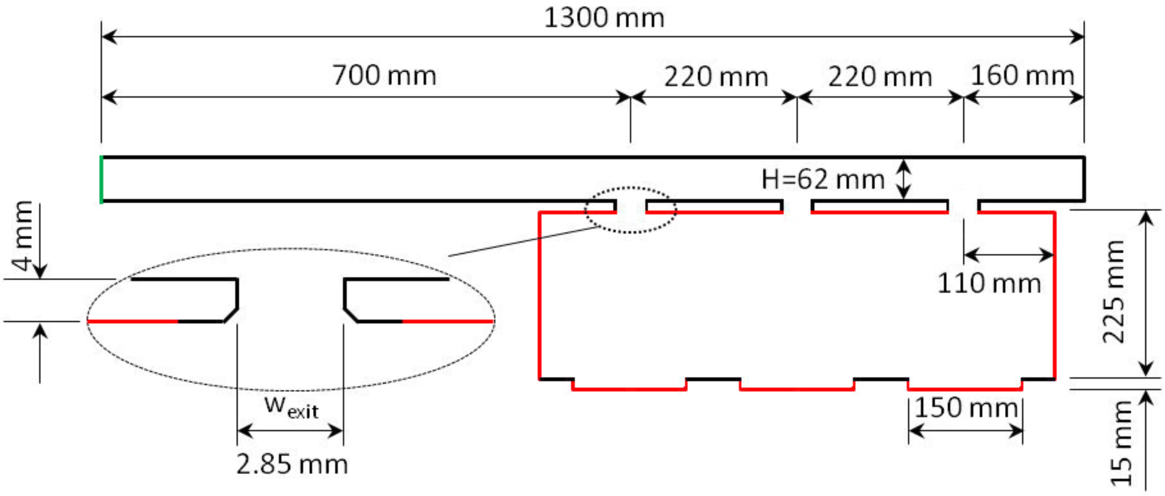

Figure 39: Computational domain with the mass flux inlet (green), the pressure outlet (red), and the solid wall boundaries

As seen from Figure 39, the computational domain is extended at the exits by an extra volume outside the duct. The extension is necessary to avoid instabilities, which would arise, if the pressure outlet boundary were imposed directly at the individual exits. The attached extra volume, wherein the pulse jets emerging from the exits are injected, is beneficial for the stability of the simulations, as it moves the pressure outlet boundary away from the region with very high velocities. At the bottom of this extra volume piecewise no-slip conditions are imposed to model the solid walls between the openings of the filter bags. Pressure outlet conditions are imposed on the upper side between the exit slots to avoid any unrealistic inference of the pulse jets. Using here solid wall boundary conditions would artificially limit the domain leading to strong recirculation zones, which do not occur in the real three-dimensional configuration. In order to guarantee a good comparability with the three-dimensional case, the width of the exit slots had to be chosen appropriately. The presently used setting is based on continuity considerations enforcing the same ratio of the exit cross-section relative to the cross section of the distributor duct for the 2D and the 3D case. Assuming B as unit spanwise extension of the planar duct in the 2D-case this equality reads

$$\frac{d^2\pi/4}{H^2} = \frac{w_{exit}B}{HB}, \qquad [4.1]$$

where H denotes the height of the square distributor duct, d the diameter of the exit holes in the real application, and w_{exit} the resulting width of the exit slots used in the 2D-simulations.

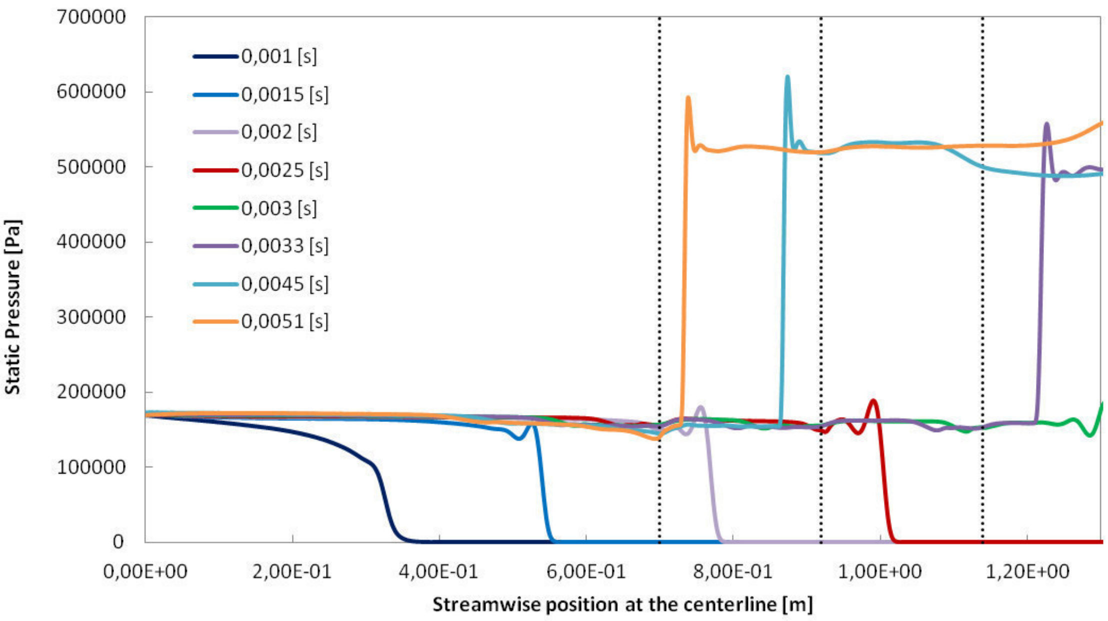

Figure 40: Variation of the static pressure along centerline for case P2 at different times

Figure 40 shows the variation of the static pressure along the centerline at different times. The positions of the exit slots are indicated by dotted lines. From this static pressure history plot it can be stated that the influence of the exit slots is negligibly small. There is actually no pressure drop occurring while the shock wave passes. Also the values for the static pressure before and after reflection are of the same order as those obtained from the straight planar duct without holes (P0). Looking more closely at the single curves before reflection, the pressure behind the shock exhibits some additional small variations in comparison to the straight planar duct. This may be due to the detachment of the flow occurring at the individual holes.

Figure 41 shows the centerline variations of the density at different times. It is immediately apparent that the behaviour of the density is similar to the previous results shown, featuring the first compression caused by the propagating shock and a contact discontinuity following behind. Again the drastic increase is well visible, when the discontinuity hits the reflected shock wave, as observed for the last two time steps. The effect of this drastic increase in density on the exiting pulse jets will be explained further below.

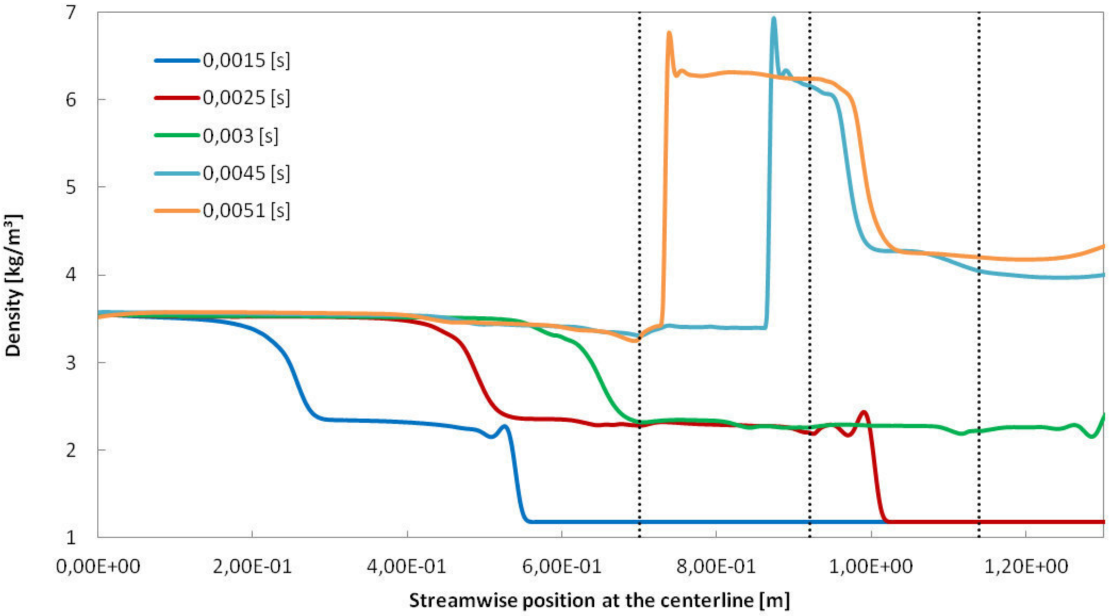

Figure 41: Variation of the density along the centerline for case P2 at different times

After the discussion of the shock wave propagating in the duct, the attention should be directed to the exiting behaviour of the gas. For this purpose the mass flow rate and the area-averaged velocity at the exit slots have been monitored. The corresponding evolutions in time are shown in Figure 42 and 43.

Figure 42 shows the mass flow rate through the individual exit slots. The first steep increase indicates the passage of the moving shock wave. The time intervals between these first step-like changes are approximately the same, which means that the passing shock wave does not speed up or slow down. A different behaviour can be observed when the shock wave is reflected. The increased time interval between the signals of the mass flow rate at the individual exits suggests that the shock wave is slowing down, as it encounters the contact discontinuity of the density. The diagram also makes evident that not only the first shock wave induces a strong pulse-jet, but even more intensively the reflected shock. Due to the reflection the pressure and density increase drastically which significantly increases the exit flow rates. The impact of the density discontinuity on the mass flow rate should not be overlooked here either. The collision of the reflected shock with the density discontinuity further increases the density leading to a substantially stronger increase of the mass flow rate exiting from the exits one and two, as compared to exit three, after the passage of the reflected shock. This might also explain, why the last bags are generally subject to higher mechanical stresses in the bag filter systems realized in existing devices.

Moreover, it can be seen that the mass flow rate through exit one roughly remains constant after the passage of the reflected shock and decreases afterwards. This decrease is due to the fact that, in the simulations, the valve is closed again after $t = t_{II} = 0.004\ [s]$, as indicated by the evolution of the prescribed inlet mass flux shown in Figure 22. The rapid decrease of the inlet mass imposed at $t > t_{II}$ triggers an expansion wave, which is propagated into the duct and finally collides with the reflected shock wave.

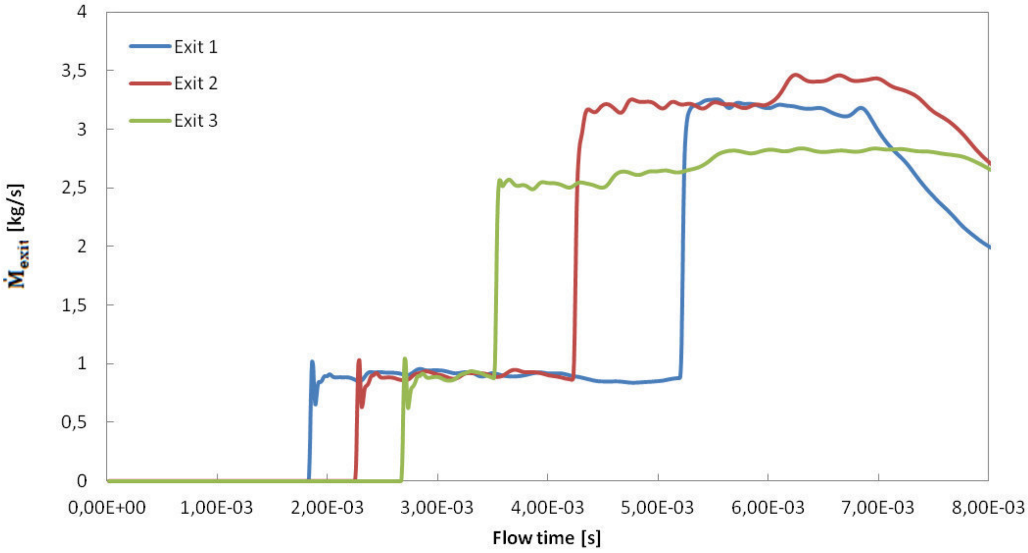

Figure 42: Mass flow rates ($\dot{M}_{exit}$) through the exits vs. time

Figure 43 shows the histories of the area-weighted average velocity magnitudes of the three exit streams. It becomes obvious that the velocities are the same for all exits when the primary shock wave has passed. After the reflection the third exit shows a higher velocity as compared to the other two exits. One reason for this behaviour is that the density discontinuity encounters the reflected shock wave before it reaches the third exit hole. The region with a strongly increased density resulting from the collision of the reflected shock with the density discontinuity does therefore not extend to the third exit hole, as seen in Figure 41. Thus, the density remains on a significantly lower level at the third hole, so that the exiting momentum translates into a higher exit velocity.

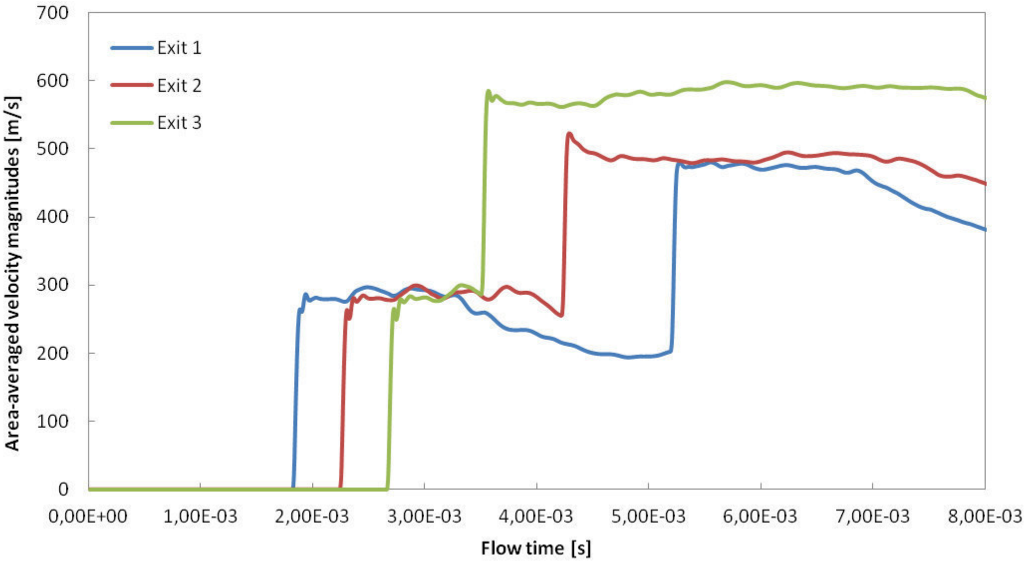

Figure 43: Area-averaged velocity magnitude at the individual exits vs. time

4.4.Results case C1

Case C1 investigates the flow inside the cylindrical pipe section between the pressure tank and the distributor duct. The focus of the three-dimensional simulation is on the effect of the 90° bend on the flow further downstream. The here considered configuration resembles fairly well the conditions of the air feed in the real advice. The geometry of the computational domain is shown in Figure 44. The axial and cross-stream extensions of the pipe were set to the same values as in the corresponding 2D-case P1 to allow for a comparison of the simulation results. Also the same initial conditions and boundary conditions were used.

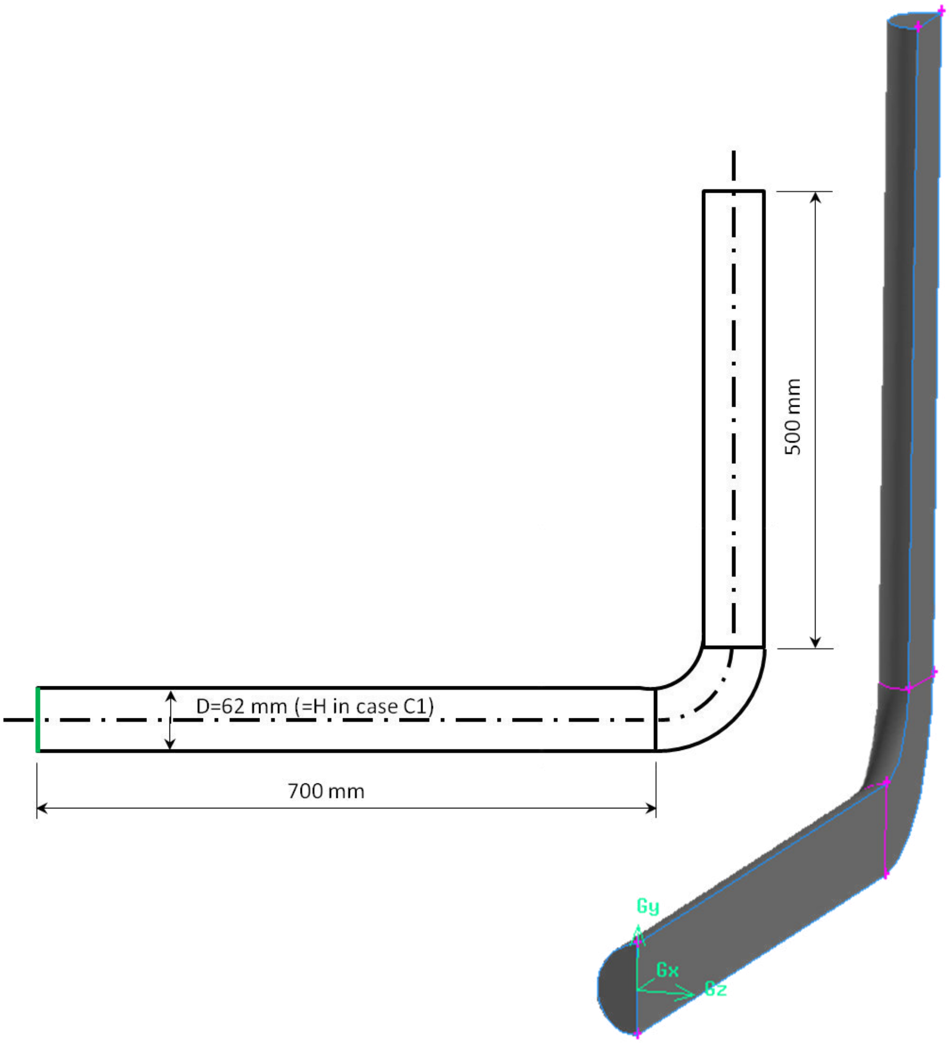

Figure 44: Sketch of the geometry of the three-dimensional pipe with a 90° Bend indicating the mass flux inlet (green line)

Figures 45 and 46 show the histories of the static pressure and density at the same points, as already considered in the corresponding two-dimensional case P1, respectively. It can be recognized that the shock wave behaves very similar to the two-dimensional problem. Here also some wiggles occur after the pipe bend at Pt. 3 and Pt. 4, and the shock induced compression leads to almost the same pressure and density levels as upstream of the bend observed at Pt. 2. As already shown for the two-dimensional case P1, the simulation of the three-dimensional case also indicates that the 90° bend no significant effect on the flow further downstream.

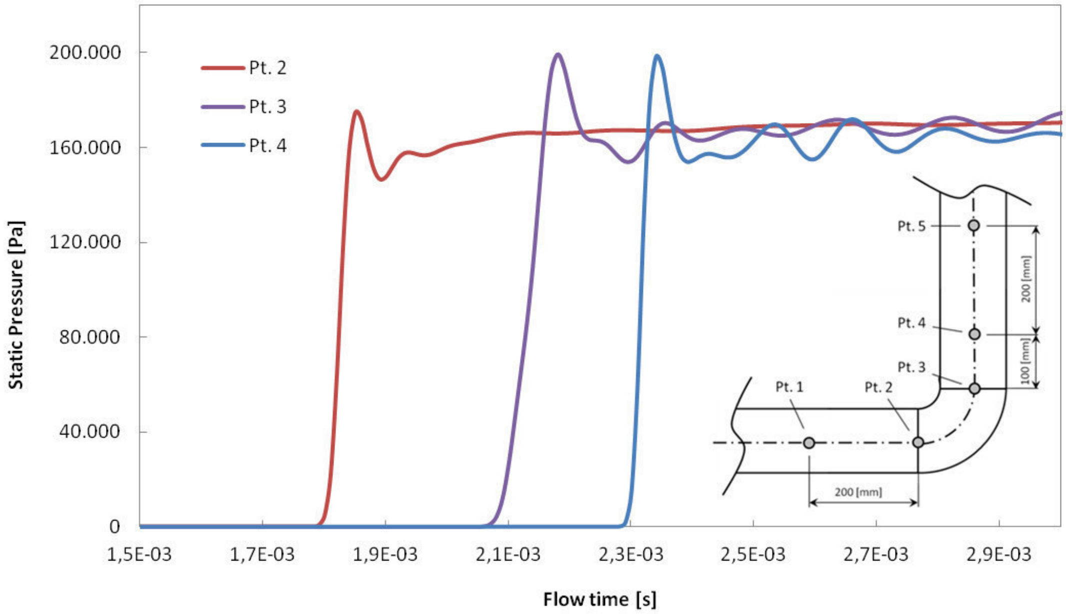

Figure 45: Histories of the static Pressure in the three-dimensional pipe with a 90° bend

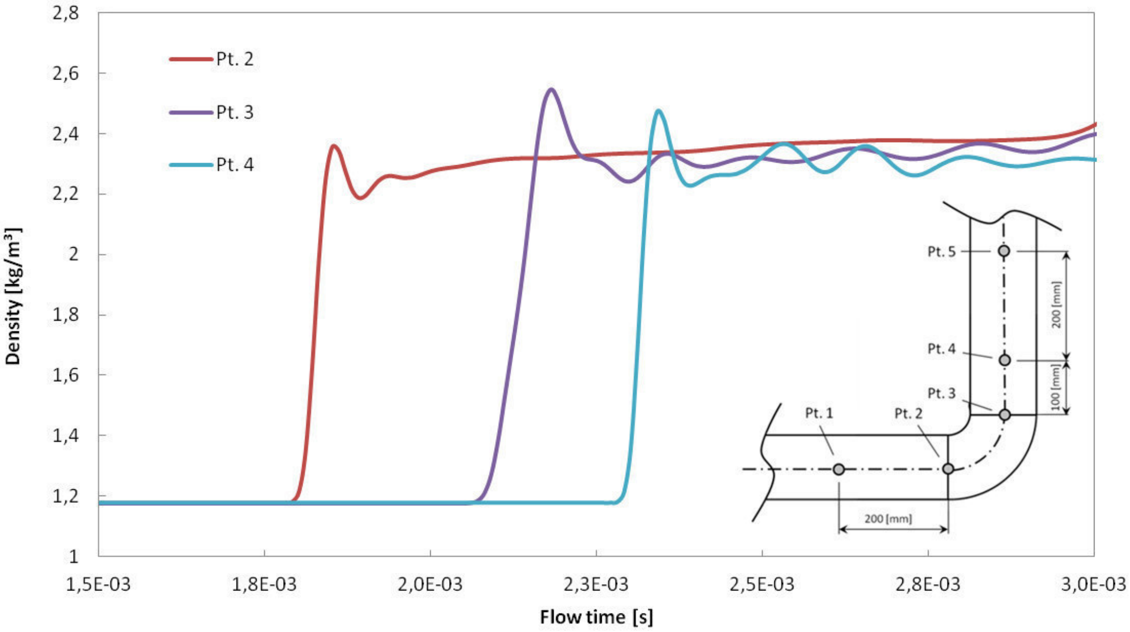

Figure 46: Histories of the density in the three-dimensional pipe with a 90° bend

The same holds true for the propagation speed of the shock, as seen from the time intervals between the two equidistant pairs of points displayed in Figure 47. The propagation speed is only slightly increased downstream of the bend. Similar to the two-dimensional case P1, it can be concluded also for the present three-dimensional case that the 90° bend occurring in the real application need not to be included into the simulation model. It appears to be sufficient to provide a certain straight inlet duct upstream of the distributor section, where the shock front can develop.

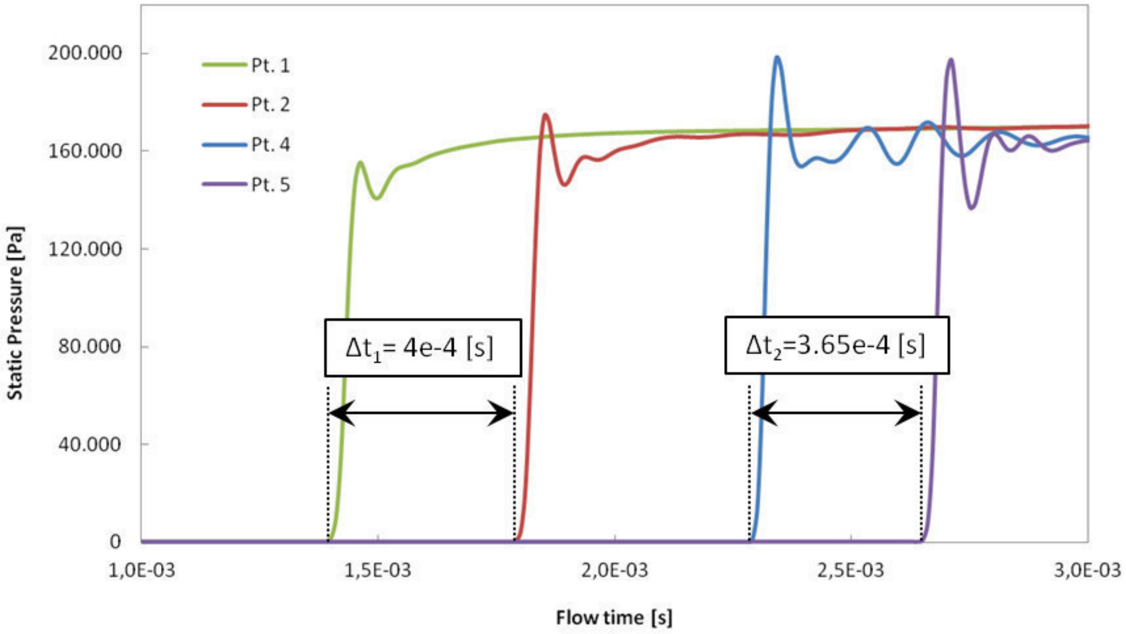

Figure 47: Histories of static pressure at two equidistant pairs of points for the evaluation of the propagation speed of the shock wave in the 3D case

Figures 48 and 49 show a comparison of the pressure and density histories obtained at a certain equivalent position (Point 4) for the two-dimensional case P1 and the present three-dimensional analogue. The shock reaches the considered positions evidently somewhat faster in the three-dimensional case, and the faster propagation speed expectedly leads to somewhat higher compression of the gas. The observed differences are still fairly small, so that it can be said that the computationally much cheaper two-dimensional planar duct simulation captures the real three-dimensional wall-bounded flow conditions very well.

Based on these findings the two-dimensional simulations provide a reliable and computationally efficient approach to optimize the geometry of the distributor section, wrt to the shape and position of the exits and the geometry of the end of the duct downstream. The effect of a special shape of the downstream end will be shown in the further discussion of the results for the case V.

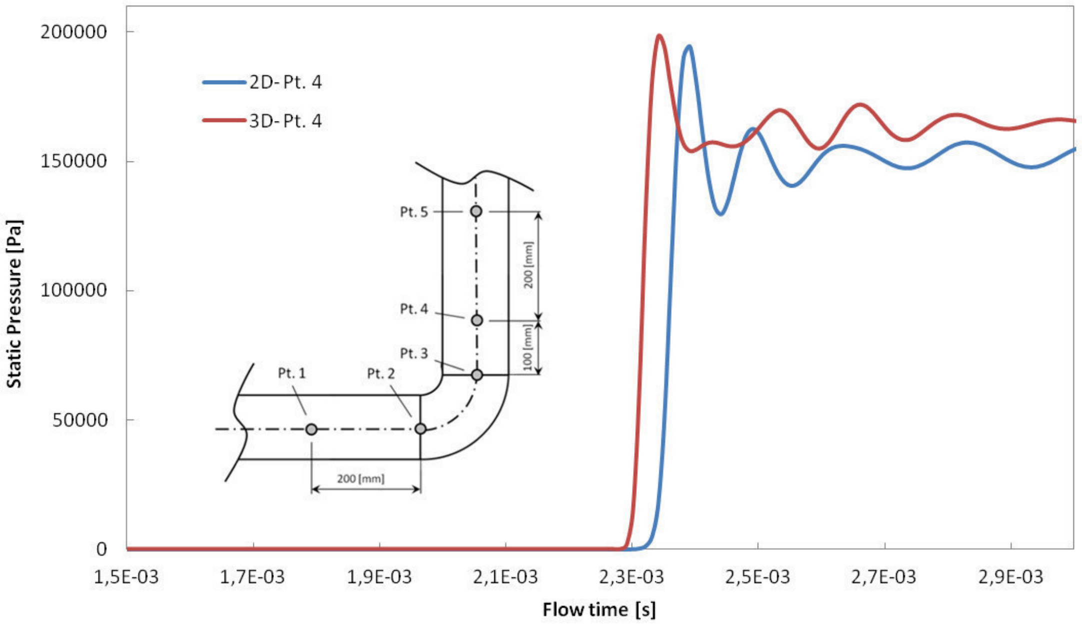

Figure 48: Pressure histories obtained at equivalent position (Point 4) for the 2D and 3D case

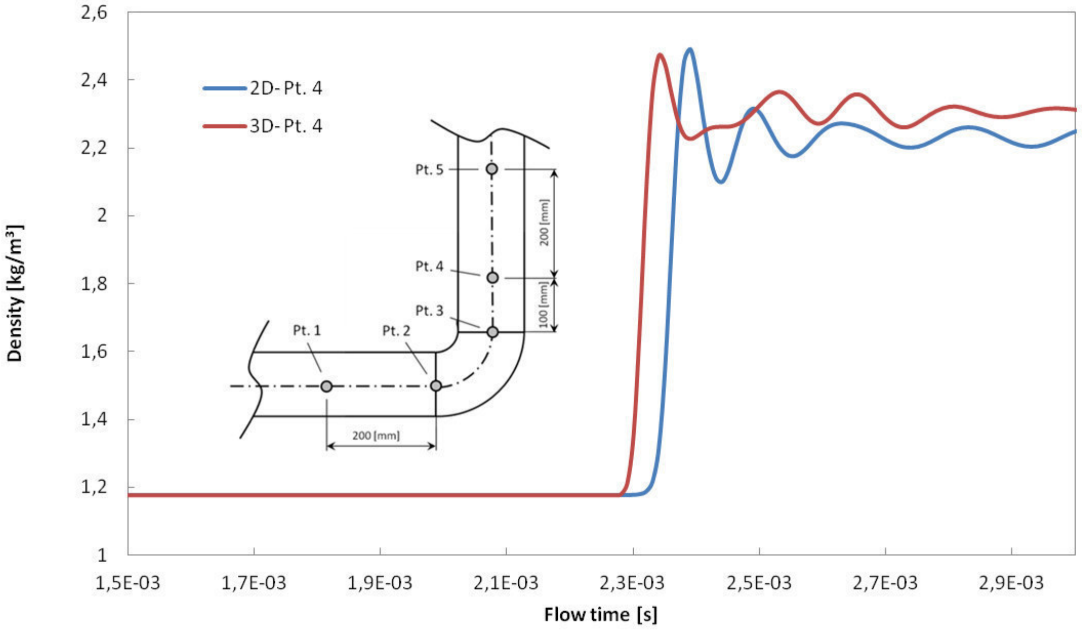

Figure 49: Density histories obtained at equivalent positions (Point 4) for the 2D and 3D case

4.5.Results case C2

Case C2 represents the three-dimensional analogue to the two-dimensional case P2 considering the flow inside the duct distributor manifold with three exits at the bottom. The exit cross-sections are circular with a diameter d_{exit}=15 mm as in the real application. The computational domain of the considered three-dimensional problem is visualized in Figure 50.

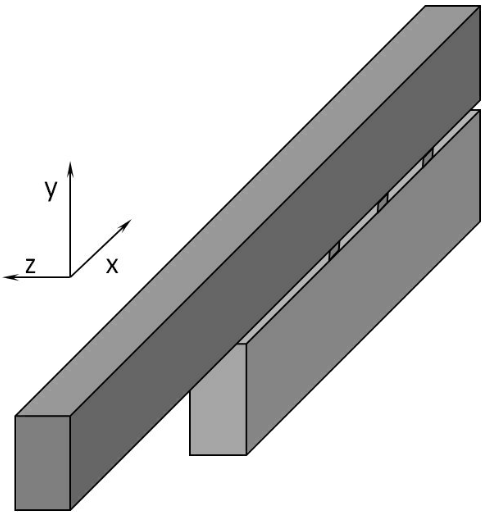

Figure 50: Geometry of the three-dimensional geometry with three exit holes

The spatial resolution of the mesh was approximately the same as for the two-dimensional analogue P2 for the sake of good comparability of the results. Solely the extra volume, into which the exit pulse jets emanate, has been vertically shortened in order to reduce the total size of the mesh, and hence the computational time. Due to the symmetry of the problem wrt to the meridional xy-plane at z=0, the computational model had to include only half of the volume of the duct, applying a symmetry boundary condition at the xy-plane at z=0. A more detailed view of the geometry showing the individual spatial dimensions is presented in Figure 51. Similar to the two-dimensional case P2, a mass flux inlet and pressure outlet conditions are imposed at the respective boundaries. As such condition the mass flux inlet condition follows from Eqs. (3.8)-(3.10).

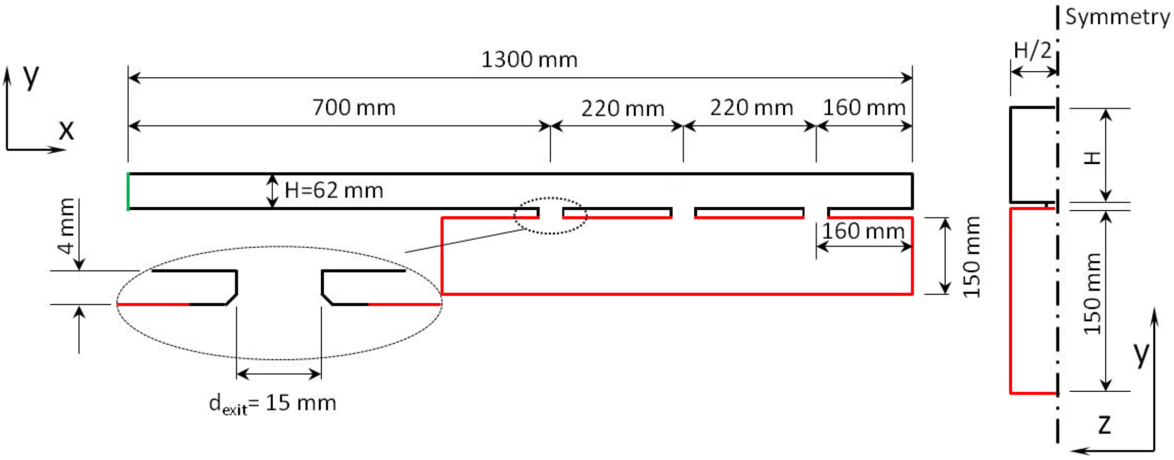

Figure 51: Dimensions of the three-dimensional geometry with the mass flux inlet (green), the pressure outlet (red) and the symmetry (dash-dot) boundaries

The main purpose of the simulation of the present case C2 was to provide three-dimensional data for a comparison against the corresponding two-dimensional data of case P2. This comparison should help to assess the capability of the computationally less expensive two-dimensional simulations to describe the three-dimensional flow conditions in the distributor duct, as they are met in the real application.

Figure 52 shows a comparison of the pressure variations along the centerline at the time t=0.003 [s]. At this instant of time both shock waves are near the end of the duct. It can be seen that the shock front of the two-dimensional case propagates a little faster in the two-dimensional case. Especially near the positions of the exit holes indicated by dashed vertical lines the three-dimensional solution exhibit stronger fluctuations. The flow exiting through the individual exit holes leads evidently to markedly stronger perturbations of the core flow inside the duct.

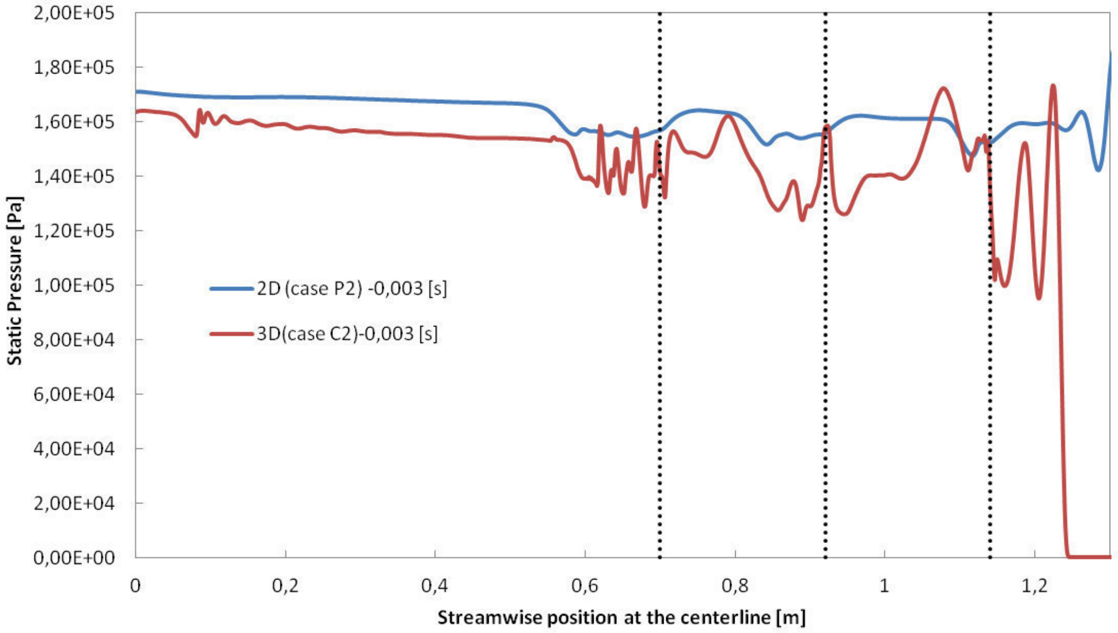

Figure 52: Comparison of the static pressure [Pa] along the centerline at t=0.003 [s]

Figure 53 shows the pressure variations at a later moment, where the shock wave has already been reflected. In the 3D simulation the reflected shock front moves somewhat faster and, accordingly, the compression of the air behind is stronger. Again the profile exhibits more fluctuations.

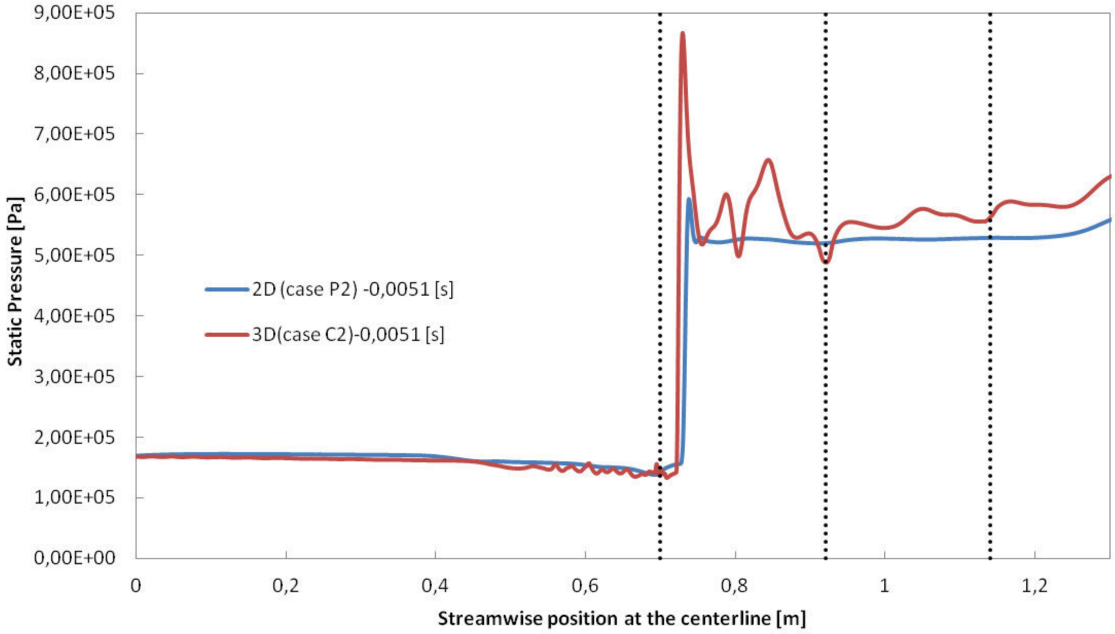

Figure 53: Comparison of the static pressure [Pa] along the centerline at t=0.0051 [s]

Figure 54 compares the variations of the density along the centerline at the times t=0.003 [s] and t=0.0051 [s]. The curves show essentially the same features as already observed for the pressure in Figures 52 and 53. The strong increase in density due to the collision of the density discontinuity with the reflected shock front is well visible for both cases, where again the three-dimensional solution exhibits significantly higher fluctuations.

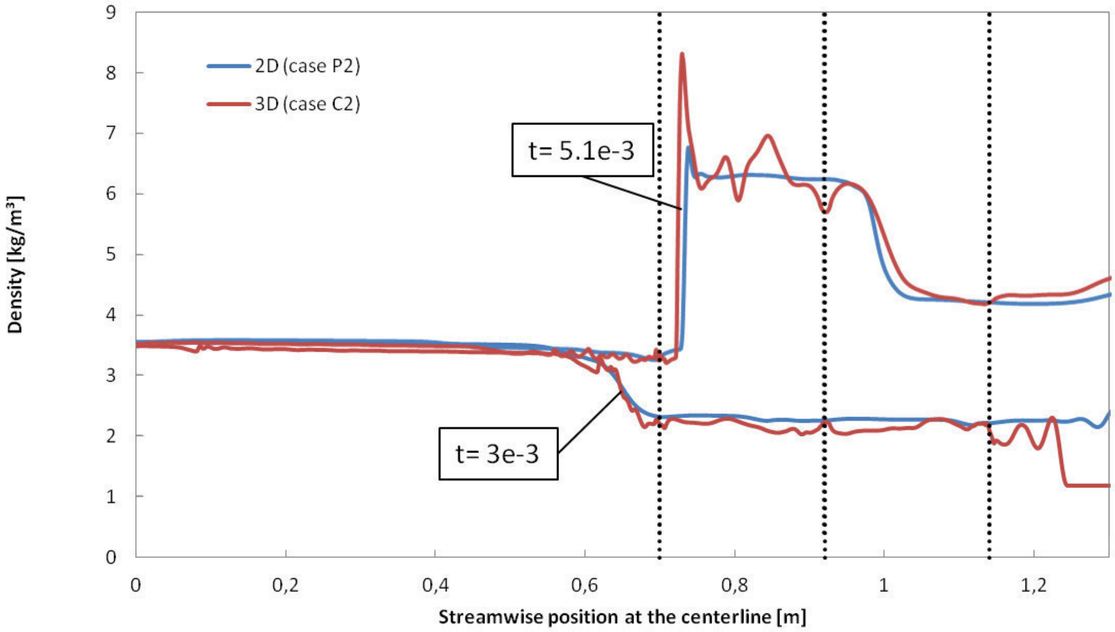

Figure 54: Comparison of the density [kg/m³] along the centerline at times t= 0.003 [s] and t=0.0051 [s]

Figure 55 shows the streamwise flow velocity at the times t=0.003 [s] and t=0.0051 [s]. Strong fluctuations appear again especially near the exit holes in the three-dimensional solutions. Aside from the wiggles the velocity shows roughly a behaviour very similar to the results obtained from the straight duct simulation P0. When the shock wave passes the first time, a flow velocity is instantaneously increased nearly to the speed of sound for both, the two- and three-dimensional case.

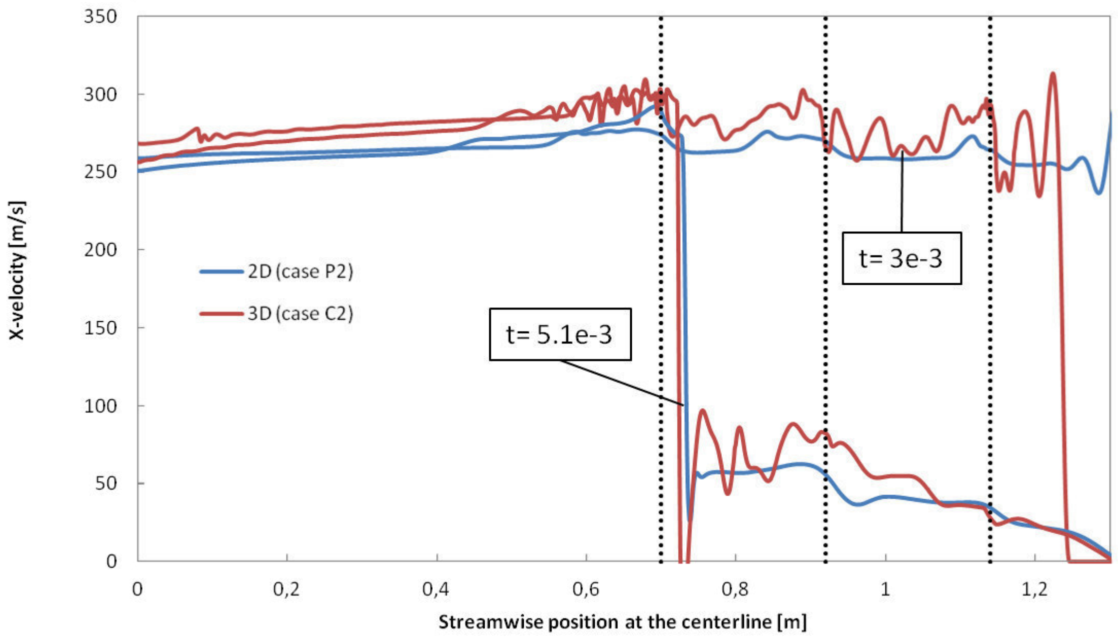

Figure 55: Comparison of the streamwise velocity component along the centerline at times t=0.003 [s] and t=0.0051 [s]

After the discussion of the results in the central core region of the duct the conditions obtained at the cylindrical exit holes shall be analysed. Figure 56 shows a comparison of the histories of the mass fluxes across the individual exit holes as predicted by the two-dimensional and three-dimensional simulations in case P2 and C2, respectively. As indicated by the dashed vertical lines in Figures 52 – 55 the axial position of the three exit holes are x=0.7 m, 0.92 m and 1.14 m, for the hole 1, hole 2, and hole 3, respectively. It gets immediately apparent that the behaviour of the mass fluxes does not differ much for both cases. Again, there are more fluctuations visible in the three-dimensional results. This can be directly attributed to the already discussed stronger fluctuating pressure and density inside the duct.

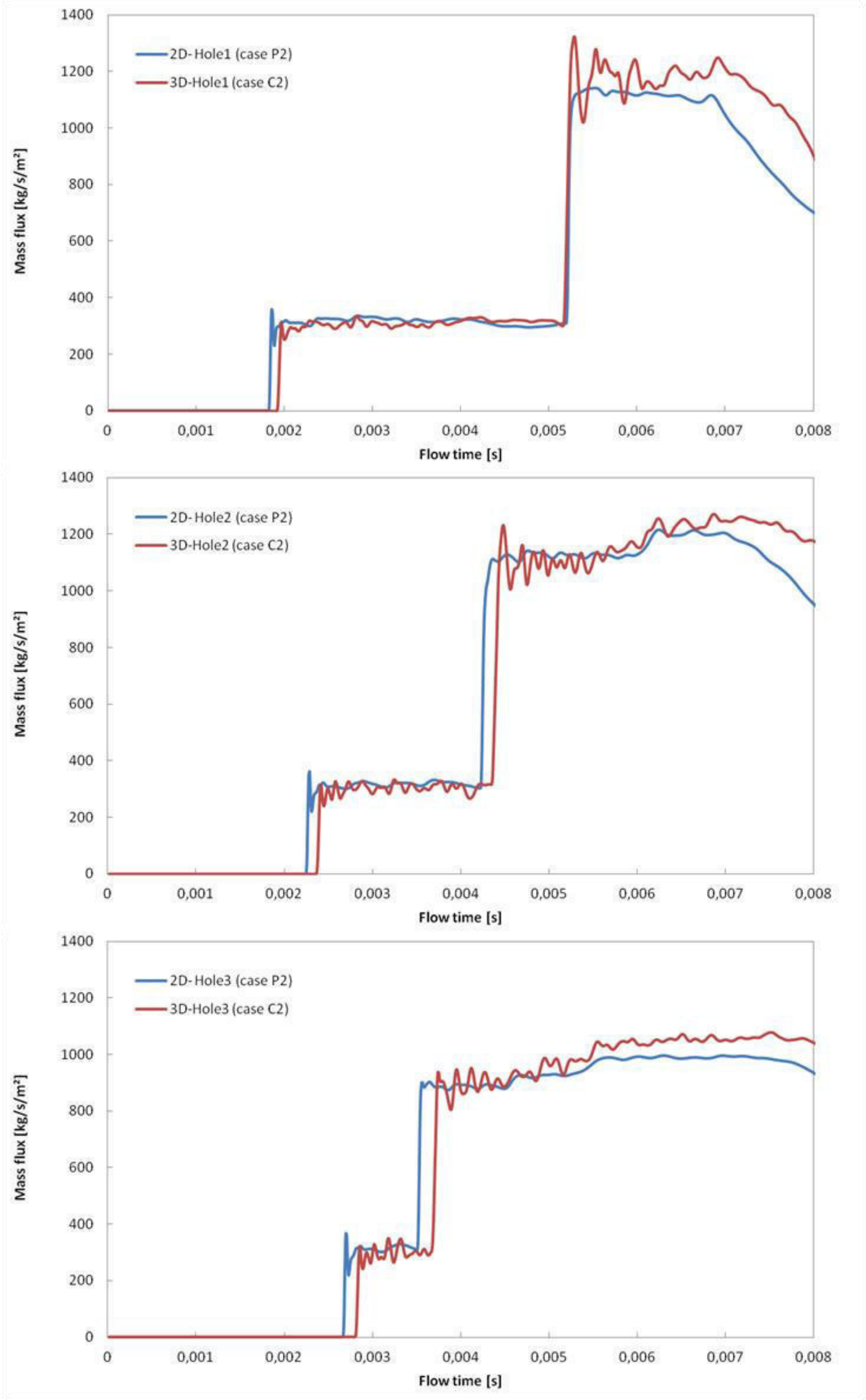

Figure 56: Comparison of the histories of the mass fluxes [kg/sm²] at the different exit holes

The instantaneous increase of the mass flux caused by the first passage of the shock wave occurs somewhat earlier for the two-dimensional case, which reflects the somewhat higher shock speed observed in this case. After the shock wave has passed the first time the mass fluxes through the individual holes remain constant. They increase even stronger once more when the reflected shock wave passes, as already has been described above when discussing the results for the two-dimensional case P2 in detail. Figure 57 shows the cross-sectional average density at the individual exit holes for both cases. It is obvious that the shown exit density is always considerably lower in the two-dimensional case than in the three-dimensional case. With this respect the solutions are evidently very different from results obtained at the centreline shown in Figure 54, where the densities of both solutions are essentially on the same level. The more pronounced decrease in density points at a stronger expansion of the gas at the exit holes in the two-dimensional planar case.

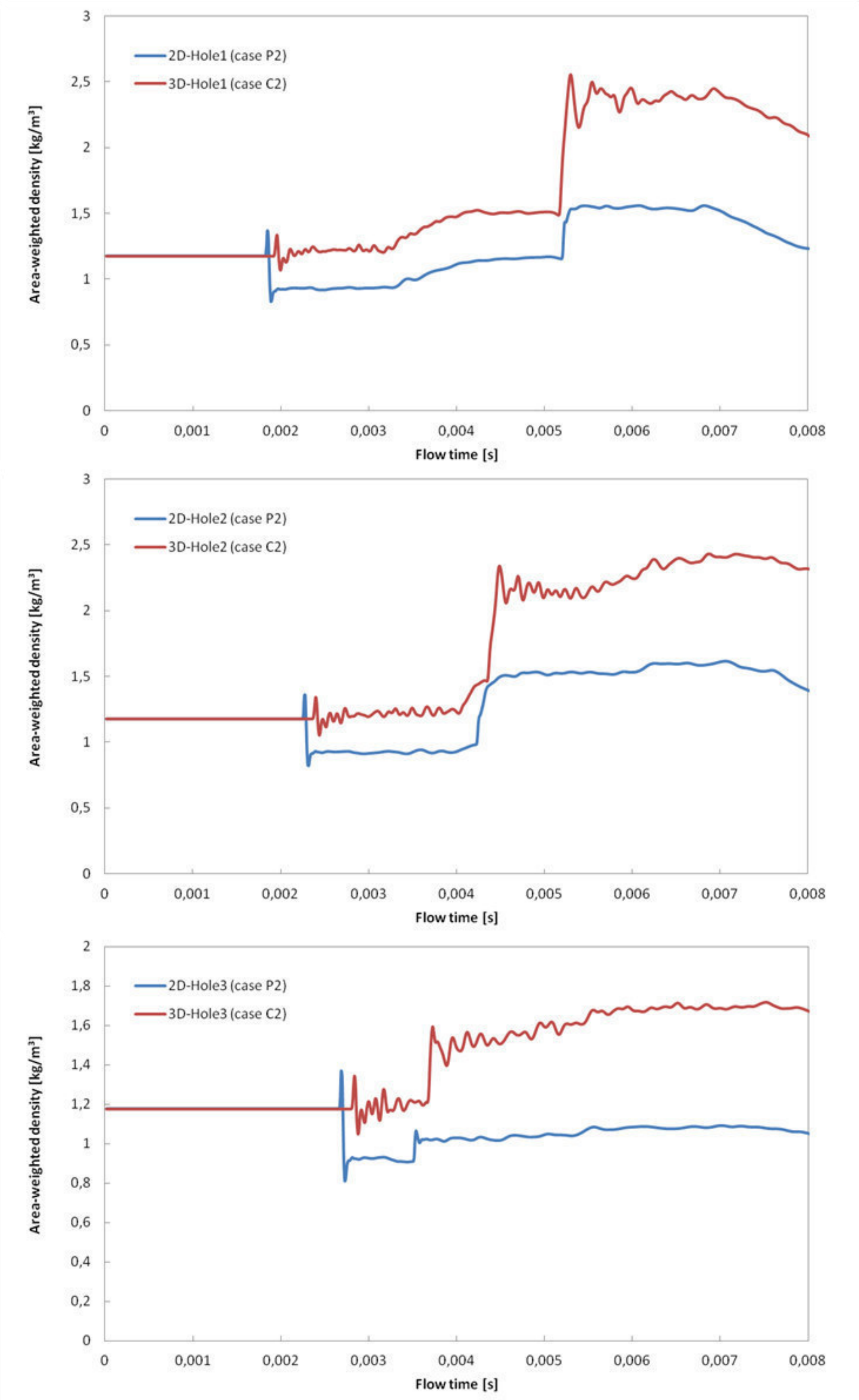

Figure 57: Comparison of the histories of the densities [kg/m³] at the different exit holes

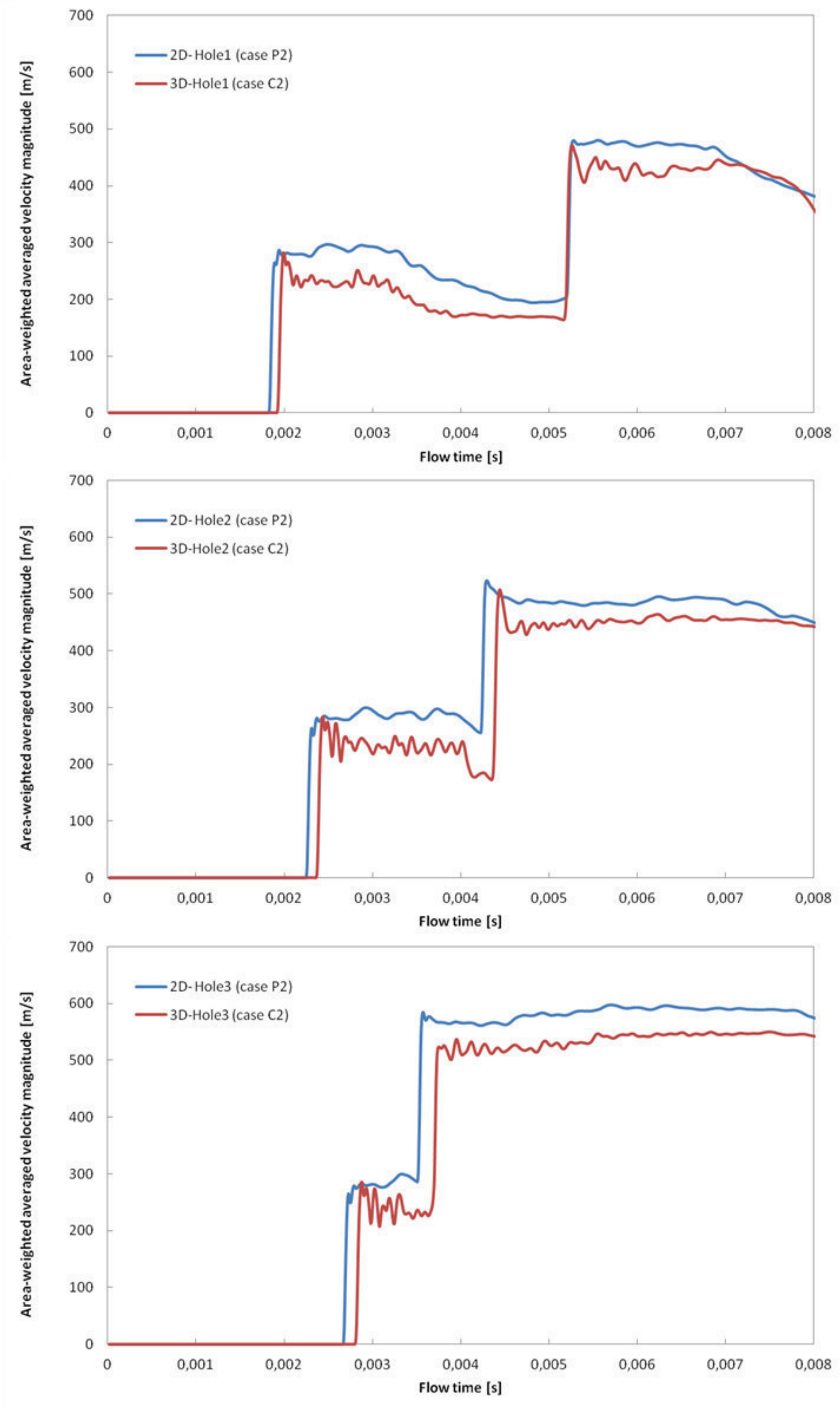

Figure 58: Comparison of the histories of the velocity magnitude [m/s] at the different exit holes

The histories of the cross-sectional average velocity magnitudes at the individual exit holes are depicted in Figure 58. It can be seen that the exit velocities of the two-dimensional solution in general considerably greater. This behaviour is directly related to the exit densities shown in Figure 57, as a smaller exit density combined with roughly the same exit mass flux seen in Figure 56 inherently gives a higher exit velocity. The difference in the discharge velocities has also some impact on the momentum of the pulse jets exiting the blow pipe. The exit momentum which is defined by Eq. (4.2) represents an important quantity for an efficient dedusting of the bag filters. Figure 59 shows the results of the 2D-case and the 3D-case. The shown momentum histories have been computed according to Eq. (4.2) using the value at the centerline of the duct for the pressure p, as the static pressure does not vary significantly over the cross-section of the duct.

$$I_{exit} = p + \dot{m}u \qquad [4.2]$$

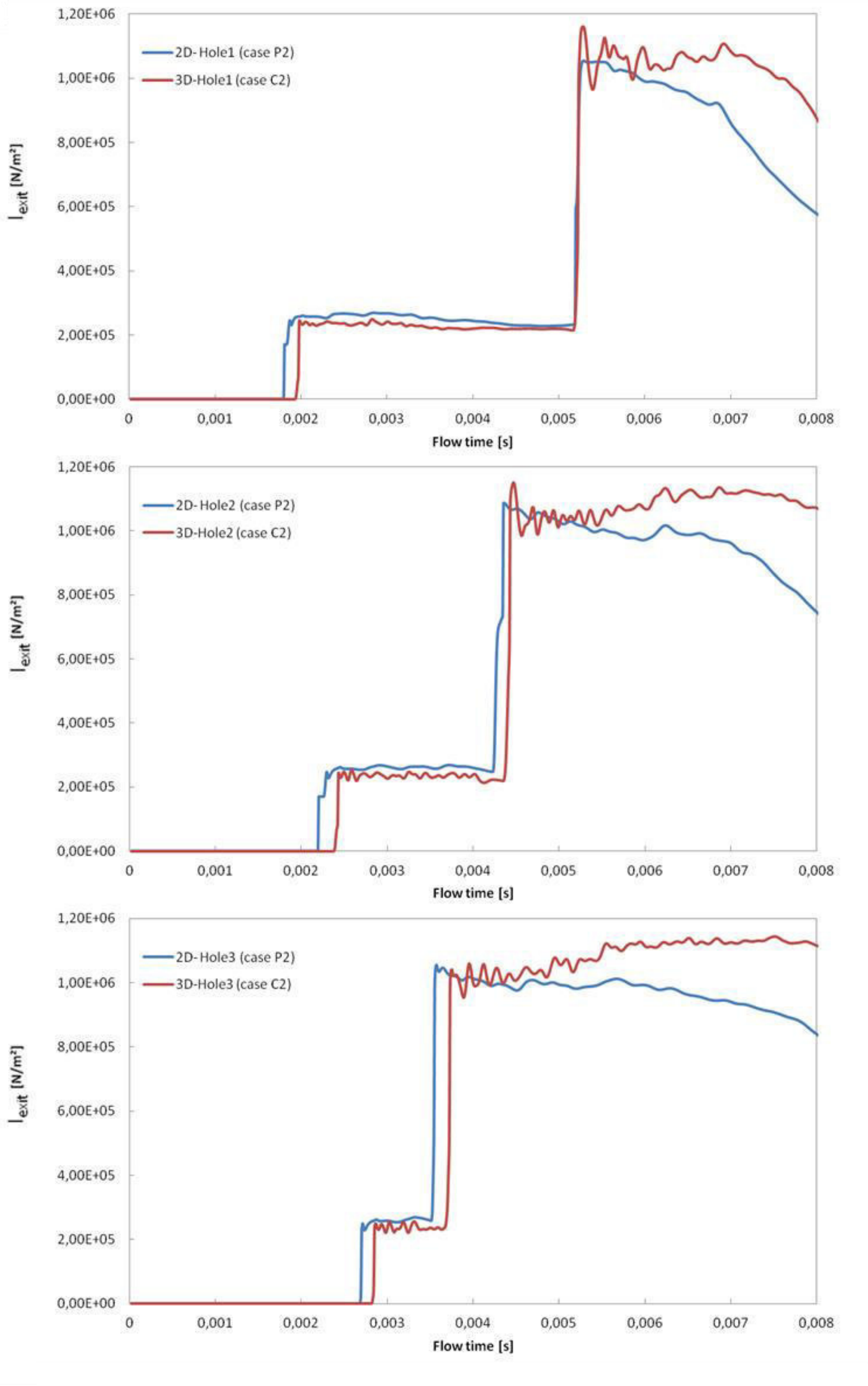

Figure 59: Comparison of the pulse jet momentum at the individual exits

Both cases show very similar histories of the exiting momentum. Only after the reflection of the shock wave at the rear end of the duct, the difference between the two cases becomes more significant. The impulse in the two-dimensional case drops earlier. This is especially evident at the first hole, where the static pressure inside the duct of the two-dimensional case drops faster than the pressure of the three-dimensional case.

Another problem, which may be highly relevant for the real application, may arise from the direction of the exiting air jets. A large deflection of the air jets could have a devastating impact on the lifetime of the bag filters. If the deflection angle is too large, the jets hit the outer surface of the bags and destroy them in the long run. The orientation of the exiting jets can be well visualized by the contours of the vertical velocity component as shown in Figure 60. Two distinct times are shown here, when the primary shock wave has already reached the rear end of the duct (t=0.0032 [s]), and after the reflected shock has passed all holes at t=0.006 [s]. It becomes obvious that the streamwise momentum which the gas catches up inside the duct, upon the passage of the primary shock wave, leads to a notable deflection of the exiting jets, which is about 15° from the vertical direction, as shown in the upper image. The reflected shock wave eliminates this streamwise momentum, so that the pulse jets are exiting vertically, as it can be seen in the lower image of Figure 60. As a result, the very strong pulse jets, which are induced by the reflected shock do not hit the outer surface of the bags, but almost enter them centrically.

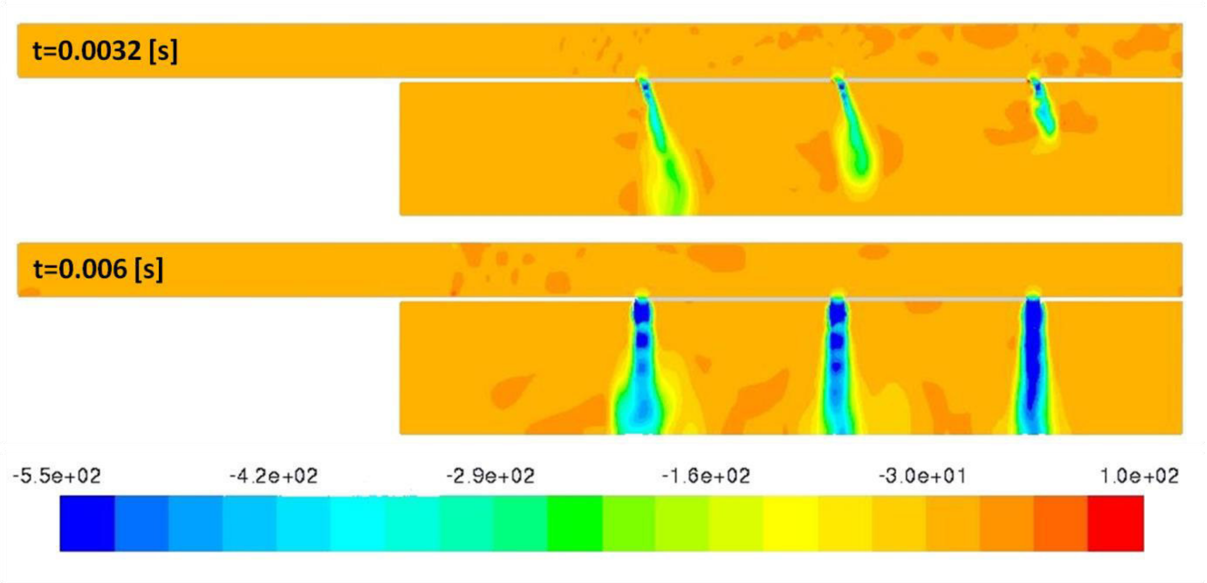

Figure 60: Contours of vertical velocity [m/s] to visualize the oblique angle of the air jets at t=0.0032 [s] (upper image) and t=0.006 [s] (lower image)

4.6.Results case V

The results shown for the cases P2 and C2 demonstrated that the reflected strong shock wave, especially after its collision with the density-discontinuity has a significant impact on the mass flux through the exits. In further consequence the dedusting of the individual bag filters may vary considerably.

As seen from Figure 59 the momentum of the exiting pulse jets rapidly increases to a very high level upon passage of the reflected shock. The obtained increase is stronger for the exits closer to the end of the duct. This peak in momentum of the pulse jets leads to the frequently reported stronger mechanical weir of the filter bags located close to the end of the duct. In order to reduce this extreme strain exerted on these bags a modification of the geometry of the duct is presented and computationally analyzed as case V in the following.

The basic idea of the considered modification is to reduce the peak in the exiting momentum, which is generated by the reflected shock wave by attaching a certain widening volume to the end of the duct. In the problems considered thus far the shock wave always perpendicularly hits a planar wall and is therefore reflected in the full strength. This strong reflection should be weakened by applying a small volume at the duct´s end, where the shock wave can expand into and is reflected at different points into different directions. Dependent of the shape of the attached volume it is for instance possible that two oblique shock waves are reflected being both weaker than a single normally reflected shock. This shall be presently achieved by a volume with a geometry visualized in Figure 62. In this special case the shock wave is reflected at different points and with different intensity. The geometry of the full computational domain is displayed in Figure 61. It is essentially the same geometry as in case C2 now extended by the additional expansion volume at the end of the distributor duct.

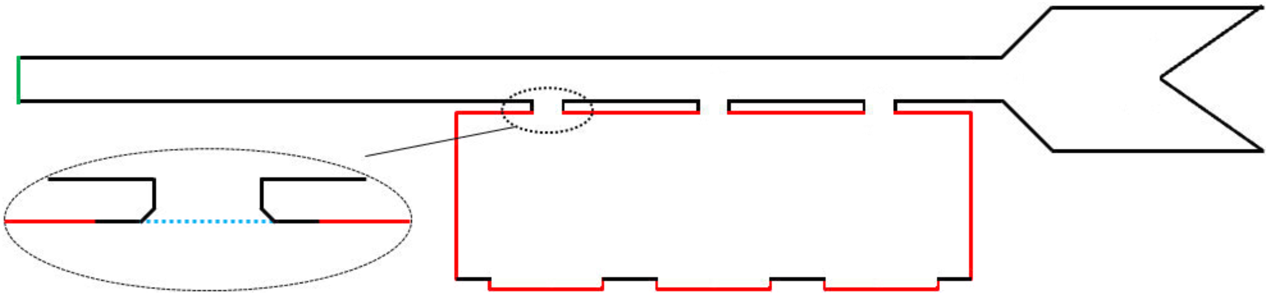

Figure 61: Sketch of the full geometry of the planar duct with the modified end (case V)

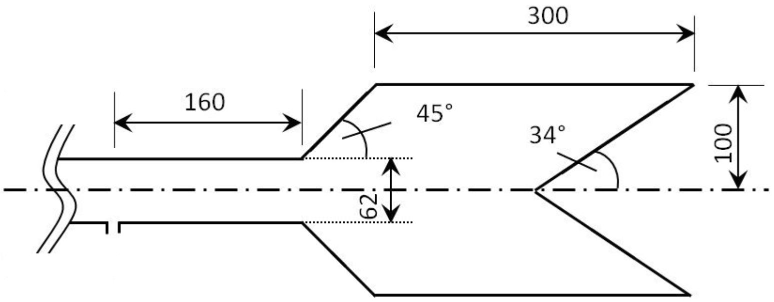

Figure 62: Detailed view of the modified and of the duct

The two-dimensional simulations for case V used the same boundary conditions as prescribed in the case P2 for the distributor duct with the unmodified downstream end. Figure 63 shows the variations of the static pressure along the centerline at different times as obtained for the cases with and without the modified end of the duct. The times were selected in a way that the primary heading shock waves are approximately at the same positions.

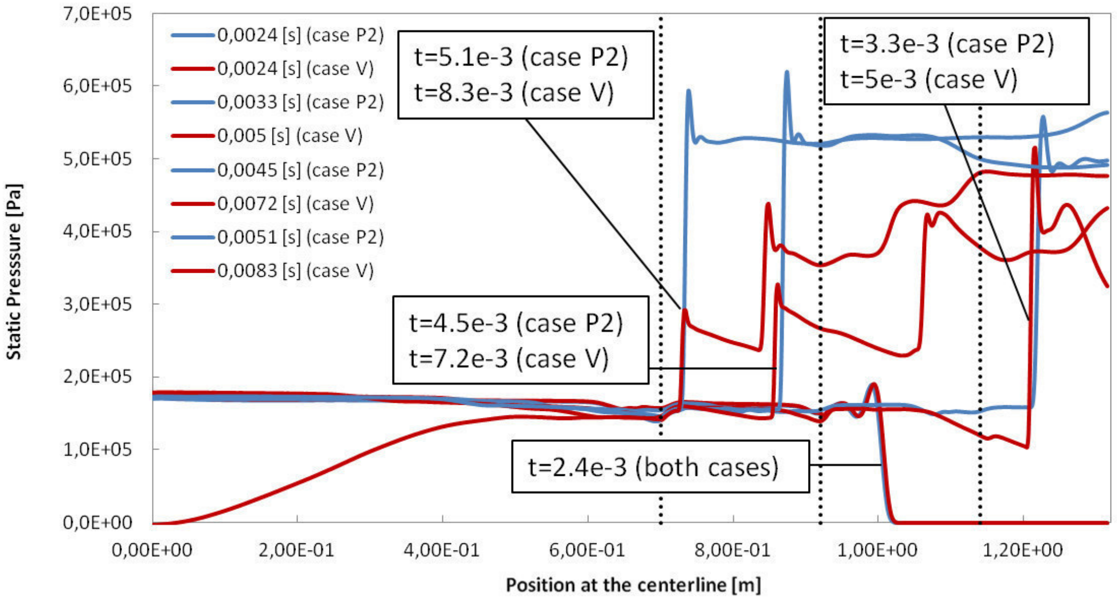

Figure 63: Variations of the static pressure [Pa] along the centerline of the duct at different times

The initial formation of the shock wave is equal to the results obtained for all the straight two-dimensional cases, as indicated by the time step t=0.0024 [s]. The behaviour of the pressure inside the attached tank is very complex and is not shown here in detail. It should be mentioned that it takes about 1.7e-3 [s] the heading reflected shock wave enters the duct. It can be seen that the heading reflected shock wave is considerably weaker as compared to the unmodified case P2. The first reflected head wave is followed by a second stronger reflected shock wave. These second reflection shock would trigger a further pulse jet for dedusting, which is however still much weaker than the pulse jet induced by the reflected shock in the unmodified original duct case P2. Comparing the elapsed time which it takes until the reflected head waves reach equivalent positions, it becomes obvious that the heading shock wave of the modified case V is propagated slowlier.

Another important effect on the flow field and on the dedusting is due to the density discontinuity, as visualized in Figure 64. The longer residence time of the shock wave in the extra volume permits that the density discontinuity can propagate farther into the duct. As a result, it collides with the reflected shock after having already passed the exit hole 3, as seen from the profile at t=5e-3 [s] for case V in Figure 64. The later collision of the density discontinuity not with one single strong reflected shock but with a couple of weaker diffracted shock waves leads to a step-wise more gradual increase in the density as compared to the one single very strong increase observed for the unmodified case. This has the consequence that it takes a certain span of time until the density finally reaches a similarly high level as in the case with the unmodified duct end. The first sharp increase in density caused by the collision of the contact surface with the reflected shock wave is thereby significantly attenuated due to the attached volume. The delayed and more spread in time increase in density has a significant impact on the blow out characteristics at the individual holes. This will be shown in more detail below in the discussion of the histories of mass flow through the individual exit holes, as depicted in Figure 66.

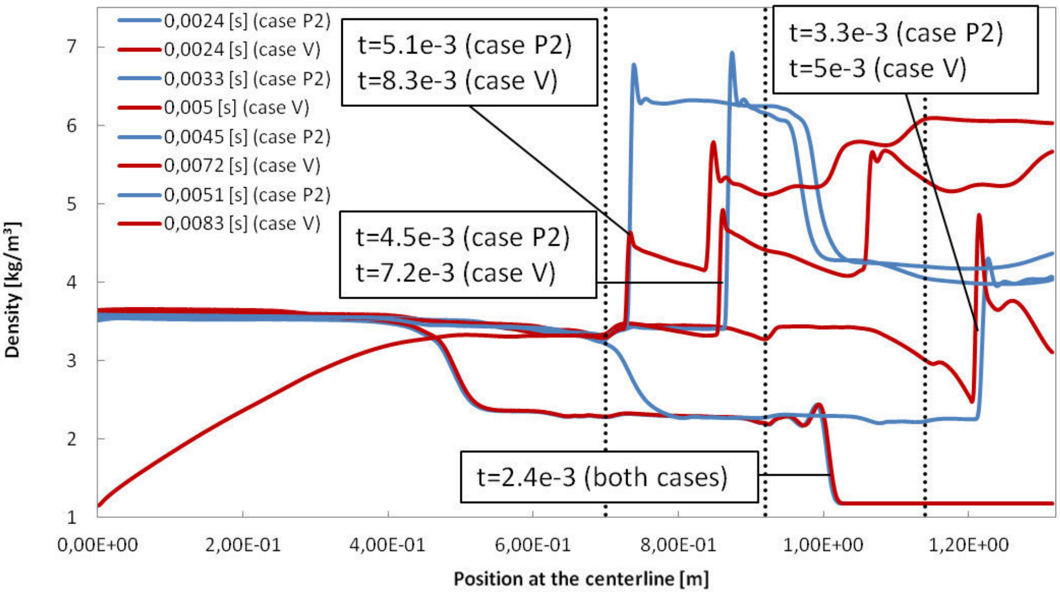

Figure 64: Variations of the density [kg/m³] along the centerline of the duct at different times

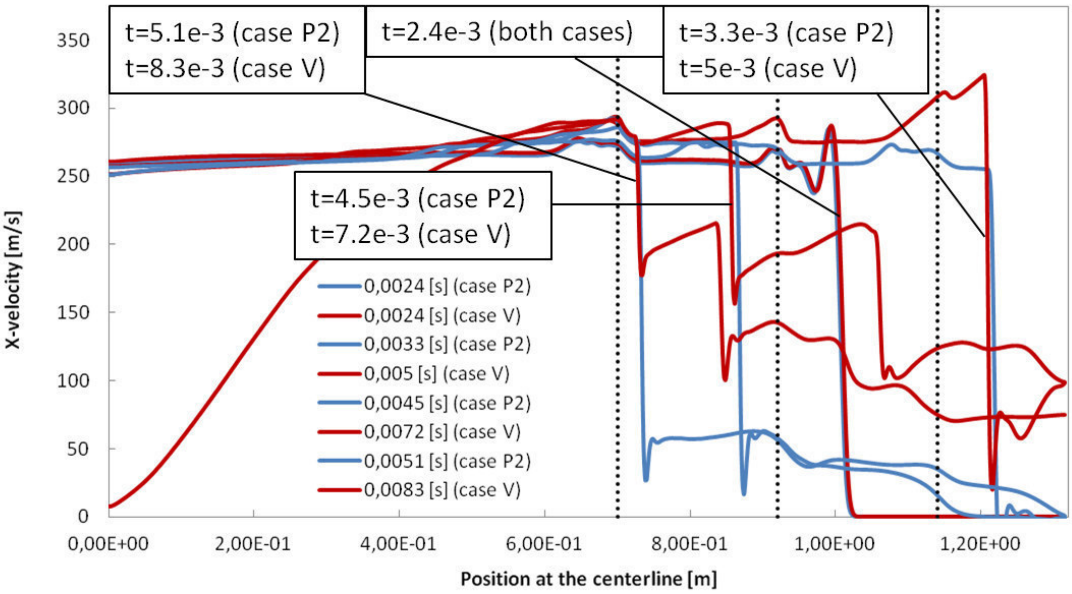

Figure 65: Variations of the streamwise velocity [m/s] along the centerline of the duct at different times

Figure 65 shows the centerline variations of the streamwise flow velocities at the same times, as used above for the variations of the static pressure and density. It can be clearly seen that the velocities are significantly different after the reflection. While the velocity of the unmodified case P2 drops close to zero after reflection, the velocity of the adapted case V remains on a markedly higher level. This indicates that a considerable amount of mass keeps flowing into the extra volume at the shown times.

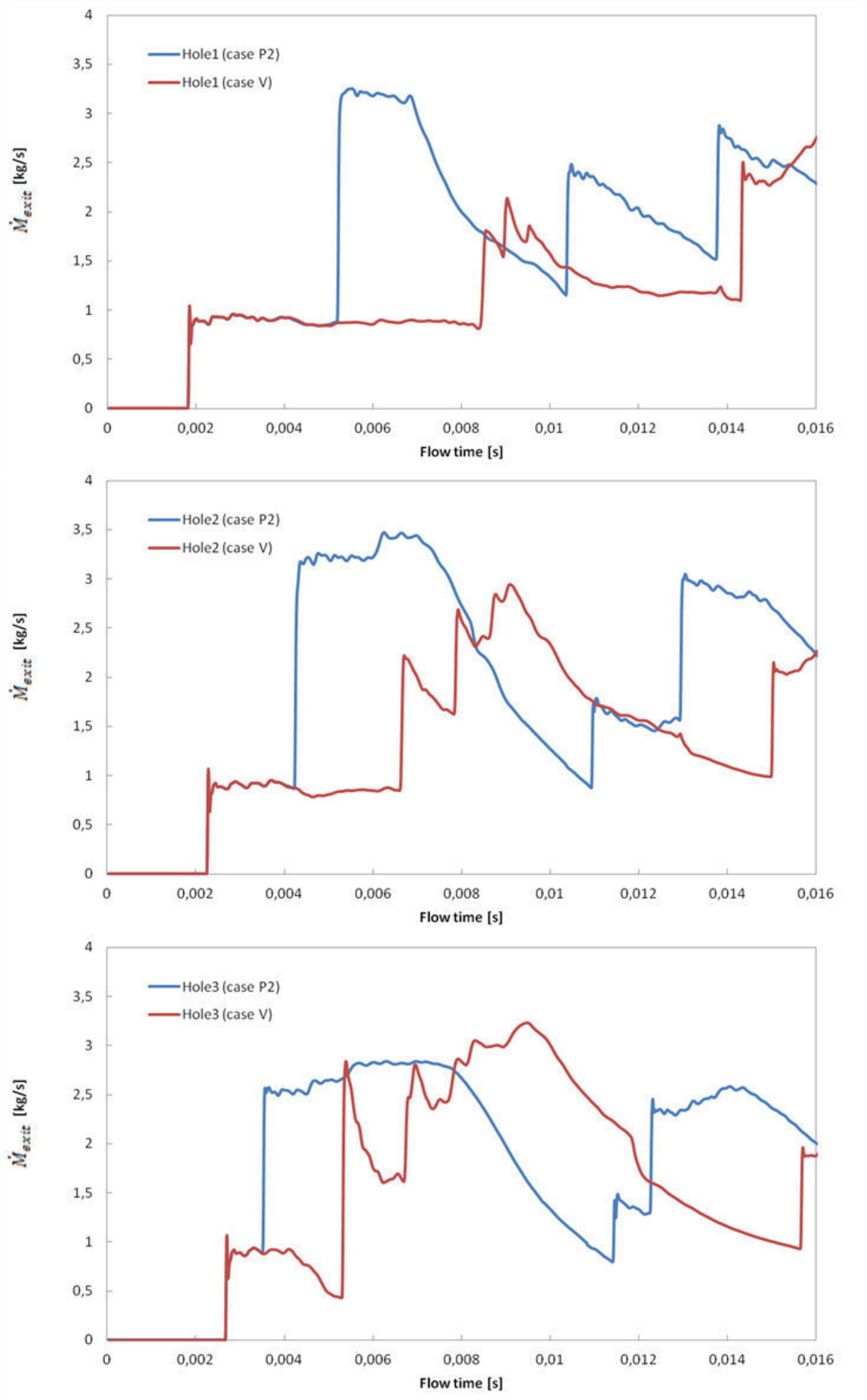

Figure 66: Comparison of the mass flow histories [kg/s] at the different exit holes

In Figure 66 the mass flow rates of the modified two-dimensional case V are compared against the data obtained for the case P2 associated with the unmodified end of the duct. This representation clearly shows the influence of the extra volume at the end of the duct on the mass flow exiting at the individual holes. The mass flow rates of the modified case are mostly below the mass flow rates for the case without modification. This is particularly evident when looking at the first exit hole (top illustration). In the unmodified case (case P2) three sudden rises, between t=0.004 [s] and t=0.014 [s], can be observed most pronouncedly at exit hole 1. These distinct increases are caused by the shock wave, which is propagated through the duct being reflected first at the end, and then at the inlet, where the valve has already been closed. This can be clearly demonstrated by the histories of the static pressure, obtained at the centerline of the duct directly above the individual exit holes shown in Figure 67. The first stepwise increase in the static pressure occurs at the same time for both cases, and is caused by the passage of the primary shock formed during the fast increase of the inlet mass flux up to the critical limit simulating the rapid opening of the valve. The second stepwise increase is due to the passage of the shock wave returning from the reflection at the end of the duct. The third and fourth sharp increases in pressure are caused the shock front reflected from the (closed) inlet and the one being reflected again at the end, respectively.

Comparing the results for the unmodified case against those for the duct with the modified end, most significant differences appear in the increase of the pressure which is caused by the first reflection from the end. The attached expansion volume leads evidently to a diffracted shock reflection, such that not a single strong but rather multiple weaker shocks are reflected back into the channel. These attenuated diffracted shocks pass the exit holes at a later time as compared to the unmodified case. Due to this time delay the fourth sharp increase in pressure observed for the unmodified case does not appear for the modified case in the shown time interval.

The observed multiple increase in pressure caused by the passage of the diffracted shock reflections, translates into a corresponding multiple increase in the exiting mass flow rate at the individual exit holes. At the exit holes one and two the mass flow rates do thereby in general finally not reach the same levels as observed for the unmodified case. This can be attributed to the delayed collision between the contact surface and the reflected weaker diffracted shock waves, which results in a more gradual less pronounced increase in the local density directly above these exit holes. At later time, i.e., t > 0.014s, the mass flow rate increases sharply once again, which is due to the passage of the shock wave reflected from the closed inlet. This behaviour is featured by both cases.

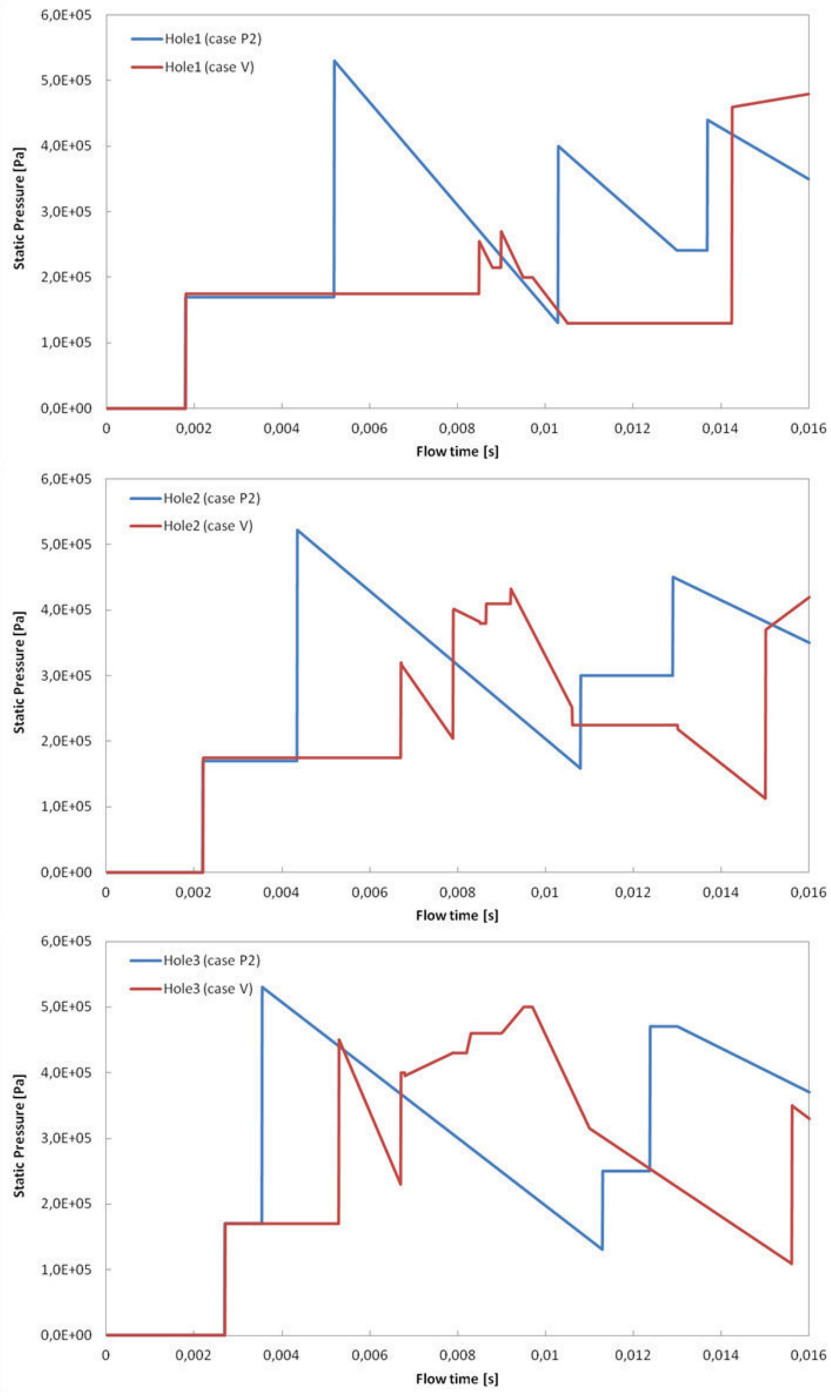

Figure 67: Comparison of the static pressure histories [Pa] at the different exit holes

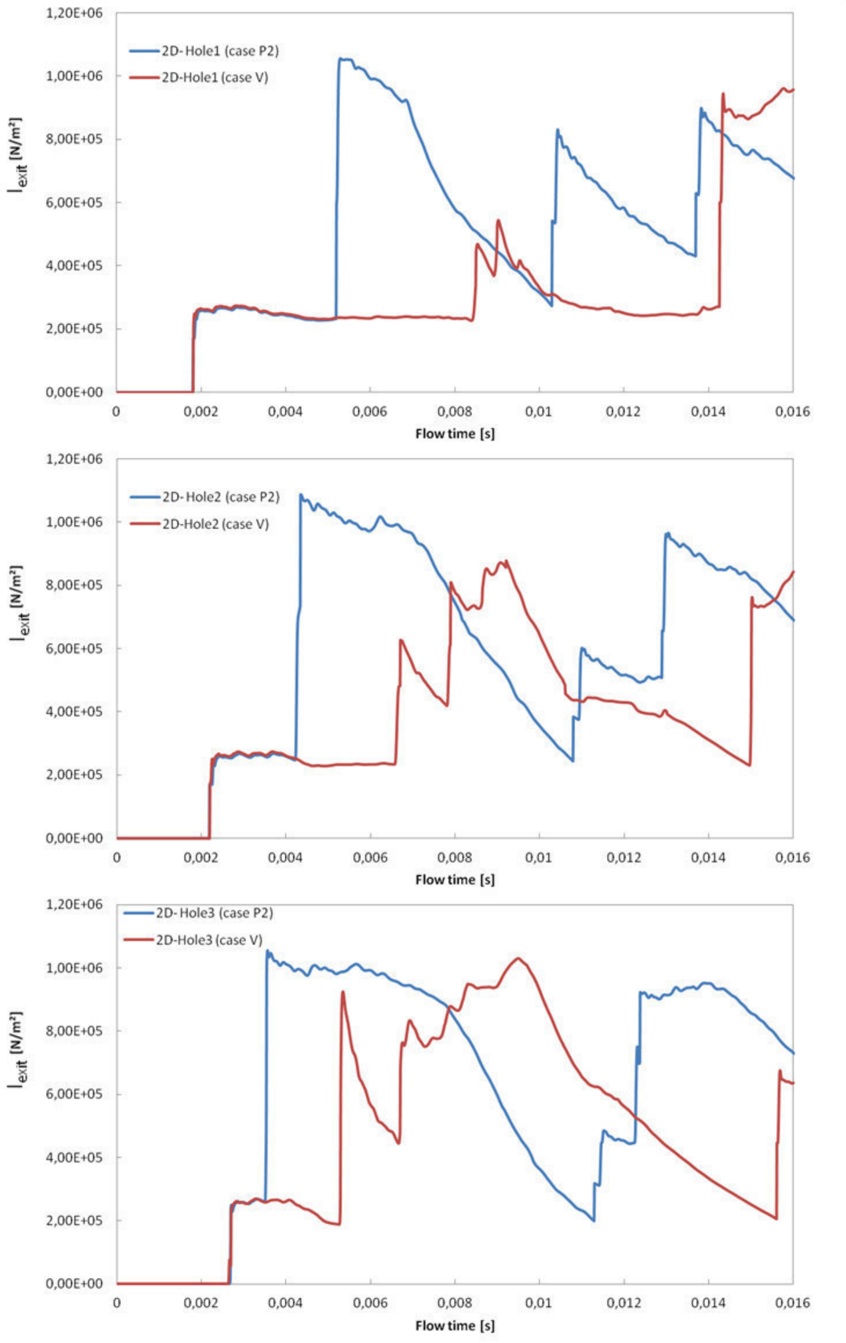

Figure 68: Comparison of the impulse [N/m²] escaping the single holes

A strong effect of the extra volume on the blow out characteristics can be observed when looking at the histories of the momentum of the exiting pulse jets depicted in Figure 68. The shown evolutions were calculated again according to Eq. (4.2), as already used for calculating the exit momentum in the previous section. It can be seen that the exit momentum follows closely the evolutions of the exit mass flow rates shown in Figure 66 for both cases. Accordingly, the attached expansion volume temporally delays the second strong increase in exit momentum associated with the first shock reflection. Furthermore, due to the reflection in terms of a sequence of diffracted multiple shocks this increase occurs in a stepwise manner. At the exit holes one and two the second increase in exit momentum does not only occur at later times but is also markedly less pronounced as compared to the unmodified case P2. On the other hand, the third rapid increase in exit momentum at t > 0.014, which is caused by the passage of the shock being reflected from the closed inlet, is still considerably strong. In summary, it can be stated that the attached expansion volume attenuates the very strong and rapid increase in exit momentum typically occurring upon passage of the shock wave, which has been reflected for the first time from the end of the channel. The obtained less intense increase in exit momentum of the pulse jets expectedly reduces the particularly high mechanical load generally imposed on the filter bags near the end, extending their material life time. On the other hand, the lower levels in the exit moment at the exit holes further away from the end of the channel (here represented by exit hole 1) certainly translates into less mechanical impulse for dedusting the filter bags at these positions. Here the question arises whether these filter bags are still cleaned sufficiently.

5. Conclusions

The present work computationally investigated the compressible flow inside a distributor channel as it is typically used in industrial devices for the dedusting of bag filters. The numerical simulations of this transonic flow was carried using the CFD-Software ANSYS-Fluent 14. Since a numerical modelling of a real-life distributing channel in full scale would be computationally too expensive, simplified computational models had to be derived. The simplifications were essentially made on the geometrical shape and total length of the channel, the total number of exit holes, and on the spatial dimensionality of the problem. In simulations of various test cases it was shown that the propagation of the shock waves and their reflections returning from the closed channel end were sufficiently well captured by a two-dimensional planar model when comparing its results to those obtained with a computationally much costlier three-dimensional model. The effect of a 90° bend, which is met in the real device in the section between the pressure vessel and the straight distributor duct, was also shown to be insignificant on the conditions further downstream. This bend could therefore be omitted in the numerical model. The derived two-dimensional model, which appeared to be as well suited for describing the most important features of the considered flow problem, assumes a straight planar distributor duct with in total three exit holes at the bottom.

The analysis of the results obtained with this model made evident that the holes have a rather small influence on the propagation of the shock wave inside the channel. This was indicated by the variations of the pressure and the density along the centreline of the channel, which turned out to be fairly unaffected by the flow through the exit holes. The results also demonstrated very well the high impact of the returning shock wave being reflected from the channel end on the blow out characteristics. Upon passage of the reflected shock the exit moment is rapidly increased once more significantly above the level which was reached upon passage of the primary shock generated at the inlet due to the fast ramping up of the mass inflow to the critical value. The almost instantaneously reached high level of exit momentum is even further increased in the region, where the reflected shock collides with the density discontinuity, which is propagated into the channel following the primary shock wave. The highly intense mechanical load suddenly imposed on the bag filters resulting from this observed strong second increase in exit momentum may be to some extent attenuated by modifying the end of the duct. Adding an expansion volume at the end of the duct can diffract the shock reflection producing several weaker reflected waves, as it was shown in a corresponding representative test case. At the most critical exit, near the end of the duct, the passage of the diffracted shock reflections turns the otherwise almost jump-like change in exit momentum into a more gradually, step-by-step, increase. The resulting more moderate increase of the mechanical impulse injected into the filter bags may be beneficial for their material life-time.

As for the relevance of the presently obtained results for the real industrial full-scale device the strongly reduced total axial length of the numerically modelled distributor ducts has to be taken into account. The significantly shorter duct inherently implies shorter propagation times for the density discontinuity and the shock fronts between the reflections at the end and the closed inlet. The conditions in the proximity of the duct end are still very well representative for the real application, with and without the attached expansion volume.

In summary, one can say that the presently used simplified numerical model describes the propagation of the shock wave inside the considered distributor channel and the resulting blow out at the single exit very well. The investigated problem basically does not necessarily require a very costly three-dimensional simulation to obtain a qualitative and, to a certain extent, also quantitative fairly good insight into the behaviour of the compressible flow. For a more detailed description of the local flow conditions, a three-dimensional treatment is still indispensable. Also the case with a modified end of the channel should be treated as a three-dimensional problem for further more detailed investigations. Particularly, the on first sight positive effect of the attached volume has to be further examined. The observed significant impact on the flow and the blow out does not automatically imply less mechanical wear for the bag filter material near the channel end together with an efficient dedusting of the filters. Showing this goes however beyond the scope of the presently performed simulations.

6. References

[1] Schneider, J. (1999). *Exposure of the austrian population to PM10 in 1996.* Wien: Umweltbundesamt GmbH.

[2] Schneider, J. (2006). *Schwebestaub in Österreich.* Wien: Umweltbundesamt GmbH.

[3] Bank, M. (1995). *Basiswissen Umwelttechnik- Wasser, Luft, Abfall, Lärm 3. Auflage.* Vogel Buchverlag.

[4] Flagan, R. C., & Seinfeld, J. H. (1988). *Fundamentals of air pollution engineering.* New Jersey: Prentice-Hall.

[5] Radl, A. D.-I. (2013/2014). *Lecture notes to Particle Technology II.* Technical University Graz

[6] Sutherland, K. (2008). *Filters and Filtration Handbook.* Oxford: Elsevier.

[7] Holgate, S. T. (2001). *Air pollution and health.* San Diego: Academic press.

[8] Infastaub. . Abgerufen am 31. 03 2015 von http://www.infastaub.de/en/infos/entstaubung-lexikon/staubabscheidung/technical-processes-for-dust-removal/

[9] Rhodes, M. (2008). *Introduction to Particle Technology.* Chichester: Hohn Wiley & Sons.

[10] Hoffmann, A. C., & Stein, L. E. (2008). *Gas Cyclones and Swirl Tubes: Principles, Design and Operation.* New York: Springer.

[11] Cheremisinoff, P. N., (2002). *Handbook of air pollution prevention and control*. Massachusetts: Butterworth Heinemann

[12] Schubert, H. (2003). *Handbuch der mechanischen Verfahrenstechnik.* Weinheim: Wiley.

[13] Löffler, F., Dietrich, H., & Flatt, W. (1988). *Dust collection with bag filters and envelope filters.* Wiesbaden: Vieweg.

[14] Systems, A. E. Abgerufen am 27. 04 2015 von http://ablenviro.tradeindia.com/

[15] *Wikipedia*. Abgerufen am 22. 04 2015 von http://en.wikipedia.org/wiki/Baghouse

[16] Cheremisinoff, P. N., & Young, R. A. (1977). *Air pollution control and design handbook- Part 2.* New York: Marcel Dekker.

[17] WPCA. (2011). *WPCA-Duke Energy FF/HAPS Seminar.*

[18] Infastaub. (09 2014). *Infastaub.de.* Abgerufen am 20. 04 2015 von http://www.infastaub.de/infos/entstaubung-lexikon/

[19] Schrooten, T., Kögel, A., & Klein, G.-M. (kein Datum). *Chemeurope.com*. Abgerufen am 2015. 04 13 von http://www.chemeurope.com/en/whitepapers/126300/industrial-dedusting-with-bag-filters.html

[20] Pentair. (2015). *Pentair*. Abgerufen am 11. 05 2015 von http://cleanairsystems.com/products-2/filter-cleaning-system-accessories/blowtube-nozzles-cartridge-cleaning-cones.html

[21] Ansys. (2009). *Ansys Fluent Theory Guide.* Ansys.

[22] Brenn, U.-P.-I. G. (2012). *Vorlesungsskript- Strömungslehre und Wärmeübertragung I.* Graz: Technical university of graz.

[23] Gurker, T. (2010). *Experimentelle Charakterisierung einer gerührten Extraktionskolonne und Vergleich mittels Computational Fluid Dynamics.* Graz: Technical University of Graz.

[24] Schwarze, R. (2013). *CFD-Modellierung: grundlagen und Anwendungen bei Strömungsprozessen.* Berlin: Springer Vieweg.

[25] Metzner, M. (2003). *Mehrgitterverfahren für die kompressiblen Euler- und Navier-Stokes-Gleichungen mit besonderer Betrachtung des schwachen kompressiblen Falles.* Heidelberg.

[26] Brenn G., Meile W. (2011) Vorlesungsunterlagen zu Strömungslehre und Wärmeübertragung I. Technische Universität Graz

[27] Hakenesch, P. D.-I. *Munich University of Applied Sciences - Fakultät 03.* Abgerufen am 22. 04 2015 von http://hakenesch.userweb.mwn.de/aerodynamik/K8_Folien.pdf

[28] Brenn, U.-P.-I. G. (2014). *Vorlesungsskript- Gasdynamik.* Graz: Technical university of graz.

[29] Eckart Laurien, H. O. (2011). *Numerische Strömungsmechanik (Grundgleichungen und Modelle-Lösungsmethoden- Qualität und Genauigkeit).* Wiesbaden: Vieweg+ Teubner.

[30] Oertel jr., H., Böhle, M., & Reviol, T. (2011). *Strömungsmechanik.* Wiesbaden: Vieweg+teubner.

[31] Dipl.-Ing. Thomas Eipper, C. S. (2011). *Lavaldüse- Praktikumsanleitung.* Dresden: Technische Universität Dresden.

[32] Gretler, o. U.-P. (1982). *Gasdynamik.* Technische Universität Graz: Institut für Strömungslehre

[33] Böckh, P. v., & Saumweber, C. (2013). *Fluidmechanik: Einführendes Lehrbuch.* Berlin: Springer Vieweg.

[34] Gertl, R. (2010). *CFD-Simulation des SNCR-Verfahrens.* Graz: Technical University of Graz..

[35] Andersson, B. et.al (2008). *Computational fluid dynamics for chemical engineers.* Gothenburg.

[36] Helfried, A.-P. D.-I. (2014). *Numerical methods in fluid mechanics and heat transfer.* Graz: Technical University of Graz.

[37] Fluent.Inc. (28. November 2001). *afs.enea.it.* Abgerufen am 23. September 2015 von http://www.afs.enea.it/fluent/Public/Fluent-Doc/PDF/chp22.pdf

[38] Fluent.Inc. (20. 09 2006). *Aerojet.* Abgerufen am 14. September 2015 von http://aerojet.engr.ucdavis.edu/fluenthelp/html/ug/node988.htm

[39] P.Spalart, S Allmaras. A one-equation turbulence model for aerodynamic flows. Technical report AIAA-92-0439, American Institute of Aeronautics and Astronautics, 1992

[40] Launder, B.E., and Sharma, B.I. (1974), Application of the energy dissipation model of turbulence to the valculation of flow near a spinning disc, Letters in heat an mass transfer

[41] Wilcox, David C. (1998), Turbulence modelling for CFD. Second edition. Anaheim DCW industries, 1998

[42] Bakker, A. (2002). Abgerufen am 20.01.2016 von http://www.bakker.org/dartmouth06/engs150/06-bound.pdf

[43] Boris, J.P., Book, D.L. (1973). Flux-corrected transport I: SHASTA, a fluid transport algorithm that works. Washington D.C.